THESIS FOR THE DEGREE OF DOCTOR OF PHILOSOPHY IN THE NATURAL SCIENCES

Advances in Membrane Protein Structural Biology:

Lipidic Sponge Phase Crystallization, Time-Resolved Laue Diffraction and Serial Femtosecond Crystallography

LINDA JOHANSSON

GÖTEBORGS UNIVERSITET

University of Gothenburg
Department of Chemistry and Molecular Biology
Göteborg, Sweden, 2013

Advances in Membrane Protein Structural Biology:
Lipidic Sponge Phase Crystallization, Time-Resolved Laue Diffraction and Serial Femtosecond Crystallography

Linda Johansson

Cover: Crystal structure of the membrane protein reaction center from the bacterium *Blastochloris viridis* on a background of a diffraction pattern collected at the Linac Coherent Light Source.

ISBN 978-91-628-8694-3
Available online at http://hdl.handle.net/2077/32704

University of Gothenburg
Department of Chemistry and Molecular Biology
Lundbergslaboratoriet
SE-405 30 Gothenburg
Sweden
Telephone: +46(0)31-786 0000

Printed by Ineko AB
Göteborg, Sweden, 2013

Till Mattias

Abstract

Membrane proteins carry out many essential tasks in cells such as signaling and transport, or function as electron carriers in photosynthesis and cellular respiration. The aim of this thesis has been to develop new and improve existing techniques for elucidating the structure and function of membrane proteins.

Membrane proteins are difficult to crystallize due to their combination of hydrophilic and hydrophobic domains. Part of this thesis was therefore dedicated to the development of a membrane protein crystallization screen based on mimicking the protein's native environment. The screen, consisting of 48 different lipidic sponge phase (LSP) conditions, was tested on eleven different membrane proteins and gave crystal leads for eight of these. One of these leads was the photosynthetic reaction center of the purple bacterium *Blastochloris viridis* (RC_{vir}). Two high-resolution structures to 1.86 Å and 1.95 Å were obtained from data collected using different radiation doses and revealed a new space group and novel crystal packing along with a number of lipid-protein interactions.

Using this new crystal form the electron-transfer reaction of RC_{vir} was studied by time-resolved Laue diffraction where data were collected on crystals illuminated with light at room temperature. This revealed a reproducible movement of the highly conserved TyrL162 residue towards the special pair upon photoactivation. These results were combined with molecular dynamics studies to propose a coupling between the conformational orientation and protonation states within a bacterial reaction center.

Finally, the LSP method was extended to a batch type of crystallization approach. This provided a large volume of micron-sized crystals suitable for structure determination at the Linac Coherent Light Source, a recently commissioned X-ray free electron laser (XFEL) facility. Data from hundreds of microcrystals were collected to low resolution and revealed yet another space group and crystal packing. After the commissioning of a high-resolution beamline, the structure of RC_{vir} was solved to 3.5 Å resolution. This represents the highest resolution membrane protein structure determined using XFEL radiation to date.

Contribution report

Paper I I took a major part in summarizing the literature, preparing figures and was involved in writing of the manuscript.

Paper II I prepared all the lipidic sponge phases, ran the SAXS- measurements and performed all the crystallization trials. I contributed to writing the manuscript as well as preparing the figures.

Paper III I was involved in data collection and processing. I contributed to the writing of the manuscript and preparation of figures.

Paper IV I grew crystals, collected Laue diffraction data, processed one of the datasets and contributed to solving the structures. I prepared the majority of the figures and participated in writing the manuscript.

Paper V I planned the project, cultivated the cells, prepared the protein, and developed the crystallization method. I collected the data and solved the structure. I took a major part in writing of the manuscript including preparation of all the figures.

Paper VI I was responsible for entire the project, including preparation of protein, crystallization, and optimization of crystals. I collected the data, processed the diffraction images and solved the structure. I contributed to writing the manuscript and prepared all figures.

List of Publications

Paper I **Linda C Johansson**, Annemarie B Wöhri, Gergely Katona, Sven Engström and Richard Neutze. Membrane protein crystallization from lipidic phases (2009*). Curr. Opin. Struct. Biol*. **19:** 372-378 (Review).

Paper II Annemarie B. Wöhri, **Linda C. Johansson**, Pia Wadsten-Hindrichsen, Weixiao Y. Wahlgren, Gerhard Fischer, Rob Horsefield, Gergely Katona, Maria Nyblom, Fredrik Öberg, Gillian Young, Richard J. Cogdell, Niall J. Fraser, Sven Engström, and Richard Neutze. (2008). A lipidic-sponge phase screen for membrane protein crystallization, *Structure* **16**, 1003-1009.

Paper III Annemarie B. Wöhri, Weixiao Y. Wahlgren, Erik Malmerberg**, Linda C. Johansson**, Richard Neutze and Gergely Katona (2009). Lipidic Sponge Phase Crystal Structure of Photosynthetic Reaction Center Reveals Lipids on the Protein Surface (2009). *Biochemistry* **48:** 9831-9838.

Paper IV Annemarie B. Wöhri, Gergely Katona**, Linda C. Johansson**, Emelie Fritz, Erik Malmerberg, Magnus Andersson, Jonathan Vincent, Mattias Eklund, Marco Cammarata, Michael Wulff, Jan Davidsson, Gerrit Groenhof, Richard Neutze (2010). Light induced Structural Changes in a Photosynthetic Reaction Center Caught by Laue Diffraction. *Science* **328**: 630-633.

Paper V **Linda C. Johansson**, David Arnlund, Thomas A. White, Gergely Katona, Daniel P. DePonte, Uwe Weierstall, R. Bruce Doak, Robert L. Shoeman, Lukas Lomb, Erik Malmerberg, Jan Davidsson, Karol Nass, Mengning Liang, Jakob Andreasson,Andrew Aquila, Saša Bajt, Miriam Barthelmess, Anton Barty, Michael J. Bogan, Christoph Bostedt, John D. Bozek, Carl Caleman, Ryan Coffee, Nicola Coppola, Tomas Ekeberg, Sascha W. Epp, Benjamin Erk, Holger Fleckenstein, Lutz Foucar, Heinz Graafsma, Lars Humprecht, Janos Hajdu, Christina Y. Hampton, Robert Hartmann, Andreas Hartmann, Günter Hauser, Helmut Hirsemann, Peter Holl, James M. Holton, Mark S. Hunter, Stephan Kassemeyer, Nils Kimmel, Richard A. Kirian, Filipe R.N.C. Maia, Stefano Marchesini, Andrew V. Martin, Christian Reich, Daniel Rolles, Benedikt Rudek, Artem Rudenko, Ilme Schlichting, Joachim Schulz, M. Marvin Seibert, Raymond Sierra, Heike Soltau, Dimitri Starodub, Francesco Stellato, Stephan Stern, Lothar Strüder, Nicusor Timneanu, Joachim Ullrich, Weixiao Y. Wahlgren, Xiaoyu Wang, Georg Weidenspointner, Cornelia Wunderer, Petra Fromme, Henry N. Chapman, John C. H. Spence, Richard Neutze (2012). Lipidic phase membrane protein serial femtosecond crystallography. *Nature Methods* **9**: 263–265.

Paper VI **Linda C. Johansson**, David Arnlund, Gergely Katona, Thomas A. White, Daniel P. DePonte, Anton Barty, Cecilia Wickstrand, Robert L. Shoeman, Sébastien Boutet, Garth J. Williams, Andrew Aquila, Thomas R.M. Barends, Michael J. Bogan, Carl Caleman, R. Bruce Doak, Matthias Frank, Raimund Fromme, Lorenzo Galli, Ingo Grotjohann, Mark S. Hunter, Richard A. Kirian, Chris Kupitz, Mengning Liang, Lukas Lomb, Erik Malmerberg, Andrew V. Martin, Marc Messerschmidt, Karol Nass, Lars Redecke, M. Marvin Seiber, Jennie Sjöhamn, Jan Steinbrener, Francesco Stellato, Dingjie Wang, Weixaio Y. Wahlgren, Uwe Weierstall, Sebastian Westenhoff, Nadia A. Zatsepin, John C.H. Spence, Ilme Schlichting, Henry N. Chapman, Petra Fromme, Richard Neutze. (2013). Membrane Protein Microcrystal Serial Femtosecond Crystallography. *Manuscript.*

Related publications

Paper VII Andrew Aquila, Mark S. Hunter, R. Bruce Doak, Richard A. Kirian, Petra Fromme, Thomas A. White, Jakob Andreasson, David Arnlund, Saša Bajt, Thomas R. M. Barends, Miriam Barthelmess, Michael J. Bogan, Christoph Bostedt, Hervé Bottin, John D. Bozek, Carl Caleman, Nicola Coppola, Jan Davidsson, Daniel P. DePonte, Veit Elser, Sascha W. Epp, Benjamin Erk, Holger Fleckenstein, Lutz Foucar, Matthias Frank, Raimund Fromme, Heinz Graafsma, Ingo Grotjohann, Lars Gumprecht, Janos Hajdu, Christina Y. Hampton, Andreas Hartmann, Robert Hartmann, Stefan Hau-Riege, Günter Hauser, Helmut Hirsemann, Peter Holl, James M. Holton, André Hömke, **Linda Johansson**, Nils Kimmel,Stephan Kassemeyer, Faton Krasniqi, Kai-Uwe Kühnel, Mengning Liang, Lukas Lomb, Erik Malmerberg, Stefano Marchesini, Andrew V. Martin, Filipe R.N.C. Maia, Marc Messerschmidt,Karol Nass, Christian Reich, Richard Neutze, Daniel Rolles, Benedikt Rudek, Artem Rudenko, Ilme Schlichting, Carlo Schmidt, Kevin E. Schmidt, Joachim Schulz,1 M. Marvin Seibert, Robert L. Shoeman, Raymond Sierra, Heike Soltau, Dmitri Starodub, Francesco Stellato, Stephan Stern, Lothar Strüder, Nicusor Timneanu, Joachim Ullrich, Xiaoyu Wang, Garth J. Williams, Georg Weidenspointner, Uwe Weierstall, Cornelia Wunderer, Anton Barty, John C. H. Spence, and Henry N. Chapman (2011). Time-resolved protein nanocrystallography using an X-ray free-electron laser. *Optics express* **20:3**: 2706-2716.

Paper VIII Sébastien Boutet, Lukas Lomb, Garth J. Williams, Thomas R.M. Barends, Andrew Aquila, R. Bruce Doak, Uwe Weierstall, Daniel P. DePonte, Jan Steinbrener, Robert L. Shoeman, Marc Messerschmidt, Anton Barty, Thomas A. White, Stephan Kassemeyer, Richard A. Kirian, M. Marvin Seibert, Paul A. Montanez, Chris Kenney, Ryan Herbst, Philip Hart, Jack Pines, Gunther Haller, Sol M. Gruner, Hugh T. Philip,, Mark W. Tate, Marianne Hromalik, Lucas J. Koerner, Niels van Bakel, John Morse, Wilfred Ghonsalves, David Arnlund, Michael J. Bogan, Carl Caleman, Raimund Fromme, Christina Y. Hampton, Mark S. Hunter, **Linda Johansson**, Gergely Katona, Christopher Kupitz, Mengning Liang, Andrew V. Martin, Karol Nass, Lars Redecke, Francesco Stellato, Nicusor Timneanu, Dingjie Wang, Nadia A. Zatsepin, Donald Schafer, James Defever, Richard Neutze, Petra Fromme, John C.H. Spence, Henry N. Chapman and Ilme Schlichting (2011). High-resolution protein structure determination by Serial Femtosecond Crystallography. *Science* **337:** 362-364.

Paper IX Anton Barty, Carl Caleman, Andrew Aquila, Nicusor Timneanu, Lukas Lomb, Thomas A. White, Jakob Andreasson, David Arnlund, Sasa Bajt, Thomas R.M. Barends, Miriam Barthelmess, Michael J. Bogan, Christoph Bostedt, John D. Bozek, Ryan Coffee, Nicola Coppola, Jan Davidsson, Daniel P. DePonte, R. Bruce Doak,Tomas Ekeberg, Veit Elser, Sascha W. Epp, Benjamin Erk, Holger Fleckenstein, Lutz Foucar, Petra Fromme, Heinz Graafsma, Lars Gumprecht, Janos Hajdu, Christina Y. Hampton, Robert Hartmann, Andreas Hartmann, Günter Hauser, Helmut Hirsemann, Peter Holl, Mark S. Hunter, **Linda Johansson**, Stephan Kassemeyer, Nils Kimmel, Richard A. Kirian, Mengning Liang, Filipe R.N.C. Maia, Erik Malmerberg, Stefano Marchesini, Andrew V. Martin, Karol Nass, Richard Neutze, Christian Reich, Daniel Rolles, Benedikt Rudek, Artem Rudenko, Howard Scott, Ilme Schlichting, Joachim Schulz, M. Marvin Seibert, Robert L. Shoeman, Raymond Sierra, Heike Soltau, John C. H. Spence, Francesco Stellato, Stephan Stern, Lothar Strüder, Joachim Ullrich, X. Wang, Georg Weidenspointner, Uwe Weierstall, Cornelia B. Wunderer and Henry N.Chapman (2011). Self-terminating diffraction gates femtosecond X-ray nanocrystallography measurements. *Nature Photonics* **6:** 35-40

Paper X Erik Malmerberg, Ziad Omran, Jochen S. Hub, Xueven Li, Gergely Katona, Sebastian Westenhoff, **Linda C. Johansson,** Magnus Andersson, Marco Cammarata, Michael Wulff, David van der Spoel, Jan Davidsson, Alexandre Specht and Richard Neutze (2011). Time-resolved WAXS reveals accelerated conformational changes in iodoretinal-subsituted proteorhodopsin. *Biophysical Journal* **101**: 1245-53

Paper XI Sebastian Westenhoff, Erik Malmerberg, David Arnlund**, Linda Johansson**, Elena Nazarenko, Marco Cammarata, Jan Davidsson, Vincent Chaptal, Jeff Abramson, Gergely Katona, Andreas Menzel and Richard Neutze (2010). Rapid readout detector captures protein time-resolved WAXS. *Nature Methods* **7**: 775-776.

Paper XII Magnus Andersson, Erik Malmerberg, Sebastian Westenhoff, Gergely Katona, Marco Cammarata, Annemarie B. Wöhri, **Linda C. Johansson**, Friederike Ewald, Mattias Eklund, Michael Wulff, Jan Davidsson and Richard Neutze (2009). Structural Dynamics of Light-Driven Proton Pumps, *Structure* **17:** 1265-75

Table of contents

Abbreviations

BChl	Bacteriochlorophyll *a*
BPhe	Bacteriopheophytin *a*
bR	Bacteriorhodopsin from *Halobacterium salinarum*
BsSQR	Complex II from *Bacillus subtilis*
β-OG	n-octyl-β -D-glucopyranoside
CHAPS	3-([3-cholidamidopropyl]dimetylammonio)-1-propane sulfonate
DDM	n-dodecyl-β-D-maltopyranoside
DMSO	Dimethyl sulfoxide
Ia3d	Gyroid lipidic cubic phase
Im3m	Primitive lipidic cubic phase
L_c	Liquid crystal
LCP	Lipidic cubic phase
LSP	Lipidic sponge phase
LDAO	Lauryldimethylamine-N-oxide
$LH2_{aci}$	Light-harvesting complex 2 from *Rhodopseudomonas acidophila*
L_3	Lipidic sponge phase
Lα	Lamellar phase
MAG	Monoacylglycerol
MO	Monoolein
MPD	2-methyl-2,4-pentanediol
MQA	Menaquinone
MW	Molecular weight
PDB	Protein data bank
PEG	Polyethylene glycol
PfAQP	Aquaporin from *Plasmodium falsiparum*
Pn3m	Diamond lipidic cubic phase
pR	Proteorhodopsin from γ-proteobacterium
PSI, PSII	Photosystem I, II
P_{960}	Special pair from *Blastochloris viridis*
Q, Q_A, Q_B	Ubiquinone
QH_2	Ubiquinol
RC-LH1	Photosynthetic core complex from *Blastochloris viridis*
RC_{sph}	Reaction center from *Rhodobacter sphaeroides*
RC_{vir}	Reaction center *Blastochloris viridis*
SAXS	Small-angle X-ray scattering
SoPIP2;1	Aquaporin from *Spinacia oleracea*
SFX	Serial femtosecond crystallography
Thesit	Polyoxylene(9)dodecyl ether
TM	Transmembrane
UbOx	Ubiquinol oxidase from *Escherichia coli*
XFEL	X-ray Free-Electron Laser
Å	Ångström (=10^{-10} m= 0.1 nm)

1 Introduction

Cells are able to communicate with their surroundings through proteins. In particular, many cellular functions are carried out by membrane proteins which perform various tasks such as signaling, transport of compounds or carry out cellular respiration or photosynthesis. The structure of proteins can be studied using X-ray radiation, which requires the proteins to form crystals. However, membrane proteins are notoriously difficult to crystallize due to their amphiphilic nature and major efforts have been dedicated towards providing a stabilizing environment which can promote crystallization events.

This work contributes to structural and functional understanding of a part of the photosynthetic apparatus, the reaction center, of the purple bacterium *Blastochloris viridis*. The structure was studied using both conventional synchrotron radiation, as well as the newly commissioned free-electron laser source and its electron transport was studied using time-resolved Laue diffraction. Furthermore, a lipid-based membrane protein crystallization screen was developed in an effort to facilitate crystallization of difficult membrane protein targets by stabilization in a membrane-like environment.

1.1 Biological membranes and membrane proteins

Cells need to distinguish between “outside” and “inside” to uphold their cellular functions. Most cells are further compartmentalized into different structures such as nucleus, chloroplasts and mitochondria, using a lipid bilayer (membrane) as a means of separation. Cells must also be able to communicate with their surroundings through exchange of various molecules, a task usually performed by membrane proteins such as transporters and channels [1].

Approximately 30 % of the proteome of a cell encodes membrane proteins [2]. This is a structurally and functionally diverse group which performs a variety of functions, all of which depend on their unique combination of amino acids and co-factors. Membrane proteins are usually subdivided into integral proteins, which are tightly bound to membranes and peripheral proteins which usually are loosely attached. Most membrane proteins perform essential functions and malfunction, alteration or loss of function can be detrimental to the cell. Therefore, many membrane proteins are potential drug targets, particularly G-protein coupled receptors, ion channels and transporters [3, 4].

1.2 Lipids used for membrane protein crystallization (Paper I)

Membrane proteins are embedded into a lipid bilayer in the cell and need to be extracted using detergents prior to purification. This procedure often leads to a loss of stability, which in turn decreases the crystallization success. An alternative method to the use of detergents is adding back lipids during crystallization in an attempt to mimic the protein’s native membrane. The most commonly used lipid for this purpose is Monoolein, which is capable of forming several phases suitable for crystallization such as the lipidic cubic and lipidic sponge phases. Another method

successfully used for membrane protein crystallization is the bicelle method, which relies on the formation of a lipid-detergent disc-like structure capable of incorporating a membrane protein. These three methods have aided in structural determination of a variety of membrane proteins, summarized in **Paper I** and in Table 1.

1.3 Structural studies of membrane proteins

The majority of protein structures are solved using X-rays and the first membrane protein to have its structure determined was reaction center from *Blastochloris viridis* in 1984 [5]. Since then efforts have been made to elucidate the structure of membrane proteins with increasing success. The amphiphilic nature of membrane proteins makes them difficult to crystallize and only a small fraction of known structures are of from membrane proteins [6]. New technical inventions in the field of X-ray sources such as synchrotrons and X-ray free electron lasers, development of cryo crystallography [7], as well as novel lipid-based crystallization techniques such as the lipidic cubic phase, the lipidic sponge phase and bicelle (summarized in **Paper I**) have also contributed to successfully determining novel membrane protein structures.

1.3.1 The use of third generation synchrotron radiation facilities for membrane protein crystallography

A third generation synchrotron source can produce brilliant beams in the 100 nm to 100 µm size range, making it suitable for a wide range of techniques applicable to (membrane) protein crystallography, particularly in the use of microfocus beamlines (and new data collection procedures [8]). One of the biggest contributions to the structural biology field is the possibility of a tunable wavelength. This allows *de novo* structure determination using SAD and MAD phasing methods [9]. Additionally, the pulsed behavior and intense beam can be exploited in the time-resolved Laue diffraction method.

1.3.1.1 Time-resolved Laue: room temperature data collection

Time-resolved Laue diffraction is used to study rapid changes occurring in biological systems such as proteins. The experiment is conducted at room temperature using a polychromatic beam, a static crystal and extremely short X-ray pulses. The most common method is the *pump-probe* where a reaction within the static crystal is induced by a short laser flash (pump) followed by an extremely short X-ray pulse (probe) to capture the movements occurring after photoactivation. A dark image is also taken to allow direct comparison with the illuminated state.

The use of a polychromatic beam allows for collection of a complete dataset using much fewer images. However, radiation and laser damage reduce the diffraction power of the crystal and it is not uncommon that data from several crystals need to be merged to obtain a complete dataset. An additional complication arises when membrane proteins are studied using the time-resolved Laue method, since these types of crystals tend to be more loosely packed and more prone to radiation damage. Furthermore, they are usually scarce, of lower diffraction quality and smaller in size. Despite these limitations, the membrane protein reaction center (RC_{vir}) has been successfully studied using Laue diffraction (**Paper IV** and [10]).

1.3.2 X-ray free electron lasers for protein structure determination

While a protein crystal cooled to cryogenic temperatures can tolerate an X-ray dose of 30 MGy [11], it was proposed in 1986 by Solem that this dose limit can be increased by using sufficiently short X-ray pulses [12] such as those from an X-ray free electron laser (XFEL). This was later modeled using molecular dynamics in 2000 by Neutze *et al.* [13], where they concluded that usable diffraction data could be collected before the sample exploded when using very short XFEL pulses: the "diffraction before destruction" principle.

An XFEL, such as the Linac Coherent Light Source (LCLS) [14] in Menlo Park, CA, US, can produce X-rays with energies up to 20 keV per pulse and a peak brilliance that is about a billion times stronger than that of a third generation synchrotron. It delivers extremely short pulses, a few to hundreds of femtoseconds (fs) in duration [15], allowing data collection from nanometer-sized protein crystals before the onset of radiation damage [16]. Furthermore, use of the ultrashort pulses allows for time-resolved experiments to be conducted, particularly on irreversible systems, made possible by the "one crystal, one shot" approach. It also provides a method where small crystals can be used, such as those obtained from membrane protein crystallization trials which often are unsuitable for conventional synchrotron data collection.

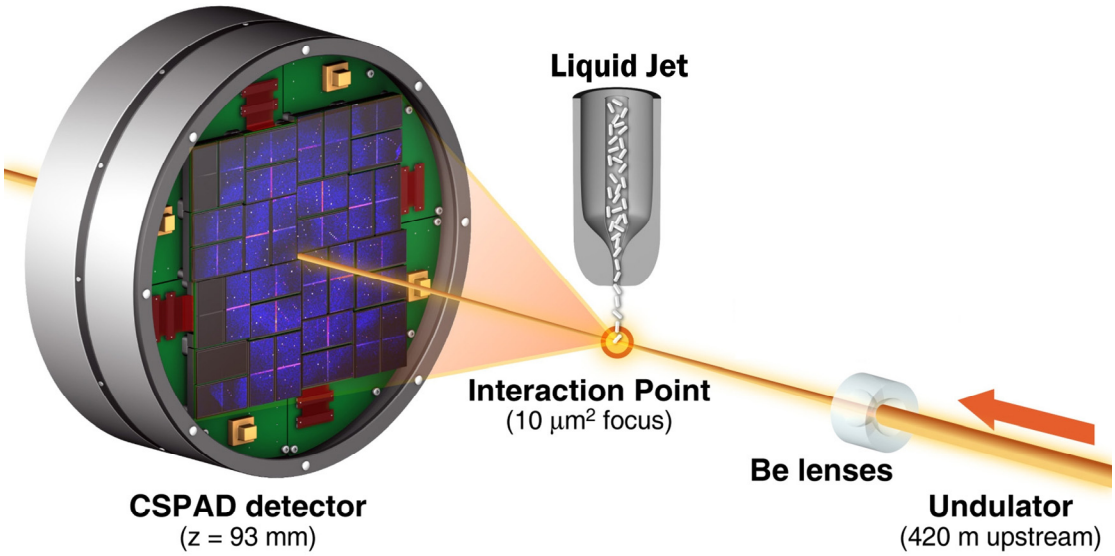

Figure 1. *Overview of the experimental setup at the Coherent X-ray Imaging (CXI) beamline at the Linac Coherent Light Source (LCLS) [17].The fully hydrated microcrystals are supplied using a liquid microjet [18] and diffraction data is collected on the CSPAD detector [19].*

The method of serial femtosecond crystallography (SFX) relies on collecting diffraction data from thousands of fully hydrated *microcrystals* injected into the XFEL beam using a liquid microjet (Figure 1 [17]). Since the commissioning of LCLS in 2009, several structures of soluble proteins have been solved including lysozyme [17] and cathepsin B [20] (in complex with its native inhibitor) and also from membrane proteins, albeit to lower resolution [18, 21, 22].

1.4 Photosynthesis

Sunlight is essential for life on earth and the process where sunlight is converted into chemical energy is called photosynthesis. Oxygenic photosynthesis, where water and carbon dioxide are converted into carbohydrates and molecular oxygen using sunlight, is mainly carried out by plants and certain algae [23]. However, sunlight is also used by bacteria to utilize other substrates such as quinones for chemical energy. The photosynthetic machinery of plants and bacteria is strikingly similar and proposed to stem from a common ancestor [24-27]. The photosynthetic apparatus in both plants and bacteria is composed of light-harvesting antennae which capture the incoming light and the inner core, the reaction center, where the charge separation event occurs. The energy generated in this process is then ultimately used for synthesis of ATP by another membrane protein, ATP synthase [28].

1.4.1 Overview of photosynthesis

In plants and algae (eukaryotes) photosynthesis is carried out in organelles called chloroplasts which have evolved from endosymbiosis with cyanobacteria [27]. The light-capturing molecules, or chromatophores, are located in the thylakoid membranes of the chloroplasts. In bacteria, which lack organelles, the photosynthetic reactions are instead carried out by proteins in the intracytoplasmic membrane [29]. The inner core, the reaction center, has a similar architecture in both plants and bacteria and is composed of a pair of (bacterio)chlorophyll molecules called the special pair which is where the charge separation occurs, along with numerous co-factors such as additional chlorophylls and in bacteria bacteriopheophins and bacteriochlorophylls [30].

1.4.2 Photosystems I and II

In photosystem II (PSII), the oxidation of water to yield molecular oxygen takes place in a cluster consisting of four manganese ions, one calcium ion and one to two chloride ions, called the oxygen-evolving complex (OEC) [31]. Also present in PSII is a redox-active tyrosine (TyrZ) which links the special pair P_{680}^{+} to the manganese cluster and, in cooperation with a nearby histidine residue of subunit D1, participates in transferring the released protons to the aqueous phase [32]. The reaction centers of non-sulfur purple bacteria such as *Rhodobacter sphaeroides* and *Blastochloris viridis* show a high degree of structural homology to the D1 and D2 subunits of photosystem II. Therefore, due to their simple architecture, bacterial reaction centers are often used as model systems for oxygenic photosynthesis, despite the lack of water oxidation capabilities.

Photosystem I (PSI) utilizes a pair of chlorophyll *a* molecules as a primary donor, a chlorophyll monomer as a primary acceptor and a phylloquinone as a secondary electron acceptor [33]. PSI utilizes an iron-sulfur cluster, [4Fe-4S] that, unlike the non-heme iron in bacterial reaction centers, is functional in electron transfer. Structural studies of PSI [34] reveal that it, unlike PSII, bears more resemblance to the reaction center apparatus of green sulfur bacteria and heliobacteria, rather than that of purple bacteria [35].

1.5 Structure and function of the Reaction Center from the purple bacterium *Blastochloris viridis*

The reaction center from *Bl. viridis (*formerly *Rhodopseudomonas viridis)* was the first membrane protein structure solved using X-ray crystallography in 1984 [5, 36]. The structure shows that the RC_{vir} is a membrane-spanning protein consisting of four subunits (L, M, C and H). A number of co-factors are also associated with the protein; the special pair of bacteriochlorophylls (P_{960}), bacteriochlorophyll *b* (BChl), bacteriopheophytin (BPhe), menaquinone A (MQ_A) and ubiquinone B (UQ_B), a non-heme iron (Fe^{2+}) and four hemes (Figure 2).

In the native membrane, the reaction center of *Bl. viridis* is, unlike most other purple bacteria, surrounded only by a single type of light-harvesting complex (LH1) which captures the energy and transfers it to the reaction center (Figure 3). This energy transfer results in a charge separation between the special pair P_{960} and the primary quinone MQ_A (ps-ns time scale), which in turn leads to an electron transfer to the mobile quinone Q_B (on the µs-ms time scale) [32]. During this transfer, P_{960}^+ is re-reduced by the cytochrome *c* subunit and is ready for a new charge separation event. After a second photon is absorbed by the special pair and transferred to the Q_B, two protons are taken up from the cytoplasm and Q_B is released as QH_2 into the membrane. As for most systems, only the L (right) branch is active in electron transfer [32].

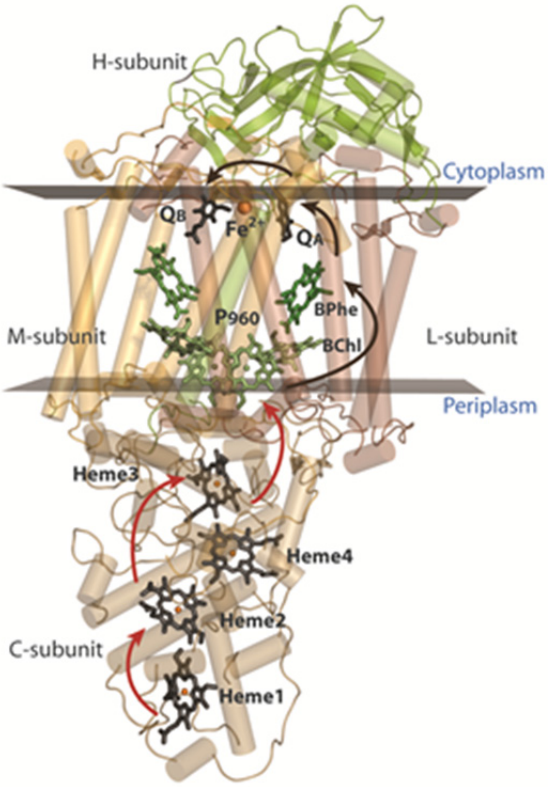

Figure 2. *Overview of the structure of reaction center from* Blastochloris viridis *(RC_{vir}). The four subunits are shown together with the co-factors. The black arrows starting from P_{960} show the light-driven charge separation reactions. The re-reduction of the special pair P_{960} is performed by Heme1, Heme2 and Heme3, as indicated by red arrows.*

The tetraheme subunit cytochrome *c* is then re-reduced after giving up one electron to the special pair by a cyclic flow of electrons *via* cytochrome bc_1 and the soluble carrier c_2. As a consequence of this coupled electron transfer, two protons per photon are pumped (Figure 3) and the resulting transmembrane potential difference is subsequently used by ATP synthase to generate ATP [37].

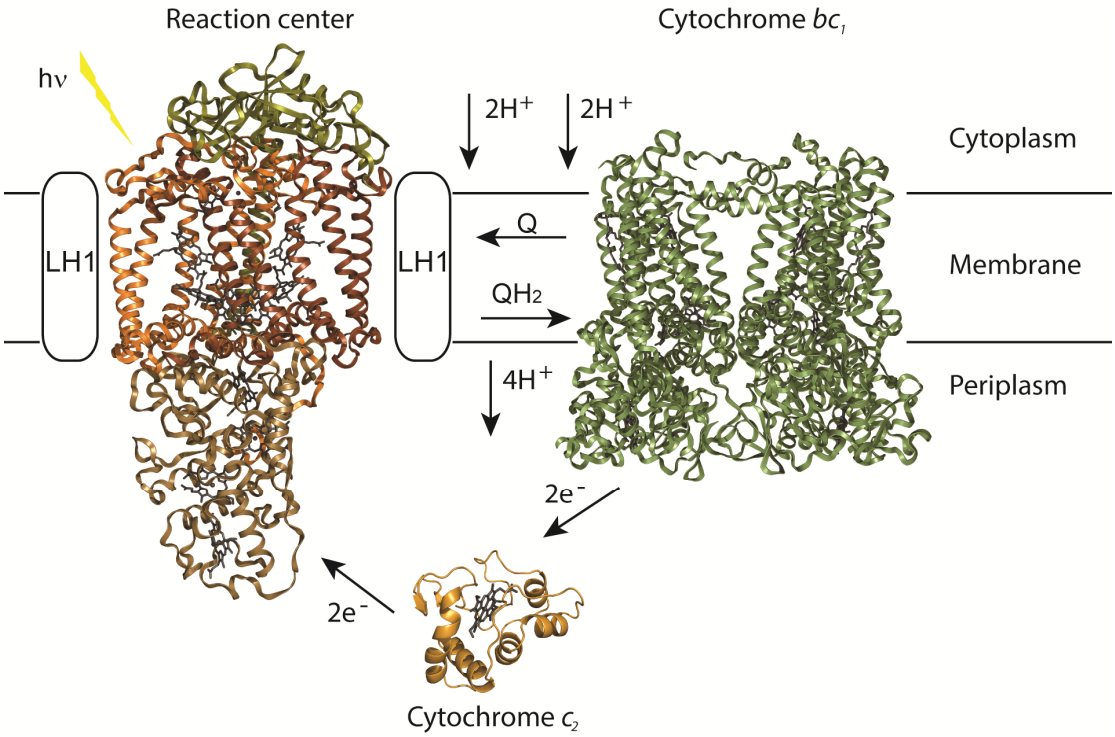

Figure 3. *A schematic representation of the electron flow and proton pumping in purple bacteria. The reaction center of* Blastochloris viridis *(RC_{vir}) is surrounded by a single type of light harvesting complex (LH1). RC_{vir} is coupled to the cytochrome* bc_1 *complex via the ubiquinone-ubiquinol pool in the membrane. A quinone molecule (Q) is photoreduced in the Q_B binding pocket of RC_{vir} to QH_2 and diffuses to the membrane to cytochrome* bc_1 *complex, where it is re-oxidized (and two protons per cycle are deposited on the periplasmic site).The structure of LH1 has not been yet been solved.*

1.6 Scope of the thesis

The aim of the thesis has been to develop new techniques for elucidating the structure and function of membrane proteins. A novel crystallization method has also been developed and used successfully throughout the work presented here.

The lipidic crystallization approach was explored by the development of a lipidic sponge phase (LSP) crystallization screen directed towards membrane proteins. It was tested on eleven different proteins of which eight gave crystal leads (**Paper II**). This, now commercially available screen, consists of 48 different conditions based on lipids, precipitants, salts and a pH range successfully used for membrane protein crystallization.

The usefulness of the screen was further demonstrated when one of the conditions was used for crystallization of the reaction center of the purple bacterium *Blastochloris viridis* (RC_{vir}) (**Paper III**). Two structures were obtained using different radiation doses and the structures were solved to 1.86 Å and 1.95 Å resolution. A novel space group and crystal packing was found for the two structures, along with a number of lipids bound to the protein surface.

A time-resolved Laue experiment was conducted on crystals obtained by using the RC_{vir} crystallization conditions from Papers II and III. This study (**Paper IV**) revealed a reproducible movement of the highly conserved TyrL162 residue toward the special pair upon photoactivation. These results were combined with molecular dynamics studies to propose a coupling between the conformational orientation and protonation states within a bacterial reaction center.

In preparation for the large amounts of crystals needed for X-ray free electron experiments at the Linac Coherent Light Source, the crystallization conditions obtained in Papers II and III, were further developed to yield microcrystals using an LSP batch crystallization method. Data were collected using an experimental setup limiting the maximum resolution to 7.4 Å. In **Paper V**, the 8.2 Å resolution structure of RC_{vir} obtained from only 265 images is presented.

With the advent of the Coherent X-ray Imaging (CXI) beamline at the LCLS, high-resolution data could be collected. Hence, the batch microcrystallization conditions were optimized to increase diffraction quality. These crystals were found to diffract beyond 2.8 Å and a SFX structure was solved to 3.5 Å resolution which is presented in **Paper VI**.

2 Methodology

2.1 Production and purification of reaction center from *Bl. viridis*

The non-sulfur purple bacterium *Blastochloris viridis* was first characterized in 1966 [38] and its cytoplasm was found to contain photosynthetic membranes arranged in stacked layers reminiscent of those present in higher plants [39]. The reaction center protein can be harvested directly from the photosynthetic membranes and has been extensively studied using a variety of spectroscopic and X-ray techniques, shedding light on one very fundamental process occurring in nature.

2.1.1 Cultivation procedures

Bl. viridis is a versatile bacterium which can be cultivated under both microaerophilic (low oxygen atmosphere) and anaerobic conditions as described by Lang and Oesterhelt [40]. Under photosynthetic growth conditions, the bacteriochlorophyll *b* concentration is inversely proportional to light intensity, while under microaerophilic conditions, a high concentration of oxygen is limiting for the growth rate (and low oxygen concentration limiting respiratory functions) [40].

2.1.2 Purification

Purification of membrane proteins from a cell involves a number of steps. The cell wall must be removed to expose the inner membranes, the protein of interest must be extracted from the membrane with the use of detergent and the solubilized protein must then be purified for crystallization experiments.

The first step involves disruption of the outer cell wall by either mechanical means with a sonicator, French press or X-press [41] or enzymatic methods, usually with help of lysozyme [42, 43]. The cell walls are then removed by centrifugation and the inner membranes, where the protein of interest is located, are pelleted using ultracentrifugation.

The membrane protein needs to be carefully removed from the membrane by use of detergents. A detergent consists of a polar headgroup with a hydrophobic tail which arranges itself in a micelle surrounding the protein. The concentration of detergent where the individual detergent monomers self-associate into micelles is known as the critical micelle concentration (CMC). All buffers used for purification of the solubilized protein must contain a detergent concentration above the CMC or the protein will fall out of solution (precipitate).

There are many different kinds of detergents with different tail lengths and compositions of the headgroup. The stability of a specific protein in a detergent is of outmost importance, thus it is advisable to perform a detergent screen prior to purification to ensure compatibility between the protein and the detergent. Commonly used detergents for purification are n-dodecyl-β-D-maltopyranoside (DDM), n-octyl-β-D-glucopyranoside (β-OG) and for RC_{vir} the zwitterionic detergent lauryldimethylamine-N-oxide (LDAO) has been successfully used in all purification (and crystallization) steps.

Once the protein is solubilized, contaminants such as other proteins or lipids are removed using chromatography. Usually the protein is subjected to a series of chromatography steps. If an affinity tag is present in the protein, it is passed through the appropriate affinity column followed by ionic exchange (based on the isoelectric point of the protein) and finally a polishing step using size-exclusion chromatography (SEC), where the homogeneity (purity), size and monomeric state of the protein is assessed.

2.2 Crystallization

A protein crystal is usually large enough to be visible in a light microscope, but the individual protein molecules within the crystals remain invisible. The physical resolution limit using a microscope is $\lambda/2$, i.e. half the wavelength of the incoming light. The wavelength used in light microscopy is 400-700 nm, thus the smallest items which can be seen are around 200 nm. An individual protein molecule is usually in the range of 30-100 Å (corresponding to 3-10 nm) and individual atom and atomic distances are in the range of 1-3 Å (0.1-0.3 nm), meaning that a traditional microscope cannot be used to visualize atoms or even individual protein molecules.

To view individual atoms, a shorter wavelength, X-rays, must be used. This type of radiation was discovered by Wilhelm Conrad Röntgen in 1895 and has since been used to determine the three-dimensional structure of various salts, proteins and other compounds. However, despite having the correct wavelength, X-rays can neither be used as a microscope to magnify the protein crystal through the use of lenses, nor are they powerful enough to visualize a single molecule. Instead the use of X-rays for structure determination relies on using proteins arranged in a highly repetitive unit, a crystal, to use constructive interference as a way of magnification. Protein crystals typically contain 10^{12}-10^{14} molecules which are arranged in a three dimensional lattice. The smallest repeating unit of a crystal is called a unit cell and is repeated by translation throughout the crystal. The unit cell can be subdivided further into the asymmetric unit, which is the smallest possible unit which can be rotated or translated according to the symmetry operators to represent the entire unit cell.

2.2.1 Protein crystal growth

Determining optimal conditions for protein crystallization can take a long time, sometimes years and this process is highly iterative, where crystallization trials are performed, evaluated and further optimized until well-diffracting crystals and a high resolution structure are obtained.

Usually, a drop of protein is mixed with a drop of precipitant and left to equilibrate over a reservoir solution (vapor diffusion, section 2.2.3.1). The drop will start to lose water to the reservoir and as a result the protein and precipitant concentrations in the drop will increase and the nucleation zone will be reached, where small nuclei will form. As a consequence, the protein concentration in the solution will decrease and the system will move into the metastable zone where crystal growth (but not formation) will occur (Figure 4).

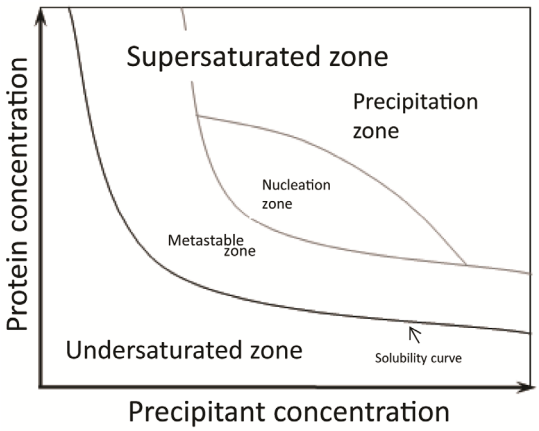

***Figure 4**. A two-dimensional solubility diagram for protein crystallization. Crystal nucleation will occur in the nucleation zone and as a consequence the concentration of free protein molecules will decrease, leading to the system moving into the metastable zone where crystal growth (but not nucleation) occurs. The solubility curve divides the undersaturated zone from the supersaturated zone, which is comprised of the precipitation, nucleation and metastable zones.*

If the concentration of the protein and/or precipitate is too high, the system will end up in the precipitation zone, where the protein forms an amorphous precipitate lacking order and therefore is unsuitable for an X-ray experiment. On the other hand, if the concentrations of protein and/or precipitate are too low, the system will reach the undersaturation zone, where the protein will remain in solution and no crystal formation will occur (Figure 4).

The growth of protein crystals are influenced by a number of different factors such as purity, concentration of protein, choice of precipitant, salt, pH, temperature and also the ratio between protein and the chosen precipitant solution. The drop should be investigated on a regular basis using a microscope and the appearance of the drop should be noted, along with crystal size, shape and quantity if crystals have formed. The quality of a crystal is investigated using an X-ray beam and if a crystal is found to be of insufficient quality, new crystallization experiments need to be performed to find more optimal conditions for crystal growth and diffraction.

2.2.2 Crystallization techniques for membrane proteins

Crystallization of a membrane protein is usually a highly repetitive task and the rate of success is based on the number of different parameters being investigated. Usually, a number of trials are carried out and their outcome is evaluated whereby decisions are taken about the subsequent steps. Usually after several iterations, with intermediate screening rounds at synchrotrons and alterations of the crystallization conditions, well-diffracting crystals might start to appear from which the structure can be obtained.

There are several techniques which can be used for membrane protein crystallization. The most common one is vapor diffusion where purified protein is mixed with a precipitant solution and allowed to equilibrate against a reservoir solution. Lately, a number of challenging targets have been crystallized by incorporation of the protein into membrane-mimicking lipids, a method known as lipidic cubic phase (LCP) crystallization. Also, a number of other lipid-based crystallization methods have been developed such as the lipidic-sponge phase (LSP) methods which is a swollen LCP and the bicelle crystallization method which can be described as a hybrid of lipid- and detergent- based crystallization.

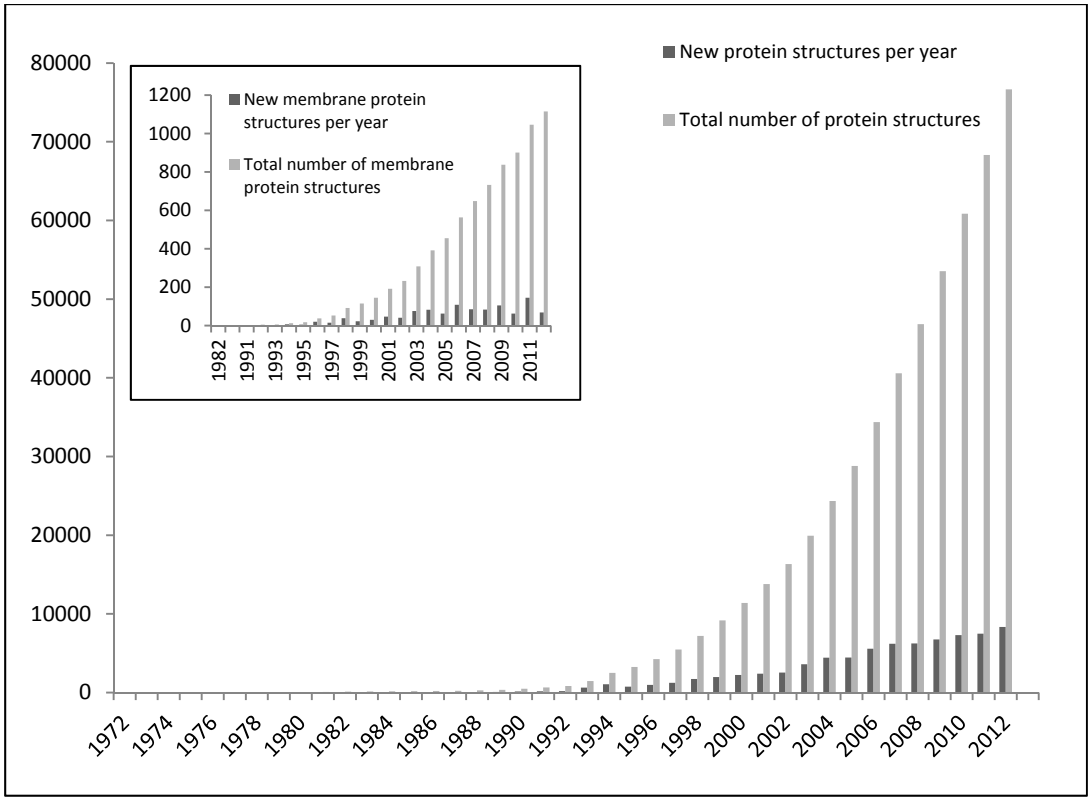

Figure 5. *Graph over the total number of protein structures and protein structures per year obtained between 1972-2012 (published in the protein data bank (PDB) [44]). The insert graph shows the corresponding growth of known membrane proteins (membrane protein data bank [6]). Only a small fraction (1-2%) of all protein structures in the Protein Data Bank (PDB) are membrane protein structures (insert). Note that these are not unique protein structures.*

2.2.2.1 Vapor diffusion

The most common method of protein crystallization is vapor diffusion where a drop of purified protein is mixed with a drop of precipitant solution on a cover slide and left to equilibrate against a reservoir solution containing the same precipitant. It can be performed in a variety of arrangements, the most common ones being hanging drop and sitting drop as shown in Figure 6.

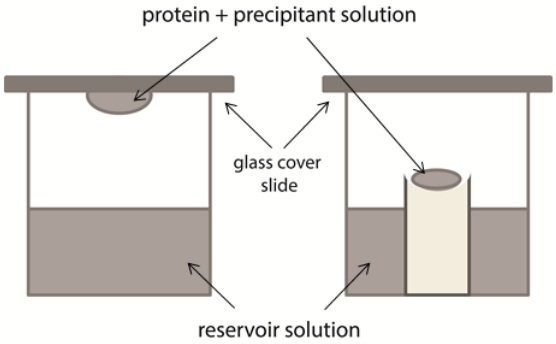

Figure 6. *Schematic representation of different types of vapor diffusion experiments. Left: hanging drop, right: sitting drop. The glass cover slides are usually sealed on top of the well using grease to provide an air-tight container. Water will evaporate from the drop to the reservoir solution over time.*

The principle behind the two experiments is the same: since the osmolarity in the precipitant solution is higher than in the protein drop, water will evaporate from the protein drop into the precipitant solution. Crystal growth usually occurs within a few

days up to a week but can be slower or faster depending on the protein and precipitant combination.

Robotic setups are often used together with commercial crystallization screens in the initial stages of screening. Once a promising condition is found, it is further optimized by changing the precipitant concentration, pH or adding other substances until a condition giving well-diffracting crystals is found.

2.2.2.2 Lipidic cubic phase crystallization (LCP)

The cubic phase used for crystallization purposes is the phase present at 20-40 % water in the Monoolein-water phase diagram (Figure 7), which is found at a lipid and temperature between those of the lamellar L_α and inverse hexagonal phases (H_{II}) [45]. The lipidic cubic phase (LCP) can exist in three main types, Diamond (D, space group Pn3m), Gyroid (G, space group Im3m) and an additional primitive phase (P, space group Im3m), which all have the appearance of a highly viscous, semi-solid paste [46].

The LCP crystallization technique was first used for the membrane protein bacteriorhodopsin in 1996 by Landau and Rosenbusch [47]. Since then, the LCP method has been successfully used in crystallization of a variety of proteins including the reaction center from *R. sphaeroides* [48], bacteriorhodopsin [49], sensory rhodopsins [50-52], halorhodopsins [53], channel rhodopsin [54], heme-copper oxidases [55, 56], several G-protein coupled receptors [57-71], along with other proteins [72-74] summarized in Table 1 and **Paper I**.

An LCP for membrane protein crystallization purposes is formed by reconstituting the protein into Monoolein in a 60:40 (w/w) of Monoolein:protein ratio. Formation of the LCP is spontaneous and can be carried out by mixing using a pair of syringes until a transparent phase is formed. The resulting, highly viscous LCP is then transferred to a vial or a sandwich plate, overlaid with precipitant solution and left to equilibrate. The LCP is not at equilibrium at temperatures below 20°C and could potentially turn into the solid lamellar crystal phase (L_c) which is unsuitable for crystallization purposes [75]. The LCP crystallization can thus only be performed at room temperature.

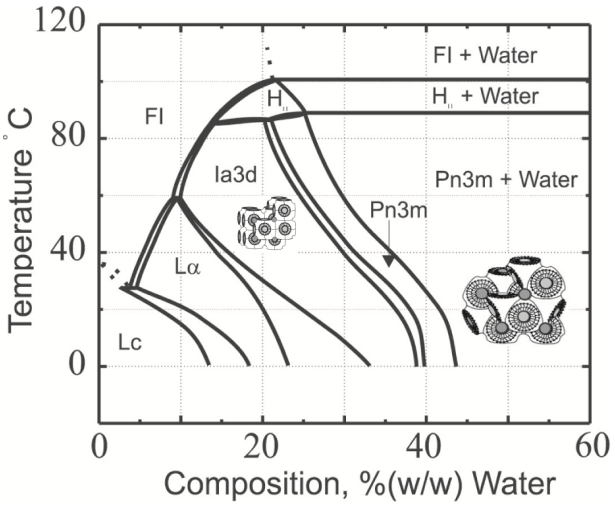

Figure 7. *Two-dimensional water-temperature phase diagram of the Monoolein-water system. Ia3d and Pn3m are cubic phases with different space groups (inserts). LCP crystallization is only possible at room temperature since the LCP will turn into a solid lamellar crystal phase (L_c) which is unsuitable for crystallization at lower temperatures. Figure adapted from [75].*

During crystallization trials, the LCP is usually overlaid with a salt-containing precipitant solution. The LCP crystallization mechanism is thought to proceed via a salt-induced local lamellar phase in which the protein molecules can diffuse laterally, nucleate and subsequently form a crystal [46, 76, 77]. The potential of the highly viscous LCP has been further exploited by the introduction of LCP-robots [78, 79] which are capable of high throughput crystallization trials, as well as the development of microfocus beamlines enabling data collection from micron-sized LCP-grown crystals [80].

2.2.2.3 Lipidic sponge phase crystallization (LSP)

The lipidic sponge phase (LSP or L_3 phase) is a method derived from the LCP and is prepared by swelling the LCP by addition of a third component such as PEG, MPD, PG ethanol, Jeffamine M600, DMSO (dimethyl sulfoxide) or NMP (N-methyl-α-pyrrolidone) [81]. The degree of swelling is dependent on the properties of the third component and the different phases obtained can be mapped in a phase diagram, such as in Figure 8. Upon closer examination of the PEG-water-Monoolein phase diagram, it can be deduced that addition of 30-40 % PEG will swell the LCP system and form an LSP [81]. The swelling increases the aqueous pore diameter up to three times [81], depending on the precipitant. Contrary to the LCP, the larger aqueous domains of the LSP allow membrane proteins with larger hydrophilic domains to be incorporated into the phase. Potential drawbacks common to both systems are that only room temperature (20°C) crystallization is possible, since the system will revert to a lamellar crystalline phase at lower temperatures [82] and moreover a pH above 9.0 is detrimental to the system since this will cause hydrolysis of the ester bond present in Monoolein [83].

The main conceptual difference in preparation of the LSP compared to the LCP is that the protein is *not* reconstituted into Monoolein prior to crystallization. Instead, the LSP is prepared in advance by mixing the three components buffer (water in the phase diagram), Monoolein and precipitant solution in the correct ratios. The LSP is then equilibrated at approximately 37°C until a homogenous, non-birefringent, transparent phase is formed. Furthermore, unlike the LCP, the LSP can be described as a liquid and can be used in a standard vapor diffusion experiment (both robot and manual setups), or used in vials or sandwich plates (as described for LCP) with or without (a batch type of experiment) reservoir solution.

Harvesting of crystals from the LSP phase is standard procedure and no lipase need to be added to dissolve the lipid phase as is the case sometimes for LCP-grown crystal harvesting [84].

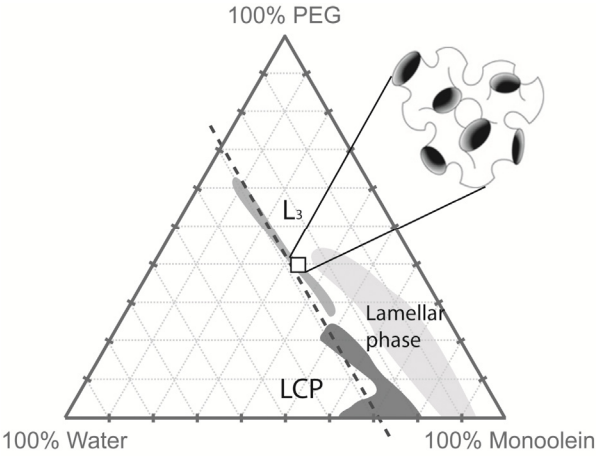

Figure 8. *The PEG-water-Monoolein phase diagram. The lipidic sponge phase, (LSP or L_3 phase) is present at a constant hydration level of about 30 % (indicated by a dotted line). Other phases are also present such as the lamellar and lipidic cubic phase (LCP), although at a higher Monoolein content.*

The LSP has been successfully used to crystallize several membrane proteins: Reaction center from *Rhodobacter sphaeroides* [85], light-harvesting complex II [76], the cobalamin transporter BtuB [86] and the reaction center from *Blastochloris viridis* (**Paper III-VI**) [87]. Moreover, several LCP structures obtained from conditions containing about 40 % PEG 400 have also been proposed to proceed *via* an LSP (summarized in **Paper I** and in Table 1).

2.2.2.4 Bicelle crystallization (Paper I)

Another recently developed method is that of bicelle crystallization. It was successfully used by Faham and Bowie in 2002 to crystallize and solve the structure of Bacteriorhodopsin [88]. Bicelles are formed by mixing the detergent 3-(cholamidopropyl)dimethylammonio-2-hydroxy-1-propane-sulfonate (CHAPSO) (other detergents can also be used [89]) with lipids dimyrisoyl phosphatidylcholine (DMPC) and dihexanoyl phosphatidylcholine (DHPC). The mixture is then subjected to cycles of vortexing and heating and cooling on ice. A viscous, homogenous liquid should be formed. The bicelle is then mixed with protein, vortexed and left on ice for insertion of protein into the bicelle. The bicelle-protein mix is then used for crystallization experiments. Since the behavior of bicelles is temperature-dependent (analogous to both LCP and LSP), formation of a gel occurs at higher temperatures (20-37°C), which is a prerequisite for crystallization to occur. Thus, as for all lipid-based crystallization methods, only room temperature crystallization is possible [90]. The bicelle method has been used to crystallize a number of different proteins including the β-barrel protein voltage-gated anion channel (VDAC1) [91], Xantorhodopsin [92], the LeuT transporter [93], the rhomboid protease [94] and one G-protein coupled receptor, the β2 adrenergic receptor [95].

Protein	Resolution (Å)	Source	PDB entry	Method	Year	Lipidic phase structure
Bacteriorhodopsin	2.50	*H. salinarum*	1AP9	LCP	1997	Pebay-Peyroula *et al.*
Halorhodopsin	1.80	*H. salinarum*	1E12	LCP	2000	Kolbe *et al.*
Sensory rhodopsin II	2.10	*N. pharaonis*	1H68	LCP	2001	Royant *et al.*
Sensory rhodopsin II-transducer complex	1.94	*N. pharaonis*	1H2S	LCP	2002	Gordeliy *et al.*
Reaction center	2.35	*R. sphaeroides*	1OGV	LCP	2003	Katona *et al.*
Anabaena Sensory Rhodopsin	2.00	*Nostoc sp. pcc 7120*	1XIO	LCP	2004	Vogeley *et al.*
Engineered human β_2 adrenergic receptor	2.40	*Homo sapiens*	2RH1	LCP*	2007	Cherezov *et al.*
OpcA outer membrane adhesin	1.95	*N. meningitidis*	2VDF	LCP*	2008	Cherezov *et al.*
Human A_{2A} adenosine receptor	2.60	*Homo sapiens*	3EML	LCP*	2008	Jaakola *et al.*
CXCR4 Chemokine receptor	2.50§	*Homo sapiens*	3ODU	LCP*	2010	Wu *et al.*
Dopamin D3 receptor	3.15	*Homo sapiens*	3PBL	LCP*	2010	Chien *et al.*
ba_3 cytochrome c oxidase	1.80§	*T. thermophilus*	3S8F	LCP*	2011	Tiefenbrunn *et al.*
Histamine H1 receptor	3.10	*Homo sapiens*	3RZE	LCP*	2011	Shimamura *et al*.
M2 muscarinic acetylcholine receptor	3.00	*Homo sapiens*	3UON	LCP	2012	Haga *et al.*
Channelrhodopsin light-gated cation channel	2.30	*C .reinhardtii*	3UG9	LCP	2012	Kato *et al.*
M3 muscarinic acetylcholine receptor	3.40	*Rattus norvegicus*	4DAJ	LCP	2012	Kruse *et al.*
μ-opioid receptor	2.80	*Mus musculus*	4DKL	LCP	2012	Manglik *et al.*
Kappa opiod receptor	2.90	*Homo sapiens*	4DJH	LCP	2012	Wu *et al.*
Sodium/Calcium Exchanger	1.90	*Methan.jannaschii*	3V5U	LCP	2012	Liao *et al.*
caa3 cytochrome c oxidase	2.36	*T. thermophilus*	2YEV	LCP	2012	Lyons *et al.*
Intimin	1.85	*E. coli*	4E1S	LCP	2012	Fairman *et al.*
Invasin	2.25	*Y. pseudotuberculosis*	4E1T	LCP	2012	Fairman *et al.*
Outer membrane porin	1.90§	*E. coli*	3POQ	LCP	2012	Efremov *et al.*
Neurotensin receptor	2.80	*Rattus novergicus*	4GRV	LCP	2012	White *et al.*
δ-opioid receptor	3.40	*Mus musculus*	4EJ4	LCP	2012	Granier *et al.*
Nociceptin/orphanin FQ receptor	3.00	*Homo sapiens*	4EA3	LCP	2012	Thompson *et al.*
Protease-activated receptor 1	2.20	*Homo sapiens*	3VW7	LCP	2012	Zhang *et al.*
Sphingosine 1-phosphate $S1P_1$ receptor	2.80	*Homo sapiens*	3V2Y, 3V2W	LCP	2012	Hanson *et al.*
Reaction center	2.20	*R. sphaeroides*	2GNU	LSP	2006	Wadsten *et al.*
Light harvesting complex II	2.45	*Rps. Acidophila*	2FKW	LSP	2006	Cherezov *et al.*
BtuB	1.95	*E. coli*	2GUF	LSP	2006	Cherezov *et al.*
Reaction center	1.86§	*Bl. viridis*	2WJN	LSP	2009	Wöhri *et al.*
Bacteriorhodpsin	2.00	*H. salinarium*	1KME	Bicelle	2002	Faham *et al.*
β_2-Adrenergic G-protein-coupled receptor	3.40/3.70	*Homo sapiens*	2R4R	Bicelle	2007	Rasmussen *et al.*
Voltage-dependent anion channel	2.30	*Mus musculus*	3EMN	Bicelle	2008	Ujwal *et al.*
Xantorhodopsin	1.90	*S.ruber*	3DDL	Bicelle	2008	Luecke *et al.*
Rhomboid protease	1.70	*E.coli*	2XTV	Bicelle	2011	Vinothkumar
Leu-T transporter	2.50§	*Aquifex aeolicus*	3USG	Bicelle	2012	Wang *et al.*

* Originally reported as LCP crystallization, but likely to have proceeded via LSP due to the PEG400 concentration; § Highest resolution reported

Table 1. *Summary of deposited membrane protein structures solved using LCP, LSP and bicelle methods between the years 1997-2012.*

2.3 X-ray diffraction and structure determination: theoretical considerations

2.3.1 X-ray diffraction theory

Diffraction from a three dimensional crystal is observed when irradiation with X-rays occurs. The radiation is scattered by the electrons within the crystals and interference occurs due to the regular three-dimensional arrangement within the crystal lattice. However, most waves cancel out each other due to negative interference and only those waves which fulfill the reflection conditions, also known as Bragg's law, will give rise to reflections:

$$n\lambda = 2dsin\theta \qquad \text{Equation 1}$$

where n is the order of diffraction, λ is the wavelength of the radiation, θ is the angle between the incoming beam and the lattice plane and d is the distance between the lattice planes (Figure 9). This means that the content of the unit cells is not taken into consideration and the reflection only depends on the lattice (the space group and the cell dimensions). Since only a few reflections will fulfill the reflection conditions, the crystal is rotated and images collected so as to cover the entire reciprocal space.

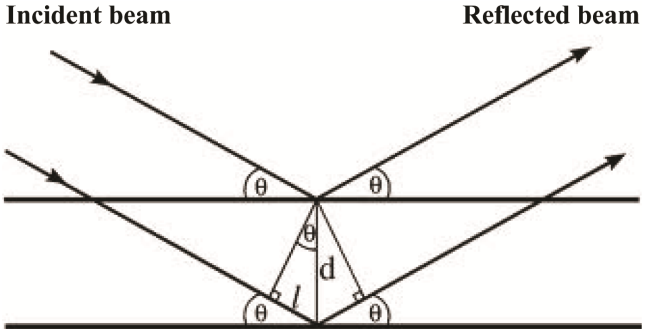

Figure 9. *Illustration of Bragg's law. The incident X-ray beam (with wavelength λ) is reflected in the lattice plane.*

The measured intensities contain information about the unit cell contents, i.e. the electron density which in turn provides information about the atomic positions. However, the information provided at a diffraction experiment is insufficient since only intensities are given and not the phases, according to the following equation describing the electron density $\rho(x,y,z)$ at position x,y,z in the unit cell using the Fourier transformation of the structure factor:

$$\rho(x,y,z) = \frac{1}{v}\sum_h\sum_k\sum_l |F_{hkl}| e^{-2\pi i(hx+ky+lz)+i\alpha(hkl)} \qquad \text{Equation 2}$$

where v is the volume of the unit cell, h k and l are the Miller indicies, F_{hkl} the absolute value of the structure factor for the corresponding hkl reflection. Experimentally, only $|F_{hkl}|^2$ can be measured and thus the phase information ($i\alpha(hkl)$) is lost, something which is referred to as the *phase problem* of crystallography.

2.3.2 Structure determination

After data collection, the reflections are indexed, meaning that their positions and h, k, l indices are assigned, followed by determination of space group. The spot intensities (I) are then integrated and the background estimated as σ(I). Various parameters such as beam intensity, crystal size, detector sensitivity and radiation damage need to be taken into consideration and the data is therefore scaled. The integrated values of the images are combined into one set of structure factors, normalized and merged.

2.3.3 Molecular replacement

Data collected in an X-ray diffraction experiment is lacking phase information and thus this data cannot be used to directly calculate the electron density. There are a variety of methods for obtaining these initial phases. The phases can be obtained by *de novo* methods such as SAD and MAD (single and multiple anomalous diffraction, respectively) [9] or SIR and MIR (single and multiple isomorphous replacement, respectively) [96]. If high resolution data (<1.2 Å) is obtained, *ab initio* methods for phase determination can be utilized for smaller proteins [97].

However, the most commonly used method for solving structures is molecular replacement (MR). This method relies on using phases from a similar structure to solve the phases using the Patterson function:

$$P(u,v,w) = \frac{1}{v}\sum_{h}\sum_{k}\sum_{l}\left|\mathrm{F_{hkl}}\right|^2 \times \cos\left[2\pi(hu+kv+lw)\right] \qquad \text{Equation 3}$$

If a part of the structure is known, such as a single domain of a multiple domain structure, there will be a correlation between the Patterson maps of the model and the target structure. The protein can be placed in the unit cell using rotation and translation and from this the initial phases can be obtained. The method of molecular replacement has been successfully used to determine the structure of RC_{vir} from data obtained from monochromatic, time-resolved Laue and X-ray free-electron laser experiments presented in this thesis.

2.3.4 Structure refinement and validation

The phases obtained by using the methods mentioned in section 2.3.3 need to be optimized further to better fit the experimental data. Fourier transformation is used to calculate an initial electron density map from the experimental data and the phases. A model of the protein can then be built into the resulting electron density using a program such as COOT [98] . This model is then rebuilt and refined so as to fit the electron density, using manual real space refinement and automated refinement against the reflection intensities using programs such as REFMAC [99] or Phenix [100]. This is repeated until convergence between the model and the electron density is reached.

The crystallographic R factor is a measure of how well the model agrees with the data:

$$R = \frac{\sum_{hkl} \left\| F_{obs}(hkl) \right| - k \left| F_{calc}(hkl) \right\|}{\sum_{hkl} \left| F_{obs}(hkl) \right|} \qquad \text{Equation 4}$$

A complete agreement between the model and data would mean that F_{obs} and F_{calc} are identical and thus the R factor would be 0. The R factor is usually given in percent and in practice a value which is about 10 times the resolution is considered a reasonably good value. However, to reduce model bias and provide a means of cross-validation, Brunger introduced the R_{free} measure, where 5-10% of all reflections are excluded from refinement [101]. The R_{free} value should not deviate substantially from the R value, since this means that the quality of the model is poor or that the data is overinterpreted.

When phasing using molecular replacement, the initial phases can be biased towards the model rather than the experimental data. To evaluate this, parts of the model is omitted and a map is calculated (a so-called omit map). A good quality map should show the whole model, including those parts which were omitted. A more automated way of calculating an omit map is by using a computer program such as CNS [102] which omits one part of the structure per calculation and then combines them into what is known as a composite omit map.

When amino acids are combined into a polypeptide, only certain combinations of the dihedral angles Φ and Ψ of the backbone are allowed. A plot of Φ against Ψ is known as a Ramachandran plot and allows detection of amino acids with unusual (disallowed) conformations. These types of restraints are used for structure validation in the final stages of structural refinement.

2.3.5 Laue data processing

Laue data processing mainly differs from monochromatic structure determination in the way the images are indexed. As a consequence of the multiple wavelengths used in the diffraction experiments, so-called nodal spots form. These have a high multiplicity and usually are used as starting points for indexing. In the case of indexing the diffraction data from RC_{vir} crystals (**Paper IV**), laser damage frequently gave rise to very streaky spots, making images very difficult to index and data from several crystals therefore had to be merged to obtain a complete dataset.

2.3.5.1 Difference Fourier maps

Difference Fourier maps can be used to visualize small differences between two isomorphous derivatives of a protein with known crystal structure. The isomorphism can be a result of ligand or substrate binding, chemical modification, heavy atom positions or photoinduced differences [103-105]. This method provides a less biased approach than that of normal Fourier maps and enables detection of subtle features which differ between datasets.

A difference Fourier map is calculated using the crystallographic phases from the refined ground (resting) state data and only the amplitudes of the structure factors for the other structures need to be known. The maps are usually not further refined, but used directly for interpretation. The method was used to calculate the differences between a resting state and a photoactivated state in a time-resolved Laue experiment (**Paper IV**) and allowed movement of a single amino acid side chain within a large 135,000 Da protein to be detected.

2.3.6 Processing and evaluation of SFX data

The new technique of serial femtosecond crystallography (SFX) enables data collection from many small nano- or microcrystals and due to the exceptionally high X-ray intensity, only one image per crystal is collected. Since the crystal is not rotated during collection, only partial reflections are recorded. The SFX method of data collection has led to development of a new software suite, called CrystFEL [106], capable of handling partial reflections as well as the large amounts of data collected at an SFX experiment.

Patterns from individual crystal are indexed *via* the program Indexamajig (within the CrystFEL suite), which calls indexing programs such as DirAx [107] and MOSFLM [108]. The input file used is a list of filenames and for each image in this list, a peak search is performed and sent for autoindexing using the indexing programs (or alternatively peak lists in the image files can be used).

After indexing, the intensities are integrated from the predicted peak locations and merging of these individual intensity measurements from single crystals are performed using a Monte Carlo based approach developed by Kirian *et al*. [109]. During merging, the mean value of all measurements (for each individual reflection) is taken and a Monte Carlo integration over the three-dimensional reflection profile provides a value which is proportional to the integrated intensity.

2.3.6.1 SFX data quality assessment

Since SFX data relies on collection of one image per crystal, the traditional measure for data quality during X-ray diffraction data collection, R_{merge}, is not meaningful for this type of data. Instead, the SFX data is split into two sets, each which is merged separately and then compared with respect to the resulting intensity lists. Due to the fact that the data is split into two sets, the degree of convergence within each dataset is lower and therefore the quality of data is underestimated by a factor of $2^{1/2}$ (and this is corrected for in equation 5 below). Thus, the figure of merit is defined as:

$$R_{split} = 2^{-1/2} \frac{\sum \left| I_{even} - I_{odd} \right|}{\frac{1}{2} \sum \left(I_{even} + I_{odd} \right)} \qquad \text{Equation 5}$$

where I_{even} represents the intensity of a reflection produced by merging even-numbered patterns, I_{odd} represents the intensity of the equivalent reflection from the odd-numbered patterns and the sum is over all reflections ($I_{even} + I_{odd}$).

As a consequence, the error in the final estimate of the intensity of each reflection using the Monte Carlo method can be described as:

$$\sigma_{hkl} = \left[\sum \left(I_{spot} - \langle I_{hkl} \rangle \right)^2 \right]^{1/2} / N_{hkl} \qquad \text{Equation 6}$$

where I_{spot} is an individual measurement of the reflection hkl, $\langle I_{hkl} \rangle$ is the mean of all such measurements, N_{hkl} is the number of measurements and the summation is over all measurements of a particular reflection. As is apparent from the equation above, the error in the final estimate of the intensity will be large if the N_{hkl} is small.

2.4 Crystal mounting and handling

Protein crystals need to be transported from the lab to the synchrotron and mounted in the X-ray beam. The conventional method is to mount the crystal on a goniometer head and then align it in the beam. This is usually automated for cryo crystallography, while room temperature mounting often requires manual mounting and alignment. Moreover, the advent of X-ray free electron lasers has led to a development of a new type of crystal delivery using a liquid microjet.

2.4.1 Radiation damage and cryo crystallography

Radiation damage is a process where an electron is ejected from an atom upon the absorption of an X-ray photon. This leads to formation of radicals which can change the chemical and electronic properties of the atoms within the crystal, resulting in decreased diffraction power. Many radicals, particularly oxygen and hydroxyl, also diffuse and cause damage at other sites in the protein. By cooling a protein crystal to cryogenic temperatures, the mobility of the radicals can be slowed down prolonging the lifetime of the crystals in the X-ray beam. A cryogenically cooled crystal can survive a dose of about 30 MGy at a synchrotron facility [11].

Protein crystals contain a high content of solvent and freezing will therefore cause an expansion of water which may be damaging to the crystal. It is possible to overcome these problems by freezing the crystal quickly so that water remains in a glass-like state, or the crystals can be soaked in a solution containing a substance which protects it during freezing, known as a cryo protectant. The most commonly used cryo protectants are small, organic molecules such as glycerol or (poly) ethylene glycols (PEG) and the use of these speeds up the freezing process which protects the crystal from vitrification. However, if crystals are grown in a high concentration of organic molecules, or in a lipid phase such as the LCP, LSP or bicelle, no additional cryo protectants are usually necessary prior to freezing. A potential drawback to flash-freezing however, is an increase in mosaicity often occurring during the vitrification process [110]. The method of cryogenically cooling crystals is now widely used in the structural biology community, as it allows crystals to be stored and shipped safely to a synchrotron, where automated sample mounting can be used, allowing the user to collect data on site as well as at a remote location.

2.4.2 Room temperature crystal mounting

Room temperature collection can be used in crystallography when no suitable cryo protection conditions can be found, for treatment of extremely large crystals unsuitable for freezing or to measure data at physiologically relevant temperatures. Crystals intended for room-temperature data collection are transported in crystallization trays to the synchrotron where they are harvested and capped with polyester or quarts capillaries filled with mother liquor to prevent them from drying out and then manually mounted on the goniometer head. Other applications of room temperature data collection also includes the time-resolved Laue method which is used for studying rapid reactions occurring within a protein under near-physiological conditions.

2.4.3 Microjet delivery of microcrystals at an X-ray free electron laser

An XFEL such as the Linac Coherent Light Source (LCLS) operates at 120 Hz, meaning that the sample must be exchanged 120 times every second. To provide rapid sample exchange, a gas-driven liquid microjet is used. This produces a steady flow of liquid which is focused to a few micrometers using a gasflow. The crystal suspension is filtered and loaded into an HPLC or syringe delivery system which is used for transport up to the microjet nozzle placed perpendicular to the incoming XFEL beam in a vacuum chamber to minimize scattering from air. The resulting microjet stream of fully hydrated protein crystals then interact with the XFEL beam and give rise to diffraction patterns on the detector.

2.5 Data collection

Membrane protein crystals rarely diffract well and care needs to be taken during data collection to obtain the best possible data from a crystal. Parameters to take into account during data collection include resolution limits, redundancy, completeness and overlaps. Also, with increased X-ray exposure the crystal will decay due to the X-ray radiation and this leads to internal disorder in the crystal, something which can be reduced by collecting the data at cryogenic temperatures instead of at room temperature. An alternative method of reducing radiation damage is by using XFEL radiation with continuous replenishment of sample, collecting only one image per crystal.

2.5.1 Cryo-temperature monochromatic data collection

The most common way of collecting diffraction data is by using monochromatic radiation. This can be CuK_{α} radiation from an in-house source (λ=1.54 Å) or synchrotron radiation (wavelengths usually around 1 Å, often tunable). During data collection the crystal is rotated while being exposed to the X-ray radiation. The diffraction pattern is collected on a detector (most commonly a CCD detector which allows the spot intensities to be integrated). To avoid overlapping reflections, an image is collected after a small oscillation (typically 0.2-1.0°). Under optimal circumstances, a complete dataset is collected from a single crystal.

2.5.2 Laue diffraction experiment: the pump- probe technique

Time-resolved Laue diffraction can be used to follow reactions at near-physiological conditions. It uses a stationary crystal and takes advantage of the intense, pulsed polychromatic X-rays naturally emitted by a synchrotron and allows for much shorter

exposure times (about three to four magnitudes) compared to monochromatic data collection [111]. A single X-ray pulse at a modern synchrotron such as the European Synchrotron Radiation Facility (ESRF) can be as short as 100 ps in duration and is sequestered using a millisecond shutter and a high-speed chopper operating in series [112].

The pump-probe technique is commonly used for photoactivated time-resolved studies in both soluble and crystallographic systems. The principle can be divided into four steps: I) Light flash which induces the system (=pump); II) a time delay (t_{light}); III) the photoactivated state is probed by X-rays (=probe) and IV) a dark period which allows the system to relax back to its ground state (t_{dark}). There is also a step 0, where a dark image is collected prior to the first laser flash. This approach allows direct comparison between dark and light images in respect to systematic drifts and errors. After collection of one dark and one illuminated image, the crystal is either rotated or translated (or both) to a new position where the cycle is repeated. The use of a polychromatic beam allows for collection of a complete dataset using much fewer images. However, radiation and laser damage can severely diminish the diffraction power of the crystal and it is not uncommon that data from several crystals are needed to obtain a complete dataset.

2.5.3 Serial femtosecond crystallography at X-ray free-electron laser sources

Serial femtosecond crystallography (SFX) is a newly developed method based on collection of data from thousands of single, fully hydrated microcrystals which are injected into an XFEL beam using a liquid microjet [113]. The LCLS operates at 120 Hz [14] and can deliver X-rays with energies up to 20 keV per pulse with a peak brilliance a billion times stronger than that of a synchrotron. The extreme brilliance of the beam together with the extremely short pulses (a few to hundreds of fs in duration [15]) only allows one diffraction image to be collected per crystal before the onset of radiation damage [16]; the “diffraction before destruction” principle [13]. This means that the crystal is neither oscillated nor rotated during data collection and a complete dataset must therefore be obtained from thousands of randomly oriented crystals which poses additional challenges during data processing.

3 Lipid-based membrane protein crystallization: Papers II and III

Membrane proteins have proven difficult to crystallize despite major efforts in development of crystallization screens and other tools. The amphiphilic nature of membrane proteins requires the use of detergents as a means of stabilization during extraction from the native membrane and subsequent crystallization trials. An alternative method is to add back lipids during crystallization in an attempt to increase the stability. The most commonly used methods are the lipidic cubic phase (LCP) and its swollen equivalent, the lipidic sponge phase (LSP). By combining the LSP technology with commonly used salts, precipitants and a pH range of 5.5-9.0, a screen consisting of 48 different conditions was developed. All conditions were validated by small-angle X-ray scattering (SAXS) as well as crystallization trials, where eight out of eleven of the tested membrane proteins gave crystal leads. This screen was used together with an additive to determine two structures of the bacterial reaction center from *Blastochloris viridis* to 1.86 Å and 1.96 Å resolution (**Paper III**).

3.1 Development of a lipidic-sponge phase screen (Paper II)

In a previous experiment, it was discovered that the LCP used for crystallization of the reaction center from *Rhodobacter sphaeroides* (RC_{sph}) was liquefied upon addition of precipitant. The resultant lipid phase was further investigated and was proven to be a swollen LCP, or a lipidic sponge phase (LSP) [85]. These conditions, along with the successful crystallization of a GPCR in LCP [57], were combined with salts, precipitants and pH commonly used for membrane protein crystallization, to provide a starting point for the development of a lipidic-sponge phase based crystallization screen.

3.1.1 Preparation of LSP

Two commonly used precipitants (PEG and MPD) were used to prepare LSPs. Since the phase diagrams are available for these precipitants, they were prepared directly by weighing in molten Monoolein (MO) into small glass vials along with the appropriate amount of precipitant (PEG or MPD) and buffer solution. The vials were tightly sealed and incubated on a roller for about 24 hours at 37°C. In cases where the sample was not homogeneous after this treatment, it was heated to 50°C for 2–3 hours and then re-incubated at 37°C. Afterwards, the samples were centrifuged (20°C, 5500 × *g*, 35 min) and left until a transparent phase (non-birefringent under polarizing light) indicative of LSP was observed (Figure 10).

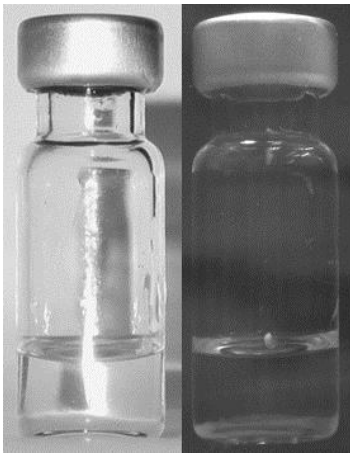

***Figure 10**. A PEG-containing non-birefringent lipidic sponge phase. Left: No polarization showing a homogenous phase; Right: under polarizers.*

Since the phase diagram for Jeffamine M600 is not available, these LSPs were prepared by swelling of an LCP. Monoolein and buffer (0.1 M Hepes pH 7.5) was mixed in a 60:40 volume ratio until a viscous, transparent and non-birefringent cubic phase was

formed. After transferring the LCP into a glass vial, 1 ml of sponge phase-inducing solution (15-20 % Jeffamine M600, 1 M Hepes pH 8.1, 0.7 M $(NH_4)_2SO_4$ and 2.5% 1,2,3-heptanetriol) was added. The sample was sealed and kept at room temperature until phase separation had fully occurred. After centrifugation (20°C, 5500 × *g*, 35 min), the upper phase containing the LSP was harvested. The LSP method can be extended further by addition of hydrophobic additives such as cholesterol, ubiquinone and soya bean asolectin directly into the phase at a final concentration of about 1 %.

3.1.2 Evaluation of the LSP conditions: SAXS measurements

SAXS can be used for determination of the space group of the LCP, but since the LSP lacks long-range order the SAXS measurements will only give one diffuse Bragg peak (Figure 11).

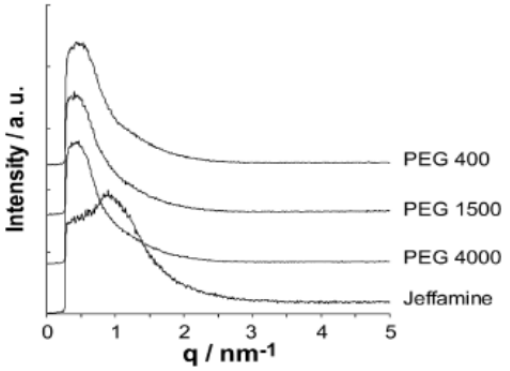

Figure 11. *Left: SAXS curves for PEG400, PEG1500, PEG4000 and Jeffamine M600. All four samples show the broad Bragg peaks at low q indicative of lipidic sponge phases.*

All LSP conditions which did not show any birefringence under polarizing light were examined using SAXS. A detector distance of 275 mm was used and the exposure time was typically 900 s for each sample. The temperature in the sample cell was kept at 20°C and the camera and sample cell were held under vacuum to minimize air scattering. The SAXS profiles were evaluated using 3D-View software and only those phases that showed a broad Bragg peak indicative of LSP were used for crystallization trials (section 3.1.3).

3.1.3 Testing the LSP crystallization kit: crystallization trials

The phases that showed the broad Bragg peak in the SAXS measurements were used in hanging drop vapor diffusion crystallization trials by mixing 1 µL LSP with 1 µL protein and equilibrating over a reservoir solution containing 0.55 M sodium acetate, 0.75 M HEPES, pH 6.3, 0.1 g/mL Na/K-PO_4 at 20°C.

Eleven different membrane proteins from both prokaryotic and eukaryotic sources were tested for crystallization (Table 2). Crystal leads were obtained for eight of these proteins: aquaporin from *Plasmodium falciparum* (PfAQP) and *Spinacia oleracea* (SoPIP2;1), complex II from *Bacillus subtilis* (BsSQR), the photosynthetic reaction centers from *Rhodobacter sphaeroides* (RC_{sph}) and *Blastochloris viridis* (RC_{vir}), the two light-harvesting complexes from *Rhodopseudomonas acidophila* ($LH2_{aci}$) and *R. sphaeroides* ($LH2_{sph}$) and the photosynthetic core complex from *Bl. viridis* (RC-$LH1_{vir}$) (Figure 12). No crystal leads were recovered from proteorhodopsin (pR), bacteriorhodopsin (bR), or ubiquinol oxidase (UbOx), something which can be attributed either to incompatibility with the LSP or to inconsistencies of protein preparation and quality.

	Protein	Source	Abbrev.	MW [kDa]	TM	Detergent	Protein conc. [mg/ml]	Crystallization conditions
1	Aquaporin	*Plasmodium falciparum*	PfAQP	30	6	DDM	10-15	30
2	Aquaporin	*Spinacia oleracea*	SoPIP2;1	30	6	β -OG	10-15	4
3	Complex II	*Bacillus subtilis*	BsSQR	120	6	Thesit	10-20	40
4	Proteorhodopsin	γ-proteobacterium	pR	27	7	β-OG, DDM	10-20	-
5	Bacteriorhodopsin	*Halobacterium salinarium*	bR	27	7	β -OG	7.5-12.5	-
6	Reaction center	*Rhodobacter sphaeroides*	RC_{sph}	100	11	LDAO	20-25	31, 36, 37, 43
7	Reaction center	*Blastochloris viridis*	RC_{vir}	135	11	LDAO	20-25	19, 31, 32, 36, 37
8	Light harvesting complex 2	*Rhodopseudomonas acidophila*	LH2	150	18	LDAO	5	25, 31, 38, 45
9	Ubiquinol oxidase	*Escherichia coli*	UbOx	144	25	DDM	10	-
10	Light harvesting complex 2	*Rhodobacter sphaeroides*	LH2	not known	not known	LDAO	5	4
11	Photosynthetic core complex	*Blastochloris viridis*	RC-$LH1_{vir}$	~440	~43	CHAPS	20-25	36

Table 2. *Summary of the eleven membrane protein tested in the lipidic sponge phase screen. For each membrane protein its source, molecular weight, number of transmembrane helices, purification detergent, protein concentration for crystallization trials and crystallization conditions are shown. Crystal leads were found for eight out of the eleven proteins tested.*

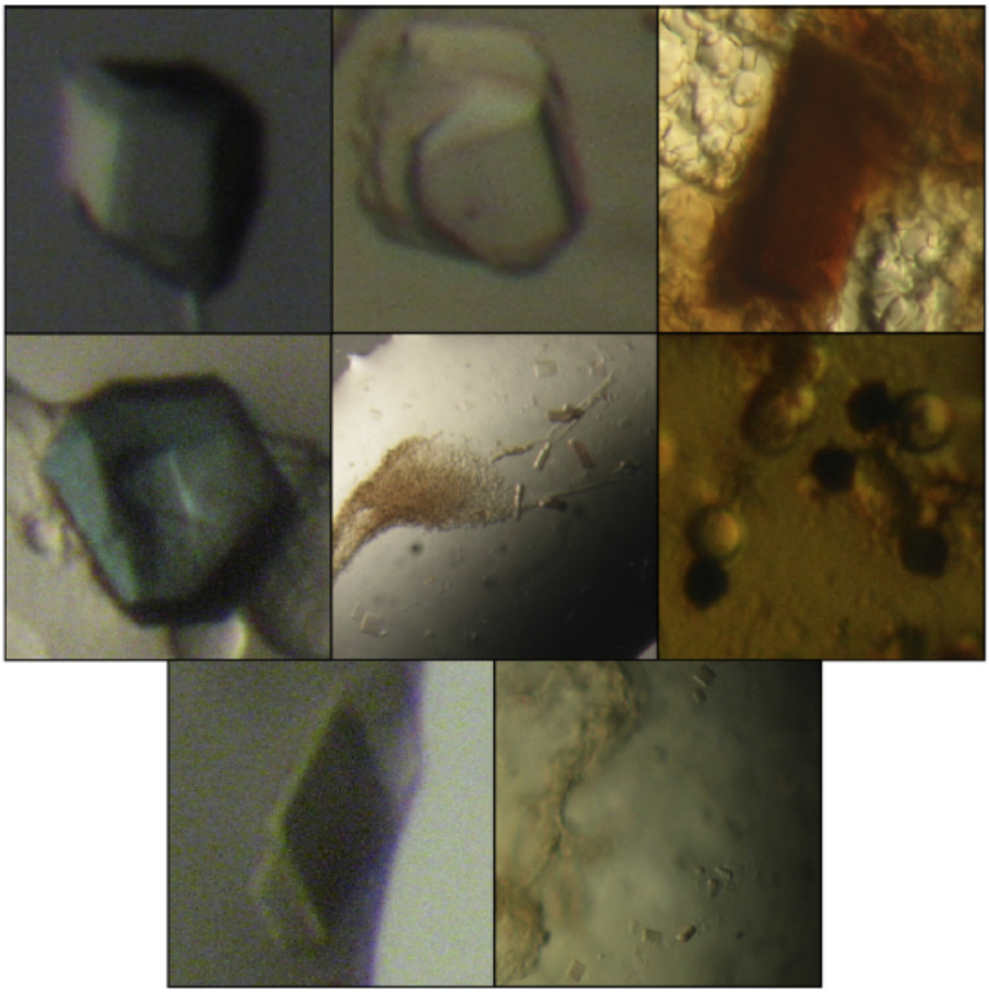

***Figure 12**. Crystal leads obtained using the lipidic sponge phase screen. Crystals were obtained from (top row, left to right) 1) Plasmodium aquaporin; 2) Spinach aquaporin; 3) Complex II from Bacillus subtilis. Middle row, left to right: 4) RC from Rhodobacter sphaeroides; 5) RC from Blastochloris viridids; 6) LHII from Rhodopseudomonas acidophila. Bottom row (left to right): 7) LH2 from R. sphaeroides and 8) RC-LH1 from Bl. viridis.*

A variety of different detergents were used to purify the proteins tested, including: lauryldimethylamine-N-oxide (LDAO), n-octyl-β-D-glucopyranoside (β-OG), n-dodecyl-β-D-maltopyranoside (DDM), polyoxyethylene (9) dodecyl ether (Thesit) and 3-([3-cholamidopropyl]-dimethylammonio)-1-propane sulfonate (CHAPS) and none lead to any deterioration of the LSP.

Colorless protein crystals can be difficult to distinguish from salt or detergent crystals and therefore it is advisable to always perform control crystallization experiments (without the protein). A false positive lead was found in one condition (number 21) out of the 144 conditions (Appendix 8.1).

3.1.3.1 RC_{vir}: optimization using additives

Initial hits of RC_{vir} were found in conditions 19, 31, 32, 36 and 37 of the screen and crystals were harvested without addition of cryo protectants. These crystals were

tested at a synchrotron and were found to diffract to about 3.5 Å resolution (Figure 13). These initial hits were then optimized using a commercially available Additive Screen HT (Hampton Research). Crystals were obtained using tri-sodium citrate as an additive and were found to diffract to about 1.7 Å resolution (Figure 13 and **Paper III**).

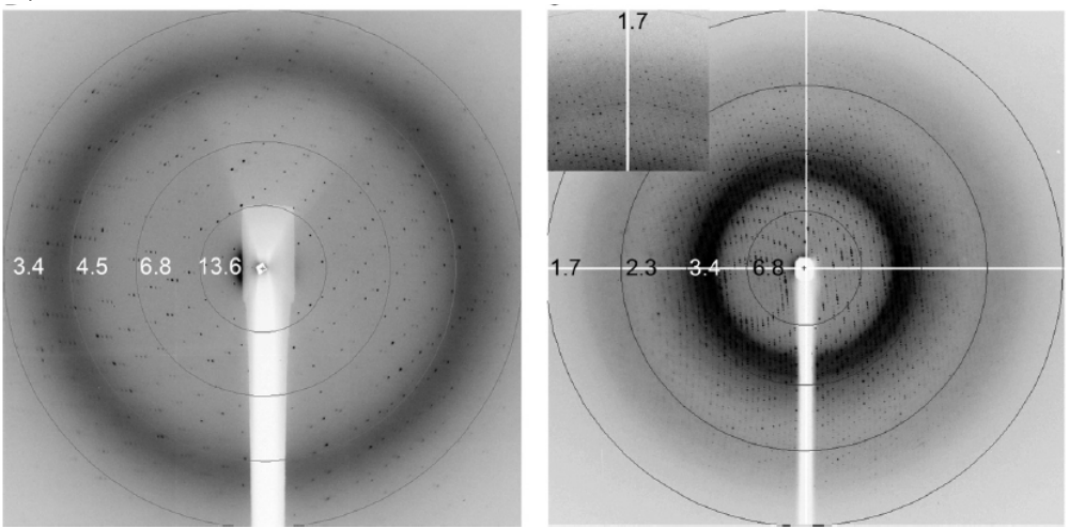

***Figure 13**. Optimization of RC_{vir} crystallization conditions. Left: RC_{vir} crystal leads obtained using the lipidic sponge phase screen diffracting to about 3.5 Å. Right: Improved diffraction of RC_{vir} crystals after using an additive screen, yielding diffraction to 1.7 Å resolution.*

3.1.4 The lipidic sponge phase crystallization kit

The selection of conditions to be included in the screen was based on the results of the SAXS measurements and whether or not crystal leads were formed in the crystallization trials. In total, 48 lipidic-sponge phase conditions were selected to form the crystallization screen and these are detailed in Appendix 8.1. Included in the kit is also a reservoir solution and instructions for use.

3.1.5 Summary Paper II

The aim of the study was to develop a commercial kit consisting of 48 different lipidic-sponge phases which could be used for membrane protein crystallization. The concept of the screen combines the idea of the lipidic sponge phase with standard crystallization conditions including a number of different salts NaCl, $MgCl_2$ and Li_2SO_4, different buffers (MES, Hepes and Tris covering a pH range of 5.5-9.0) and successful crystallization precipitant solutions PEG400, PEG1500 and PEG4000. The screen also includes conditions based on a previously successful crystallization condition: 1 M Hepes (pH 8.1), 15-20% Jeffamine M600, 0.7 M $(NH_4)_2SO_4$ and 2.5% 1,2,3-heptanetriol [85].

The conditions were confirmed to be lipidic sponge phases using SAXS and validated in hanging drop vapor diffusion crystallization trials testing in total eleven different membrane proteins. Out of these eleven conditions, eight gave crystal leads, where one of the leads (reaction center from *Bl. viridis*) was optimized to yield diffraction to 1.86 Å (**Paper III**). The resulting kit is commercially available and is compatible with both robots as well as manual setups and includes all 48 conditions along with reservoir solution along with instructions for storage and handling of the LSP.

3.2 Structure of *Blastochloris viridis* reaction center grown in LSP: Paper III

The RC_{vir} crystallization conditions obtained in the LSP crystallization screen were further optimized using tri-sodium citrate as an additive. Two datasets were obtained to 1.86 Å and 1.95 Å resolution, collected using different X-ray radiation doses. Unlike detergent-grown crystals, both crystals displayed a novel space group, type I packing and crystal contacts are mediated by a different loop in the H-subunit. A number of protein-lipid interactions were also reported. A diacylglycerol molecule was found to be bound at the N-terminal of the cytochrome *c* subunit, which is a common prokaryotic posttranslational modification. Moreover, a 36 Å long, unidentified lipid was present at the surface of the protein and the Q_B site was occupied by a Monoolein molecule instead of the native, mobile ubiquinone-9.

3.2.1 Cultivation and purification

Cultivation was performed as follows: cultures were grown in the dark for approximately 24-48 hours at 20°C and then transferred to photosynthetic light conditions where the temperature was 30°C for 24-48 hours. These cultures were then transferred to large 10 L bottles and the dark-light incubation process was repeated. The photosynthetically active cells were harvested after 48 hours.

The solubilization step was performed using a high concentration of LDAO (4 %), followed by anionic exchange and size exclusion chromatography using the same detergent, albeit at lower concentrations. The optical purity ratio (A_{280}/A_{830}) required for crystallization was approximately 2.1-2.8.

3.2.2 Crystallization of RC_{vir} in LSP

Crystals were grown using the LSP crystallization technique using 20 % Jeffamine M600. The upper LSP was harvested and 1 µL was used as a precipitant solution together with 1 µL of protein solution and 1 µL of additive 1 M tri-sodium citrate in a hanging-drop, vapor-diffusion experiment against a reservoir solution. The crystallization plates were stored in darkness at room temperature and diamond-shaped crystals appeared after two to three weeks, growing to a maximum size of 0.25 mm x 0.50 mm x 1.15 mm. The crystals were frozen directly in liquid nitrogen without the addition of cryo protectants.

3.2.3 The structure of reaction center from *Blastochloris viridis*

Two datasets of RC_{vir} were collected on LSP-grown crystals using different radiation doses. The low dose dataset was collected at the ESRF and the high dose at Swiss Light Source (SLS, about one order of magnitude higher X-ray dose, see Table 3). The structures were solved independently using molecular replacement and the crystals were found to belong to a new space group, $P2_12_12$. The structures were refined using iterative manual rebuilding in COOT [98], with refinement in REFMAC5 [99]. In the final stages of refinement, Translation Libration Screw motion (TLS) [114] refinement was used which resulted in an improvement of the R_{free} with about 2 %. The low dose dataset could be processed to 1.95 Å and the high dose to 1.86 Å (summarized in Table 3).

Data collection	Low-dose data set	High-dose data set
PDB entry	2WJM	2WJN
resolution (Å)[a]	45.9−1.95 (2.06−1.95)	45.0−1.86 (2.00−1.86)
space group	$P2_12_12$	$P2_12_12$
unit cell dimensions, *a*, *b*, *c* (Å)	84.5, 138.5, 177.8	84.8, 139.4, 178.2
total absorbed dose (Gy)	4.4×10^6	7.1×10^7
no. of unique reflections[a]	145,856 (18,911)	176,119 (34,206)
completeness (%)[a]	96.2 (86.4)	97.8 (92.1)
multiplicity[a]	4.3 (3.6)	6.6 (6.7)
Mean I/σ[a]	10.9 (2.1)	15.0 (3.7)
R_{sym} (%)[a]	8.9 (72.6)	6.8 (48.5)
R/Rfree (%)[c]	17.3/20.1	16.6/19.3
rmsd from ideal bond lengths (Å) /angles (deg)	0.017/2.1	0.018/2.3
no. of atoms (protein/waters/hetero)	9186/711/774	9175/692/723
Ramachandran plot (% by PROCHECK)		
most favored	92.0	92.4
additionally allowed	7.5	7.1
generously allowed	0.4	0.4
disallowed	0.1	0.1
average *B*-factors (Å^2)	33.0 ± 6.1	37.0 ± 6.8
Protein[b]	32.6 ± 4.5	36.6 ± 5.2
waters	37.3 ± 8.8	44.4 ± 10.5
all other heteroatoms	34.2 ± 13.8	35.5 ± 13.3
diacylglycerol	66.1 ± 8.1	
monoolein 1 (at Q_B site 70% occupancy)	42.8 ± 4.1	47.0 ± 6.1
monoolein 2	55.7 ± 1.6	64.2 ± 1.2
monoolein 3	59.6 ± 12.5	64.0 ± 4.4

[a]Values in parentheses indicate statistics for the highest resolution shell; [b]Residual *B*-factors after TLS refinement.

Table 3. *Data collection and refinements statistics for the low and high dose datasets.*

3.2.4 Crystal packing and contacts

Both structures were found to pack in stacked 2D layers (type I packing), which is commonly found in lipid-grown crystals. However, in contrast to a previously published structure of lipid-grown RC_{sph}, no crystal contacts are observed within the membrane plane [48].

Upon comparison with a detergent-grown crystal structure (PDB entry 2PRC) [115], residues 46-60 of the H-subunit were not visible in the electron density compared to the detergent-grown structure. This region is involved in crystal contacts between neighboring symmetry-related molecules in the detergent-based crystals, but were disordered in the LSP-grown form. Instead, crystal contacts in the LSP-grown form are mediated by residues 80-85 of the H-subunit, which deviate about 6.5 Å from that of the detergent- grown form (Figure 14).

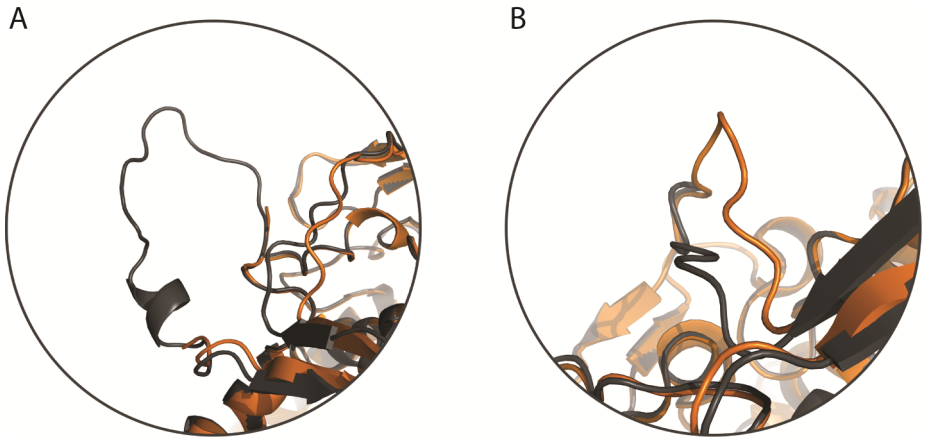

Figure 14. *An overlay between the detergent-grown (grey) and LSP-grown RC_{vir} structures (orange). A) Shows the loop H46-H60 (grey) of the detergent grown crystals involved in crystal contacts; B). Shows the loop H80-H85 of the LSP-grown structure involved in crystal contacts (orange).*

3.2.5 Diacylglycerol covalently bound at the cytochrome *c* subunit N-terminal: a prokaryotic posttranslational modification

A diacylglycerol molecule was found to bind an N-terminal cysteine residue of the cytochrome *c* subunit. This has been previously established by masspectrometry studies [30] and is a type of prokaryotic posttranslational modification facilitating the association of the cytochrome *c* subunit to the membrane. A similar, but reversible, form of posttranslational modification can be seen in eukaryotes, where thioacylation on cysteine residues have regulatory functions for a number of membrane proteins including the G-protein coupled receptor in complex with G-protein [116].

Upon comparison between high dose and low dose RC_{vir} datasets, the high-dose dataset displays a reduced occupancy of diacylglycerol in the electron density, as a result of specific radiation damage to the thioether bond connecting the diacylglycerol molecule to the N-terminal cysteine, as evident by the lack of continuous electron density for this feature.

3.2.6 Unidentified 36 Å lipid moiety at the surface of RC_{vir}

A 36 Å continuous electron density feature was found to be bound between the transmembrane helix of the H-subunit, the L-subunit and the co-factors of the L-branch. This lipid has in previously published RC_{vir} structures been modeled as LDAO molecules [115], or in RC_{sph} structures, as cardiolipin [117-121]. However, in the two structures it has been modeled as phosphate ions, since the identity of the lipid is yet to be identified (Figure 15C).

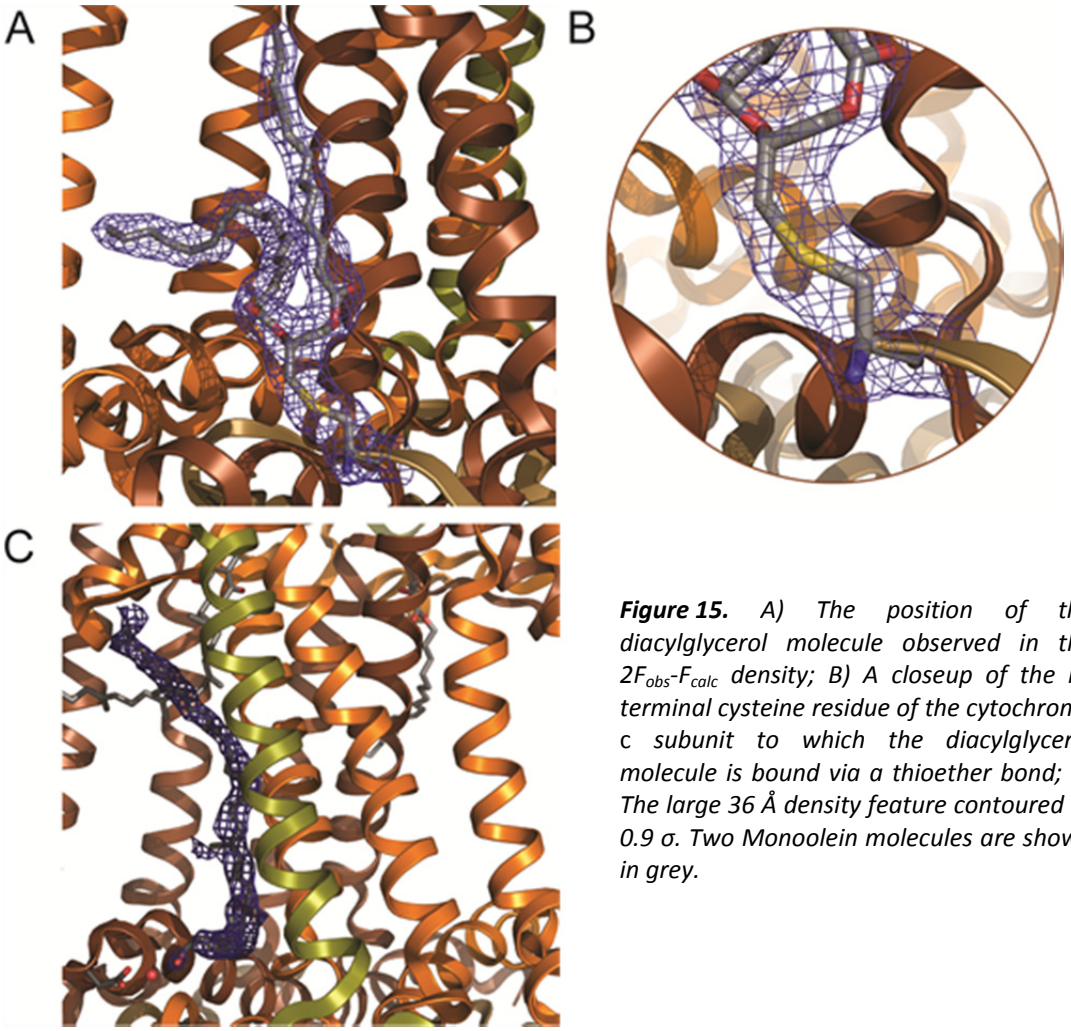

Figure 15. *A) The position of the diacylglycerol molecule observed in the $2F_{obs}$-F_{calc} density; B) A closeup of the N-terminal cysteine residue of the cytochrome c subunit to which the diacylglycerol molecule is bound via a thioether bond; C) The large 36 Å density feature contoured at 0.9 σ. Two Monoolein molecules are shown in grey.*

3.2.7 Monoolein found in three positions including the Q_B binding pocket

In both the high and low dose data sets, Monoolein was found to be present in the Q_B site instead of the ubiquinone usually found in RC_{vir} structures [122, 123]. It could be placed in the Q_B pocket without any residual F_{obs}-F_{calc} density.

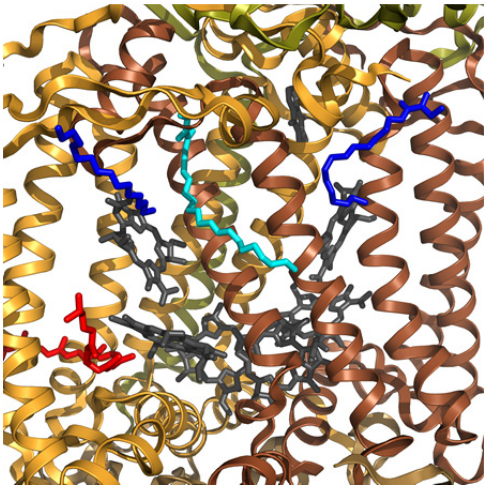

Figure 16. *Figure of the overall arrangement of lipids in the high-dose structure of RC_{vir}. The Monoolein bound in the Q_B binding pocket is shown in cyan. Two Monoolein molecules were also found outside the Q_B binding pocket, shown in dark blue. The diacylglycerol molecule is shown in red.*

The L- subunit is shown in brown, the M-subunit in yellow and the H- subunit in green. The C -subunit is not shown. Co-factors are shown in grey (tails are omitted for clarity).

The hydrogen bonds between the hydroxyl groups of the headgroup and the surrounding amino acids were also satisfied. The fatty acid tail of Monoolein was fully visible on the protein surface, indicating that hydrophobic binding interactions in RC_{vir} are not selective (Figure 16).

3.2.8 Summary Paper III

In this paper, two structures of the reaction center from *Blastochloris viridis* grown in the lipidic sponge phase are presented. The two datasets were collected using high and low X-ray doses and could be processed to 1.86 Å and 1.95 Å resolution, respectively. The paper demonstrates that a protein with large hydrophilic domains is suitable for crystallization in the lipidic sponge phase, rather than the lipidic cubic phase which has a limited pore size. The structures revealed a novel space group ($P2_12_12$) compared to all other RC_{vir} structures deposited in the protein data bank and showed a type I crystal packing typical of crystals grown in lipidic phases.

Upon comparison with other structures grown in detergent-based crystallization conditions, residues 46-60 of the H-subunit were found to be disordered in the LSP-structures. This loop is involved in crystal contacts between neighboring protein molecules in the detergent-grown structure. In the LSP-grown structures, the crystal contacts are instead mediated by another loop consisting of residues 80-85 of the H-subunit.

The two structures also displayed a number of lipid-protein interactions. A diacylglyerol molecule was detected on an N-terminal cysteine in the cytochrome *c* subunit acting as a posttranslational modification by facilitating association of the cytochrome *c* subunit to the membrane. In the high-dose dataset, the thioether bond anchoring the diacylglycerol to the N-terminal cysteine residue was affected by radiation damage, showing a discontinuous difference electron density. Furthermore, a 36 Å long lipid moiety was discovered in the density of the high-dose dataset. However, no known lipid was found to fit into the density and instead two phosphate ions were modeled in its place. Moreover, Monoolein molecules were found in several locations, including the Q_B binding site where a ubiquinone molecule usually is found.

4 Time-resolved Laue crystallography studies of the reaction center from *Blastochloris viridis*: Paper IV

The idea behind a time-resolved crystallographic Laue experiment is to induce a reaction in the crystal by a laser flash and probing it with a polychromatic X-ray beam. This approach to studying conformational changes upon photoactivation requires robust crystals capable of withstanding both laser and X-ray radiation damage. In this study, time-resolved Laue crystallography was applied to the membrane protein reaction center, revealing a reproducible movement of a highly conserved Tyrosine residue toward the special pair upon photoactivation. The crystallographic results were combined with molecular dynamics studies providing a model of how conformational orientation and protonation states are coupled in bacterial reaction centers.

4.1 Time-resolved crystallography studies of proteins: different approaches

The most common way of studying reaction intermediates in protein crystals is by freeze trapping. This method involves generation of the state of interest, such as a catalytically relevant intermediate state, followed by flash freezing of the crystal. Another method is the time-resolved Laue diffraction experiment, where polychromatic synchrotron X-rays are utilized for probing structural changes as a response to a reaction initiated by a short laser pulse. This approach enables collection of several complete, high-resolution datasets from various time-points, thus producing a "molecular movie" of the protein in action instead of individual intermediate states such as in the freeze trapping approach.

Several soluble proteins have been used as model systems for Laue crystallography. The photodissociation and rebinding of carbon monoxide (CO) to myoglobin [124-126], hemoglobin [127] and the photoactive yellow protein (PYP) [128, 129] have all been studied achieving a time-resolution of 100 ps to 5 ns. Membrane proteins are usually difficult to crystallize which poses additional challenges to time-resolved studies and only one a time-resolved Laue experiment has been performed on membrane proteins prior to our study, by Baxter *et al.* in 2004 [10].

4.1.1 Structural changes in reaction centers from *R. sphaeroides* and *Bl. viridis*

In 1997, Stowell and colleagues performed a freeze trapping study on crystals of the reaction center from *R. sphaeroides* [130]. Light-induced changes in the RC_{sph} could be obtained by comparing the dark-adapted state of the crystals (at cryogenic temperatures) with the light-adapted state which had been cooled to cryogenic temperatures under illumination. These structures were refined at 2.2 Å and 2.6 Å resolution respectively and upon comparison between the two structures the most prominent finding in the light-adapted state was a 4.5 Å movement of the ubiquinone towards the cytoplasm, accompanied by a 180° propeller twist of the quinone isoprene tail [130]. The freeze trapping data thus suggests that at low temperatures (90 K) the electron transfer from Q_A to Q_B is completely blocked when RC_{sph} is cooled in the dark, whereas the electron transfer proceeds when RC_{sph} are frozen during illumination. This led Stowell and colleagues to hypothesize that, based on the structural evidence, the ubiquinone can adopt two positions; one where electron transfer from Q_A is inhibited (dark state, distal binding site) and one

where it is not (light state, proximal binding site); thus implying that the movement of the quinone from the distal site to the proximal position is a prerequisite for electron transfer from Q_A to Q_B. However, the photoinduced movement of the quinone from the distal to the proximal position remains controversial, mainly because the dark and illuminated datasets were collected using different crystals; something which does not exclude the possibility that the quinone occupied the proximal binding site even before illumination. Several studies, including Fourier Transform Infrared Spectroscopy (FTIR) [132-134] and crystallographic studies on both RC_{vir} [123] and RC_{sph} [131] indicate that the quinone occupies the proximal binding site, or a position intermediate of that of the proximal and distal sites, in both the dark and illuminated states [135-137].

Baxter and colleagues performed a similar experiment to that described above on the reaction center from *Blastochloris viridis*, using a time-resolved Laue approach. The aim was to investigate if the Q_B pocket exhibited the same type of behavior regarding the distal and proximal binding of the ubiquinone molecule. However, refinement showed that the ubiquinone only was found in the proximal position (equivalent to the dark state for the RC_{sph} experiment) and that no significant changes upon illumination could be detected [10].

4.2 Time-resolved Laue crystallography studies on LSP- grown RC_{vir} crystals

In the experiment by Baxter *et al.* no conclusions about conformational changes in the Q_B binding site could be drawn [10]. Therefore, due to the excellent crystal quality and low mosaicity of the RC_{vir} crystals grown in the LSP, the time-resolved Laue experiment was repeated at the beamline ID09B at the ESRF in an attempt to elucidate potential structural changes accompanying ubiquinone reduction in the Q_B binding pocket.

4.2.1 Crystallization of RC_{vir} and crystal mounting at room temperature

Crystals were obtained using the LSP in hanging drop vapor diffusion setups as described in section 3.3.3. In an attempt to increase the occupation of ubiquinone in the Q_B pocket, ubiquinones with two different tail-lengths were used independently in crystallization trials, UQ2 and UQ9. Crystals (approximately 0.25 mm x 0.50 mm x 1.15 mm in size) were brought to European Synchrotron Radiation Facility (ESRF) in crystallization trays and were harvested using a nylon loop. To prevent the crystals from drying out during data collection, a capillary (quartz or polyester) filled with mother liquor was mounted on the cap base and sealed with wax just prior to the diffraction experiment.

4.2.2 Laser excitation and data collection

Time-resolved room-temperature (293K) Laue data collection was performed at beamline ID09B at the ESRF with the storage ring operating in 24x8+1 hybrid bunch mode. Laue diffraction data were collected using X-ray pulses 86 µs in duration without illumination (laser off) and 3 ms following laser photo activation (laser on) a new image was collected using the same oscillation angle, allowing direct comparison of images with respect to systematic errors in the data. The crystal was then rotated and the cycle was repeated. In an attempt to increase the lifetime of

the crystal, it was translated 100 µm along the axis of rotation to a new position and data collection was repeated.

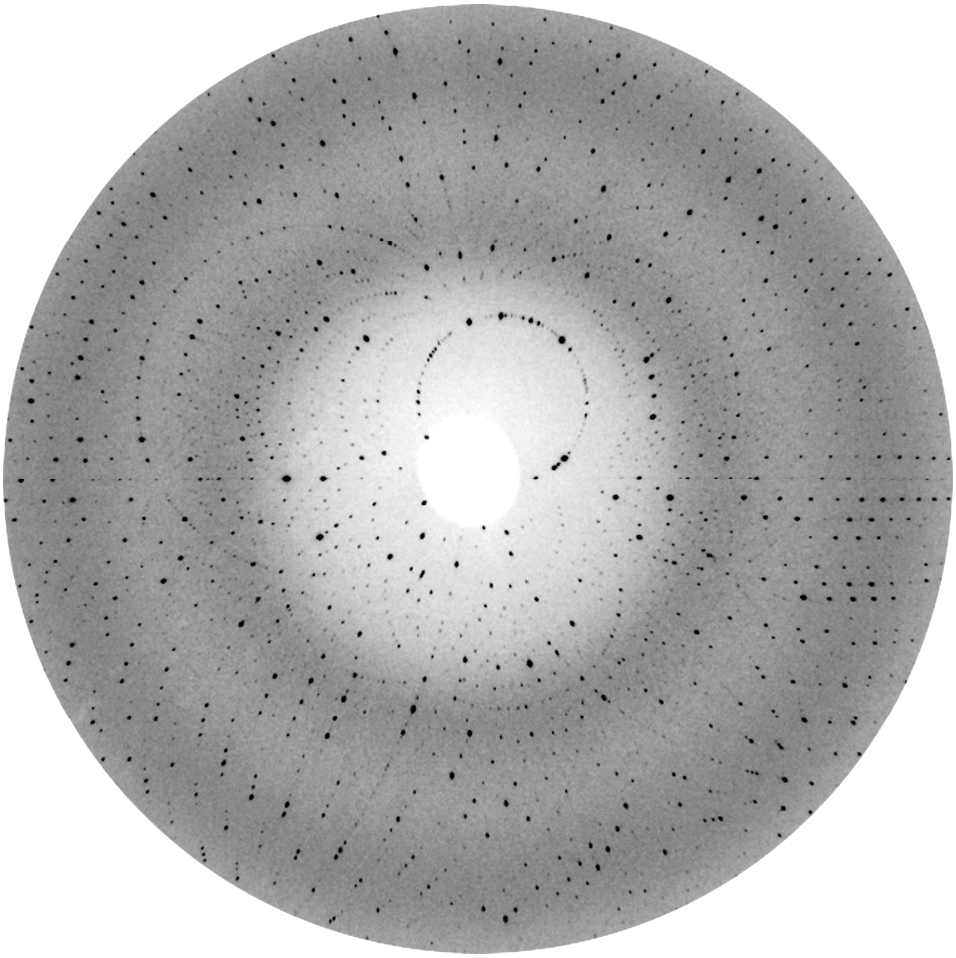

***Figure 17**. Laue diffraction pattern of an LSP-grown RC_{vir} crystal obtained using a single polychromatic 86 µs exposure collected at beamline ID09B at the European Synchrotron Radiation Facility.*

4.2.3 Processing and refinement of Laue data

Time-resolved Laue diffraction data were indexed and integrated using the program Precognition™ (Renz Research, Inc.) and scaled with Epinorm (Renz Research, Inc.).

Several datasets were collected, but not all could be processed as a result of radiation damage as may be expected during room temperature data collection. Furthermore, many of the photoactivated images were severely affected by laser damage. Three datasets were found to be of sufficient quality to be processed and were scaled together to increase the completeness. As a result, two high-completeness Laue diffraction data sets were recovered, with the dark and the photo-activated state data having a completeness of 91.3 % and 90.6 %, respectively. The structure was solved using molecular replacement and both models were further refined using rigid body and restrained refinement (see Table 4 for data collection and refinement statistics).

4.2.4 Fourier difference density maps

Calculation of a F_{light}-F_{dark} difference Fourier map can be used to investigate structural changes occurring due to photoactivation. Difference Fourier maps were calculated for each pair of laser off and laser on datasets and the structure factor amplitudes from each of the states were scaled together (independently) using SCALEIT. The phases were calculated from the model obtained from refinement against merged dark state Laue diffraction data (91.3% complete, Table 4).

The resulting difference density Fourier maps for the three datasets were quantified by evaluating the 100 strongest negative and 100 strongest positive peaks within the individual maps (Appendix 8.2). Only peaks which were within 3.5 Å search radius were considered reproducible. The strongest reproducible positive and negative peaks detected in the Fourier difference density map were found to be associated with Tyrosine 162 of the L- subunit (TyrL162) (Figure 18). These paired positive and negative densities are indicative of a conformational change happening around the TyrL162 side chain on the 3 ms timescale. However, similarly to a previously published study [10], no paired positive and negative densities corresponding to changes in or around the Q_B site were found within the top 100 peaks and it is therefore unlikely that such a movement occurred during this experiment.

To verify the results, TyrL162 was modeled to a position corresponding to that found in the difference Fourier maps, with 35% occupancy in accordance with the spectroscopic measurements of the P_{960}^{+} state. $(F_{light}-F_{dark})_{theoretical}$ Fourier maps at 2.95 Å were then calculated from the photoactivated and resting states. The shape and size of the positive and negative peaks from the theoretical calculations correspond to those of the experimental difference Fourier maps (Figure 19).

Data collection	***Dataset 1***		***Dataset 2***		***Dataset 3***		***Merged dataset***	
	resting state	photo-activated state	resting state	photo-activated state	resting state	photo-activated state	resting state	photo-activated state
Wavelength [Å]	0.8-1.1	0.8-1.1	0.8-1.1	0.8-1.1	0.8-1.1	0.8-1.1	0.8-1.1	0.8-1.1
Data range [Å]	61.8-2.8	42.2-2.8	45.7-2.5	45.7-2.5	46.2-2.8	46.2-2.8	61.8-3.0	46.2-3.0
Observations	177950	167254	241696	239076	200218	194620	-	-
Unique reflections	23005	21618	31309	30904	25853	24970	40855	40530
Redundancy	7.7	7.7	7.7	7.7	7.7	7.7	-	-
R_{merge} on F^2 [%][a]	17.1	18.7	13.1	18.6	13.3	16.5	15.4	18.0
R_{merge} on |F| (%)[b]	9.8	10.3	7.4	10.4	7.7	9.3	8.8	10.0
Resolution [Å]	2.95	2.95	3.00	3.00	3.00	3.00	3.00	3.00
Completeness [%][c]	49.9 (33.5)	46.9 (29.1)	71.5 (49.6)	70.2 (51.1)	59.0 (37.8)	57.0 (35.0)	91.3 (75.9)	90.6 (74.2)
Mean I/σ[c]	11.8 (8.5)	9.9 (6.8)	14.9 (10.0)	10.2 (7.6)	13.9 (8.2)	11.4 (6.8)	12.9 (8.6)	10.4 (6.9)
Laser energy [µJ][d]	-	300	-	130	-	2x165	-	-
Diff. Fourier map completeness (%)	43.4		57.5		51.7		87.0	
No. of atoms in model							9790	9808
R_{factor} [%][e]							25.0	27.7
R_{free} [%][f]							28.4	31.9

[a] $R_{merge}=\Sigma|F^2-\langle F^2\rangle|/\Sigma F^2$, where F^2 is the mean of multiple observations and symmetry related measurements.

[b] $R_{merge}=\Sigma||F|-\langle|F|\rangle|/\Sigma|F|$

[c] Values in parentheses indicate statistics for the highest resolution shell.

[d] Dataset 3 has been illuminated with two subsequent laser pulses each 165 µJ with 3 ms interval.

[e] $R_{factor} = \sum||F_{obs}|-|F_{calc}||/\sum|F_{obs}| \times 100\%$

[f] For the R_{free} calculation a random selection of approximately 5% of the data were assigned and was not included in the refinement.

Table 4. *Table of X-ray data collection and refinement statistics for datasets 1-3.*

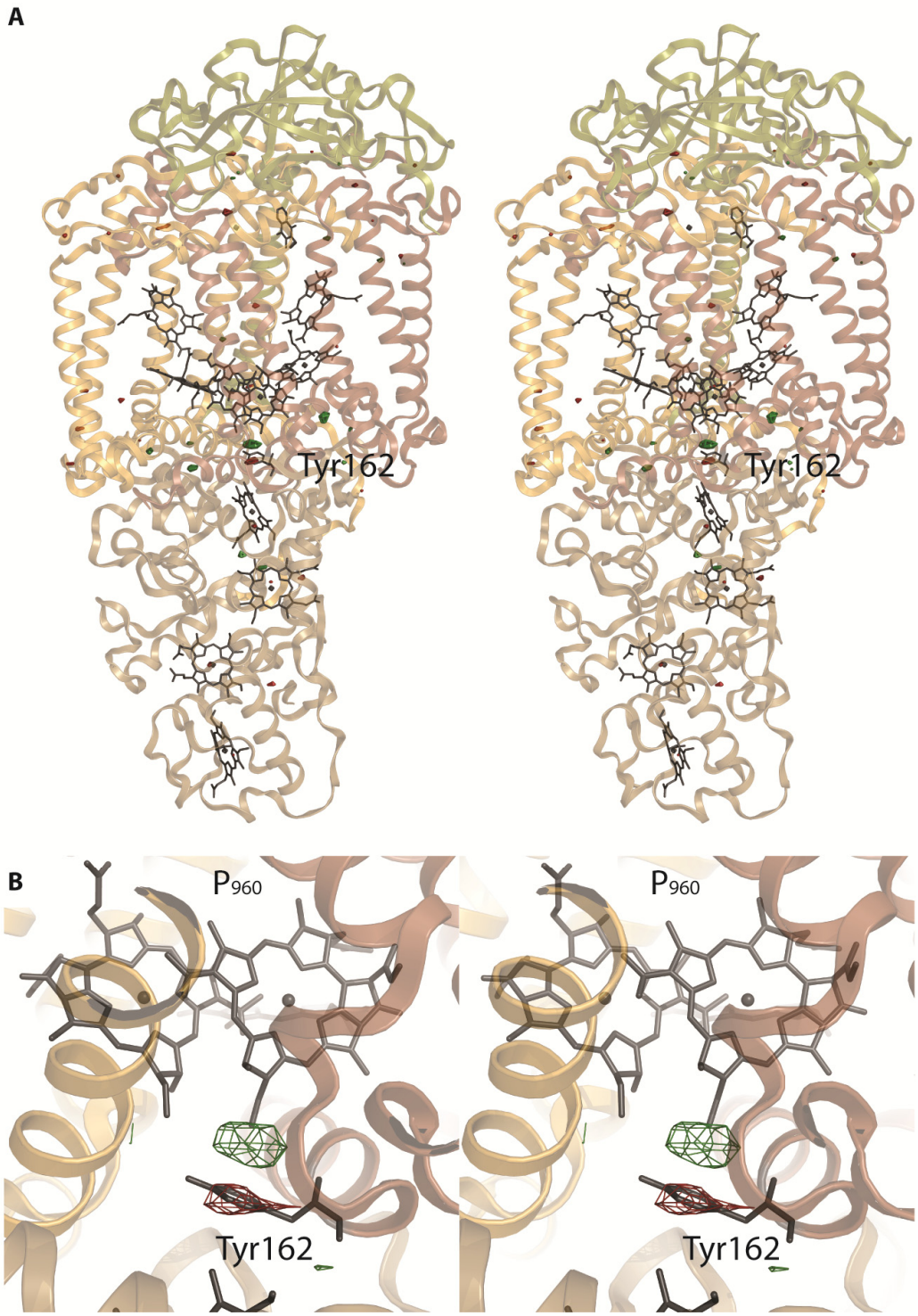

***Figure 18**. A) Long-distance stereo image of F_{light}-F_{dark} difference Fourier electron density map recorded 3 ms after photoactivation (green=positive density, red=negative density, both contoured at 4σ). B). Close- up stereo view of the difference Fourier map close to the TyrL162 residue. Complementary positive and negative electron density are indicative of a movement of TyrL162 towards the special pair during photoactivation.*

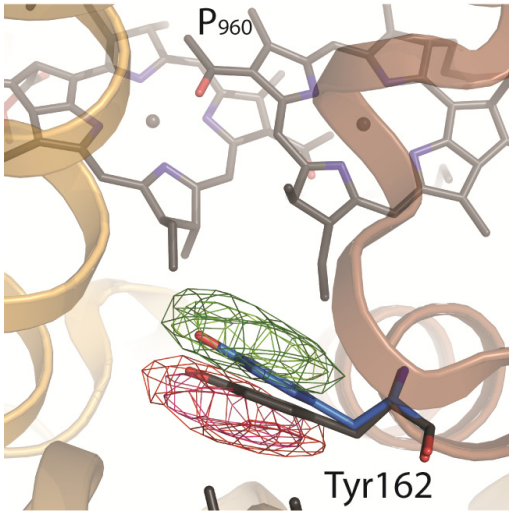

Figure 19. *Theoretical difference density map (F_{light}-F_{dark})$_{theoretical}$ calculated from two refined structural models for the RC_{vir} photoactivated (blue) and ground state (grey), cut to 2.95 Å resolution. Dataset 1 is the pink and light green peaks and the merge datasets the red and green. The size and position of the paired positive and negative electron density peaks agree with the experimental difference Fourier map (compare with Figure 18).*

4.3 Identification and validation of structural changes: movement of TyrL162 towards the special pair upon photoactivation

By examination of the difference density, both the strongest red and green peaks in the map were associated with an amino acid in the L-subunit, Tyrosine 162 (TyrL162). Paired negative and positive density is indicative of conformational changes and thus indicating that TyrL162 orients towards the special pair of bacteriochlorophyll (P_{960}^{+}) upon photoactivation. This tyrosine is strictly conserved among purple bacterial centers [138, 139] and is situated between the special pair and heme 3 (c_{559}) of the cytochrome *c* subunit. The hydroxyl group of the side chain interacts with Water 501, which in turn is coordinated by two other water molecules and the hydroxyl group of SerM188 (Figure 20A).

Structural refinement of the photoactivated state reveals that the hydroxyl oxygen of TyrL162 undergoes a 1.3 Å movement towards the special pair, P_{960}^{+}. This movement also creates new hydrogen bonding interactions with the hydroxyl group of ThrM185 and Water 10 (Figure 20B).

Upon photoexcitation of the special pair, the electrostatic environment changes towards a more positive charge, which implies that TyrL162 is negatively charged in the photoactive state. This seems plausible since it would prove energetically unfavorable to bury the isolated positively charged special pair within the membrane without stabilization of a nearby negatively charged species such as a tyrosyl anion. Furthermore, upon photoactivation, TyrL162 moves towards the special pair, creating new hydrogen bonding interactions with nearby amino acid ThrM185 and water 10 (Wat10), which could act to stabilize the deprotonated TyrL162 (Figure 20B).

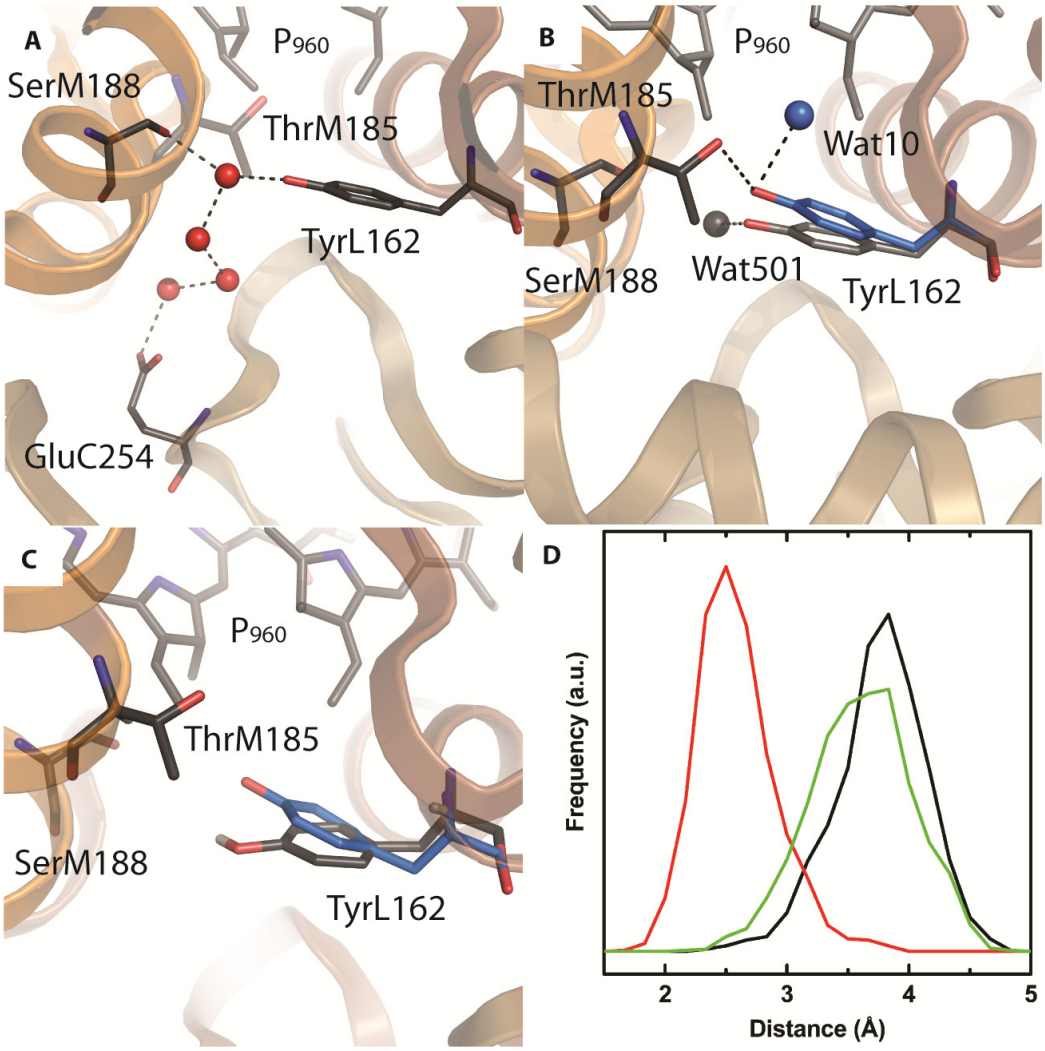

Figure 20. *The modeled light-induced changes in RC_{vir}. A) The ground (resting) state conformation of TyrL162. A chain of water molecules stretching from TyrL162 towards the proteins surface via the SerM188 and GluC254 residues can be seen; B) Refined movement of TyrL162 (blue) overlaid with the ground state conformation (grey). In the photoactivated state, TyrL162 forms H-bond interactions with ThrM185 and Wat10; C) Result of the molecular dynamics (MD) trajectories, showing a reorientation of TyrL162 towards the special pair upon deprotonation (blue); D) Histogram plot of the frequency with which a given minimum distance from the side chain of TyrL162 to the photooxidized special pair when TyrL162 is protonated (green), deprotonated (red) and non-illuminated (black). Histograms were extracted at the final stages of the MD trajectories.*

To investigate the possibility of a deprotonated TyrL162 in the photoactivated state, a series of molecular dynamics (MD) simulations were carried out. These trajectories show that the deprotonated TyrL162 adopts a conformation 1.1 Å closer to the special pair than that of the protonated state (Figure 20C, D). Moreover, to account for the deprotonation step, another MD simulation was carried out to calculate the free energy change (ΔΔG) for transferring the hydroxyl proton from the TyrL162 to the carboxylate of GluC254 upon photoactivation. It was found that the energy requirements for the proton transfer correspond to a (relative) change of 8±1 pK_a units (where K_a is the acid dissociation constant). The reference pK_a values for TyrL162 and GluC254 are 9.8 and 4.3, respectively, which would allow for spontaneous proton transfer to occur. Furthermore, the solvent channel (Figure 20A) would allow for efficient transfer of the proton to the bulk solvent (pH=8.1) and

thus provide a mechanism for coupled electron-proton transfer reactions in photosynthesis. The molecular dynamics calculations were repeated by Ishikita [140] in 2011, concluding that the pK_a of deprotonated TyrL162 was lowered to 6.7 as a result of displacement of its side chain. Furthermore, the deprotonated TyrL162 was found to move towards the ThrM185 in the photoactivated state, which was accompanied by a hydrogen network rearrangement involving the ThrM185 and HisL168 residues.

4.3.1 Analogy with the Tyrosine radical of Photosystem II

It is known that Photosystem II creates a tyrosyl radical (TyrZ•) which oxidizes the manganese cluster and leads to the oxidation of water to oxygen [141, 142]. Structural information about Photosystem II reveals that TyrZ lies between the Manganese center [143] and the special pair in an arrangement which resembles that of TyrL162 of RC_{vir} (Figure 21). Upon photoactivation of the special pair P_{680}, TyrZ is oxidized to a radical by the highly electropositive special pair and this event triggers a proton transfer from TyrZ to D1-His190, leading to extraction of an electron from the manganese cluster [144].

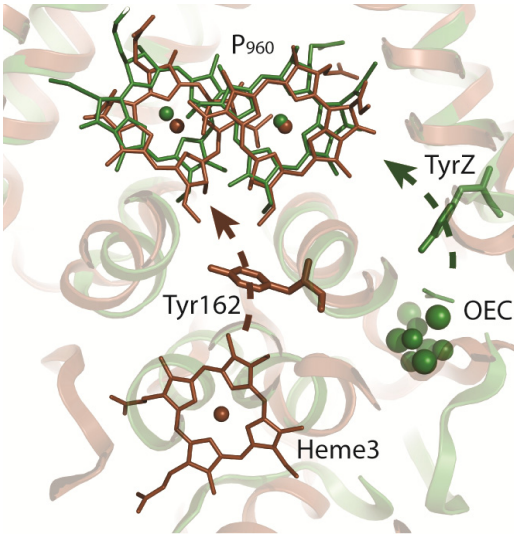

Figure 21. *Overlay of photosystem II (PSII, PDB entry 1S5L, green) and RC_{vir} (brown). TyrZ of PSII and Tyr162 of RC_{vir} are indicated.TyrL162 lies between the special pair and Heme 3, whereas TyrZ lies between the oxygen-evolving center (OEC) and the special pair of PSII.*

Similarly to radical formation in PSII, RC_{sph} mutants which increase the midpoint potential of the special pair [145], have shown that TyrL162 can form a tyrosyl radical (deprotonated) as a result of photoactivation of the special pair. Thus, it can be proposed that conformational switching and especially deprotonation, could be a contributing factor in the evolution of tyrosine radicals in an early form of reaction center.

4.3.2 Summary Paper IV

The robust RC_{vir} crystals grown using lipidic sponge phases were used in a time-resolved Laue experiment in an attempt to study conformational changes in the Q_B binding pocket upon photoactivation. Three datasets were found to be of sufficient quality to yield a difference Fourier electron density map but revealed no changes around the Q_B site. Instead the resulting difference electron density maps showed strong positive and negative electron density associated with a highly conserved Tyrosine residue, TyrL162, situated between the high potential heme 3 (heme c_{559}) and the special pair P_{960}. Structural refinement of the photoactivated state revealed that the hydroxyl oxygen of the TyrL162 undergoes a 1.3 Å movement towards the special pair upon photoactivation.

As a consequence of photoactivation, the special pair becomes positively charged. It would prove energetically unfavorable to bury this positive charge on the special pair within the membrane, implying that TyrL162 is deprotonated upon photoactivation as an act of stabilization of the positive charge on the special pair. This theory was investigated using molecular dynamics simulations which demonstrate that the deprotonated form of TyrL162 adopts a conformation which is 1.1 Å closer to the special pair than that of the protonated form.

In photosystem II, a tyrosyl radical is directly involved in oxidization of a manganese cluster and is found halfway between the special pair and the manganese cluster, functionally similar to that of the position of TyrL162 in the RC_{vir}. We therefore propose that, in an ancient form of the reaction center, the conformational switching of TyrL162 may have contributed to the formation of tyrosine radicals, creating a high enough chemical potential to withdraw electrons from manganese clusters, giving rise to the water-splitting capacity of oxygen evolving centers.

5 X-ray free-electron laser experiments on RC_{vir}: Papers V and VI

The concept of using X-ray free-electron laser radiation to overcome crystallographic problems such as radiation damage and the need for macrocrystals, was proposed by Neutze *et al*. in 2000 [13]. The first hard X-ray free electron laser (XFEL), the Linac Coherent Light Source (LCLS) was commissioned in 2009 and the first structure obtained from a protein was of photosystem I to 8.5 Å in 2011 by Chapman and colleagues [18]. Since then, a number of protein structures have been successfully obtained from the LCLS such as lysozyme [17], photosystem II [21, 22] and the previously undetermined structure of cathepsin B in complex with a native inhibitor, a potential drug target against sleeping sickness [20]. In this chapter, the successful batch microcrystallization in the lipidic sponge phase is presented along with a low resolution structure obtained from only 265 images. Furthermore, the LSP batch crystallization method was used to obtain a 3.5 Å resolution structure of RC_{vir}, which is the highest resolution membrane structure obtained from an XFEL to date.

5.1 Microcrystallization of RC_{vir}

A serial femtosecond crystallography experiment at an XFEL requires large volumes of crystals (up to one milliliter of crystal suspension per day of data collection) and the repetition rate of 60-120 Hz prohibits manual harvesting of crystals. Therefore an alternative method was developed to combine the LSP crystallization method with the batch approach, yielding large amounts of RC_{vir} microcrystals.

5.1.1 Scaling up purification

X-ray free-electron laser experiments using a liquid microjet consume approximately 600 µL of crystal suspension per hour of data collection, which at a protein concentration of 50 mg/mL almost amounts to a gram of protein used in a twelve hour shift at the LCLS. Therefore, the purification protocol was scaled up to accommodate the need for large protein quantities. The anionic exchange column was exchanged for one with a larger diameter which would increase the protein loading volume by a factor of five, followed by a larger size exclusion column (a factor of three). This purification protocol yielded approximately 100 mg of crystallization-grade protein from 50 grams of cells.

5.1.2 Microcrystal growth in the lipidic sponge phase

Obtaining microcrystals is an iterative process. Since LSP crystallization conditions giving macrocrystals were available, these were used as a starting point for microcrystal growth. The first stage of crystallization trials included vapor diffusion sitting drop experiments where the Jeffamine M600 content of the LSP was varied along with the LSP to protein ratio. It was found that small crystals appeared in these conditions, although not sufficiently small for XFEL purposes. The next step was to prepare a batch experiment using glass vials. Here, a total volume of 60 µl per setup was used, consisting of varying ratios of protein, LSP and additives (tri-sodium citrate). These conditions also gave small crystals reminiscent of the ones grown in the first rounds of crystallization and were further refined by omitting all filtration steps for solutions (except for the protein) to provide many nucleation sites for the protein. The size of the batches was also increased to 250 µL in the final conditions,

which were the following: 100 µl reaction center protein at a concentration of 20-30 mg/mL, 100 µL LSP (12 % Monoolein, 17.5 % Jeffamine-M600, 1.0 M Hepes (pH 8.0), 0.7 M $(NH_4)_2SO_4$, 2.5 % 1,2,3- heptanetriol) and 50 µL of the additive 1.0-1.2 M tri-sodium citrate (Figure 23A).

It should be noted that using the batch method alone does not guarantee microcrystals (unpublished observations of another membrane protein), but may instead give macrocrystals suitable for synchrotron diffraction studies. Moreover, optimization of existing crystal conditions to yield microcrystals might influence the diffraction quality, as well as giving rise to other crystal forms. Pre-screening of the microcrystals is usually not possible since the availability of beamtime is extremely limited as only two hard XFEL facilities currently are in commission.

5.1.3 Identification of microcrystals

There are several methods for detection of microcrystals. The most common method is standard light microscopy (Figure 23C) together with a polarizer or a UV-source. If the crystals are sufficiently large (in the micron region), they can be easily identified, especially under polarizing (Figure 23D) or UV light. However, if the crystals are in the lower micron region or even in the nanometer scale, other methods are required for visualization of the crystals.

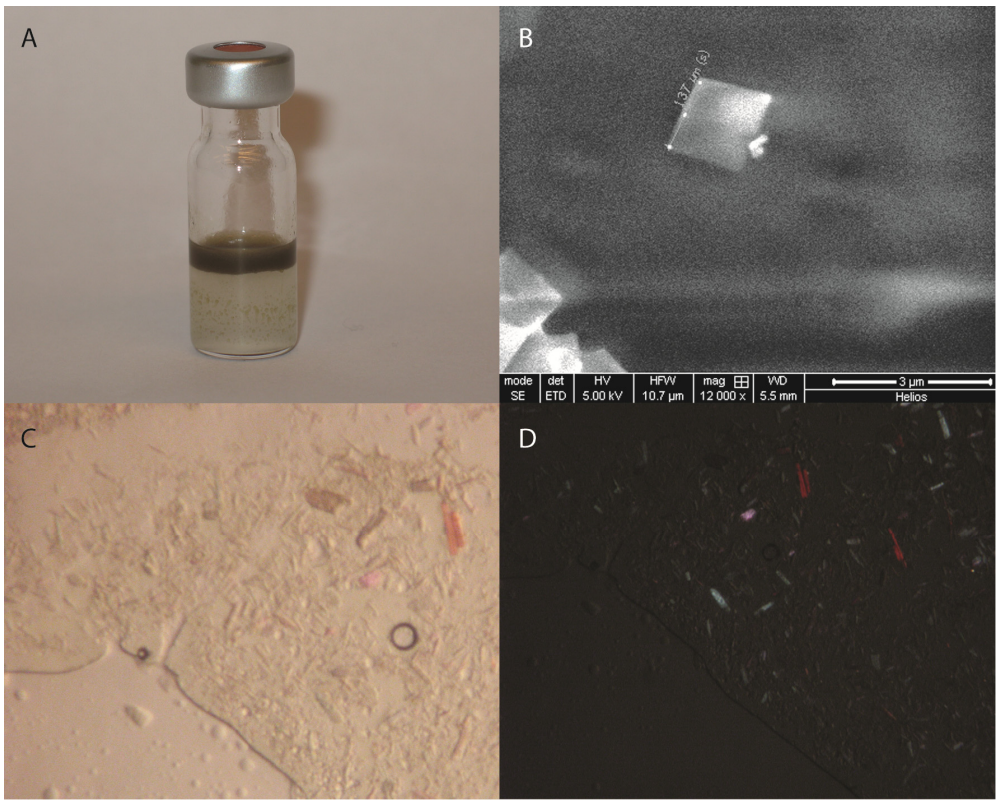

Figure 23. *RC_{vir} microcrystals. A) Glass vial containing RC_{vir} microcrystals (brown); B) SEM image of RC_{vir} microcrystal; C) Microcrystals after filtering through a 10 µm cutoff metal filter; D) The same microcrystals under polarizing light.*

Several detection methods for nano- and microcrystals have been employed such as Scanning Electron Microscopy (SEM, Figure 23B), small-angle X-ray scattering (SAXS)

and Second Order Non-linear Imaging of Chiral Crystals (SONICC) [146]. All these methods have been tested in detection of RC_{vir} crystals, where SAXS and SEM proved successful. In the case of SONICC, incompatibility of the wavelengths used for crystal identification (RC_{vir} absorbs readily within the region used) was proposed to prevent successful detection of these crystals.

5.1.4 Sample delivery system: compatibility with LSP

Both Jeffamine and PEG based LSPs have been successfully used for membrane protein crystallization (summarized in **Papers I-III** and Table 1). While the Jeffamine-based LSPs flow readily in the liquid microjet at a flowrate of 10 µl min^{-1} using a nozzle with an inner diameter of 50 µm, the PEG-based LSPs, which have a higher Monoolein content, require an inner diameter of 100 µm for the microjet to flow. These LSPs consisted of 40 % PEG400, PEG1500 or PEG4000 mixed with 30 % Monoolein and 30 % buffer (0.1 M Hepes, pH 8.0, 0.1 M NaCl and 0.1 M $MgCl_2$). All three PEG-based LSPs were tested for compatibility with the microjet and showed similar behavior (Figure 24).

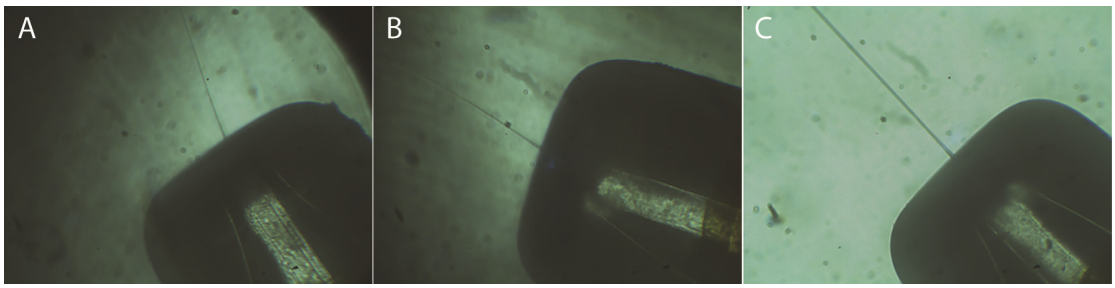

Figure 24. *Microjets formed using PEG-based LSP. A) PEG400 (40 %), Monoolein (30 %) and buffer (30 %); B) PEG1500 (40 %), Monoolein (30 %) and buffer (30 %) and C) PEG4000 (40 %), Monoolein (30 %) and buffer (30 %).*

5.2 Low-resolution structure: a proof-of-principle experiment (Paper V)

A low-resolution dataset was collected at the Atomic, Molecular and Optical Science (AMO) beamline [147] at LCLS in 2010, when the maximum achievable resolution (limited by the experimental geometry) was 7.4 Å. Despite the low resolution and hitrate, it proved to be possible to obtain a molecular replacement solution as well as an electron density map. Furthermore, a new space group and crystal packing were discovered for RC_{vir}.

5.2.1 Data collection

Fully hydrated RC_{vir} microcrystals were injected in a rapidly flowing liquid microjet aligned vertically relative to the X-FEL beam [113]. The crystal-containing LSP flowed at a rate of 10 µl min^{-1} and produced a stable microjet ~4 µm in diameter. Diffraction data were collected at the AMO [147] beamline of the LCLS on the Center for Free-Electron Laser Science Advanced Study Group multipurpose chamber (CAMP) pn-junction charge-coupled devices (pnCCDs) [148] with two panels that were read out at the same repetition rate as the XFEL (60 Hz). The photon energy of the X-ray pulses were 2 keV (6.17 Å wavelength) with up to 10^{12} photons per pulse (at the sample position) and pulse duration of 70 fs, focused in a 10 μm^2 spot. A diffraction image is shown in Figure 25A.

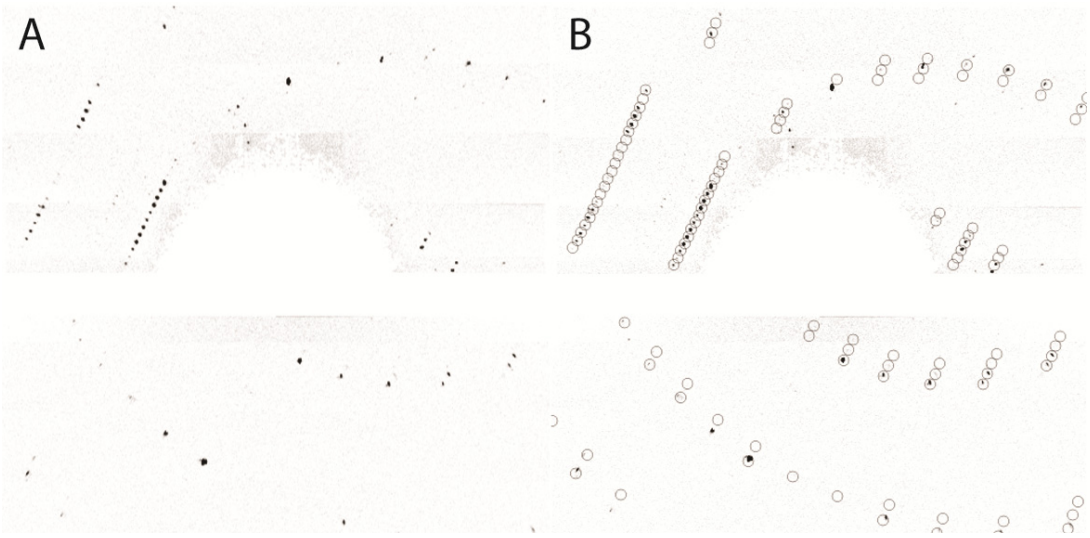

Figure 25. *A) A diffraction image of an RC_{vir} microcrystal collected on two detector panels at the Atomic, Molecular and Optical Science (AMO) beamline at the Linac Coherent Light Source. B) The corresponding indexed diffraction image. The maximum resolution with the energy and detector geometry at the experiment in 2010 was 7.4 Å.*

5.2.2 SFX data processing: new RC_{vir} space group discovered

In total, 365,035 images were recorded during approximately 100 minutes of beamtime, of which 1,542 were denoted diffraction patterns by the hit-finding software developed by Anton Barty (http://www.desy.de/~barty/cheetah/). The diffraction patterns were then fed into the CrystFEL [106] software that called DirAx [107] and MOSFLM [108] for automated indexing. The indexing was initially performed using the cell parameters from the previously determined LSP structure (2WJN, **Paper III**), but the predicted peak locations did not agree with the peaks on the diffraction pattern. Therefore, the CrystFEL software was used to perform *ab initio* indexing without a previously known space group and cell parameters. After several iterations, the cell parameters converged to the following: axes a=57.6 Å, b=84.6 Å, c=375.8 Å and α=β=γ=90°, using a total of 265 diffraction images which were indexed in the novel space group $P2_12_12_1$.

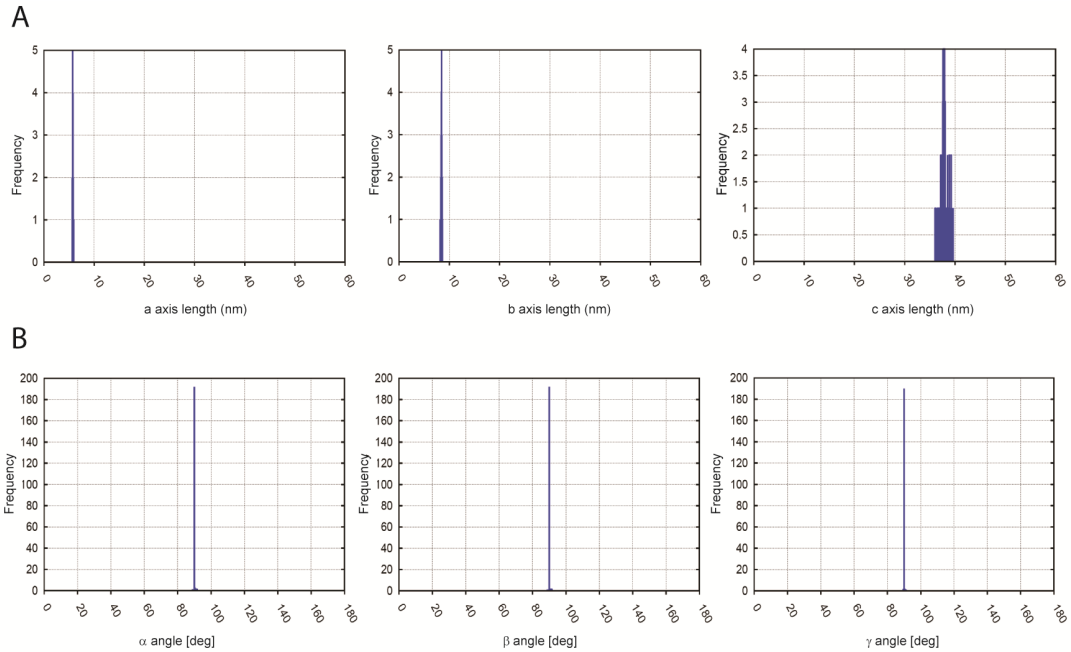

Figure 26. *Histograms of A) cell axes and B) cell angles, recovered from 265 RC_{vir} diffraction images.*

No subpopulations of other crystal forms were observed in the cell parameter histogram (Figure 26). Small variations in the length of the c axis can be seen in the histogram which might be the result of pulse-to-pulse fluctuations in the XFEL wavelength as well as non-isomorphism of the LSP crystals.

The diffraction data were processed using Monte Carlo methods because each diffraction pattern recorded only partial reflections from randomly oriented microcrystals. The I/σ values for each resolution bin were estimated from reflections with positive intensity and a multiplicity higher than 1. The NZ-test and L-test plots showed the expected distributions of a non-twinned space group as expected for the $P2_12_12_1$ space group (not shown).

5.2.3 Molecular replacement and refinement

The phases were solved by molecular replacement using Phaser 2.3.0 [149] with PDB entry 2WJN (**Paper III**) as the search model. The best solution had a translation function Z score (TFZ) = 8.5, a rotation function Z score (RFZ) = 5.8 and a log likelihood gain (LLG) = 81. This was well discriminated from second best solution with scores of TFZ = 4.6; RFZ = 5.8; and LLG = 39. A TF Z score of at least 8 and LLG of 40 are required for a definite solution in Phaser.

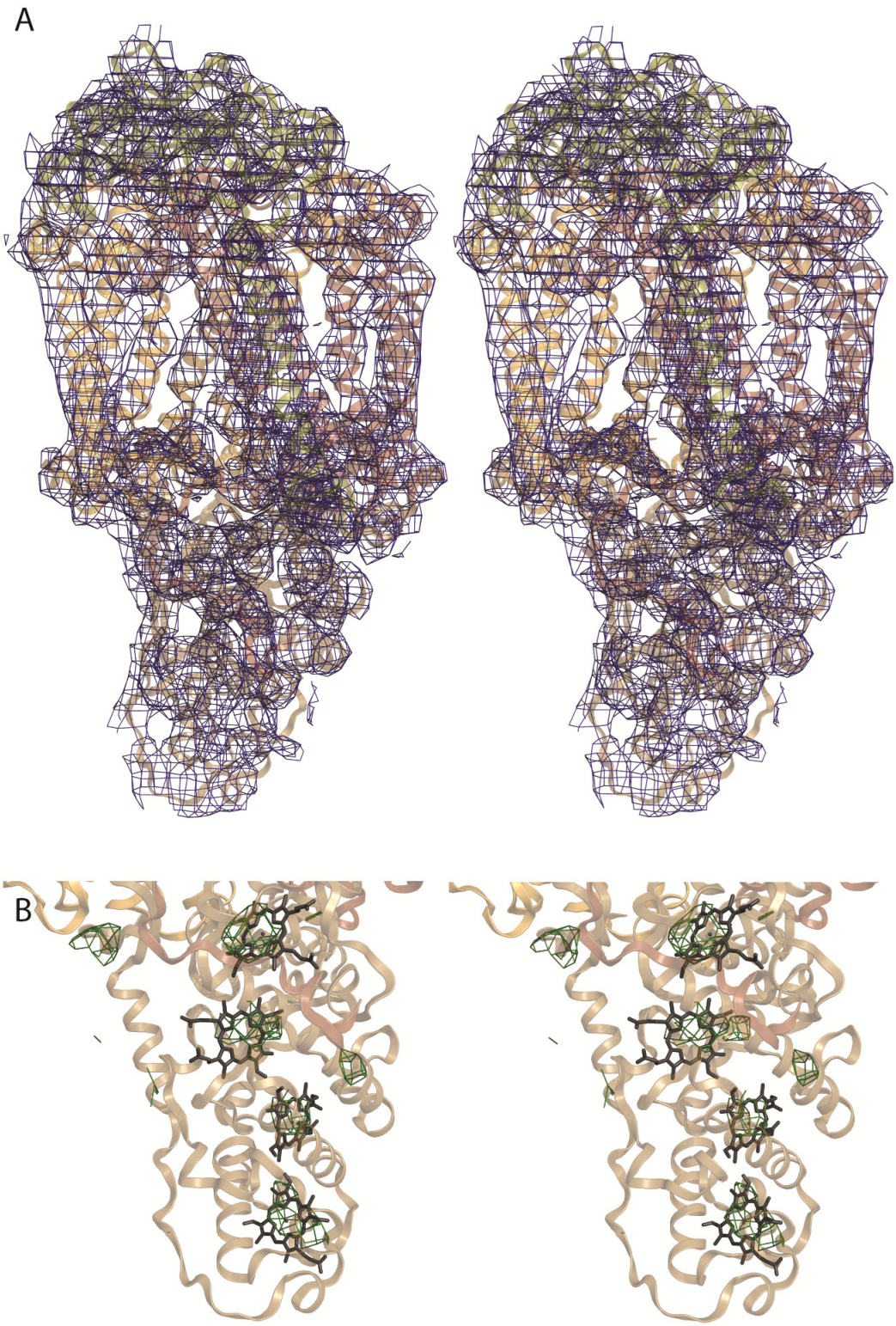

***Figure 27**. A) Electron density for the LSP serial femtosecond crystallography RC_{vir} structure at 8.2 Å resolution shown in stereo. A) $2F_{obs}$-F_{calc} density contoured at 1 σ recovered from 265 diffraction images; B) Stereo view of the omit electron density map (contoured at 2σ), calculated with all four heme groups omitted.*

Refinement was performed using 20 cycles of rigid body and restrained refinement using REFMAC5 [99], converging to R_{factor}/R_{free} = 0.35/0.38 and an overall figure of merit of 0.62. During refinement a simple Wilson scaling was used and a constant

X-ray data and refinement statistics	
Total number of images	365,035
Images showing diffraction	1542
Images indexed	265
Wavelength	6.17 Å
Data processing resolution limits	46.1 - 7.4 Å
Number of used reflections	2247
Completeness	85%
Multiplicity	8.0
Rint	50%
I/σ	1.9
Refinement resolution limits	46.1 - 8.2 Å
Rfactor	35%
R_{free} (5% omitted reflections)	38%
Overall figure of merit	0.62

Table 5. *Summary of X-ray data and refinement statistics for the data collected at the AMO beamline at LCLS.* R_{int} *is defined as* $R_{int} = \Sigma_{hkl} |F_{even}-F_{odd}|/\Sigma_{hkl} ((F_{even}+F_{odd})/2)$

density (using default values) was assigned to the region of the unit cell which was not occupied by protein atoms. The solvent mask was calculated using default parameters. The diffraction data were cut to 8.2 Å resolution, where the multiplicity was greater than four and completeness was above 85%. The crystallographic data statistics are summarized in Table 5.

5.2.4 Control map calculations

Since the data were cut at 8.2 Å and few details are visible at this resolution, a number of control map calculations were performed on the SFX data and also for monochromatic and Laue data for comparison. Additional control calculations were performed to confirm the molecular replacement solution. This was done using two control datasets: one with the h, k, l indices of processed SFX data randomly shuffled and one where all intensities were uniform. Molecular replacement failed with both of these control datasets. Instead the phases from the molecular replacement solution recovered against the experimental data were combined with these control datasets. The resulting electron density maps did not show any α-helical structure and hence it can be concluded that random or uniform data do not produce electron density maps containing any structural information and therefore the molecular replacement solution obtained using the experimental data were not due purely to model bias.

An omit map was also calculated, where all four heme groups of the cytochrome *c* subunit were removed. Positive F_{obs} - F_{calc} electron density associated with each of the heme co-factors were detected in the resulting omit map (Figure 27B). As a final validation control, a composite omit electron density map was calculated using the program CNS [102, 150] version 1.3. The same calculations were performed with monochromatic data (using PDB entry 2WJN, **Paper III**), as well as room-temperature Laue data (PDB entry 2X5U, **Paper IV**) cut at 8.2 Å, which both showed comparable electron density map quality as the SFX data (Figure 28).

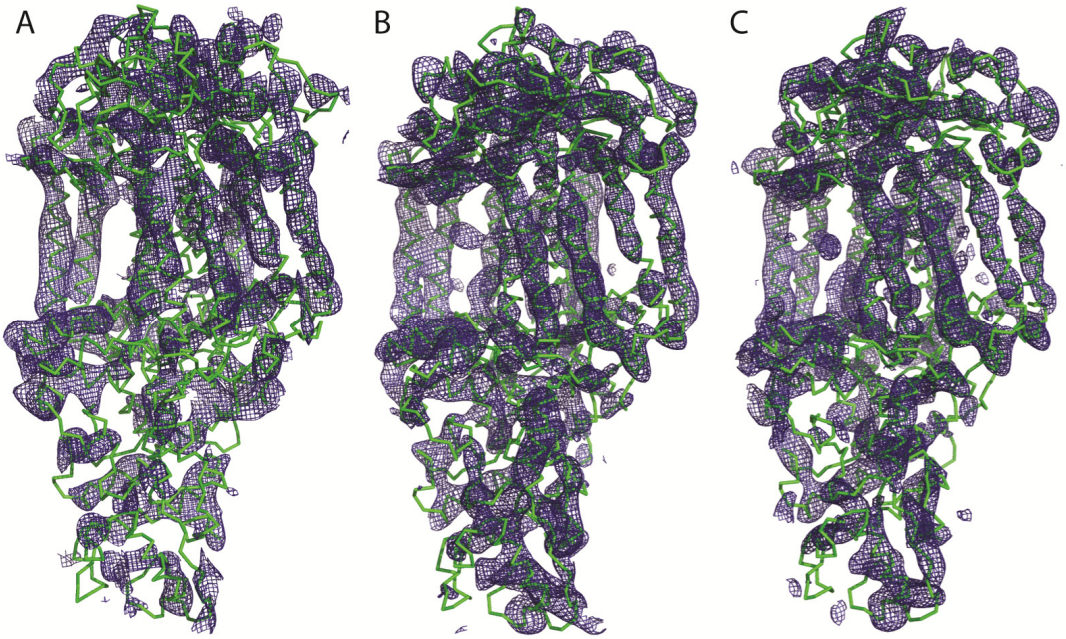

Figure 28. *Composite omit electron density maps calculated using CNS 1.3 with 5 % of the model omitted in each step. A) Calculated using the LCLS data; B) Calculated from data extracted from PDB entry 2WJN (Paper II) and C) Calculated from data extracted from PDB entry 2X5U (Paper IV). All data are cut to 8.2 Å resolution and contoured at 1.5σ.*

5.2.5 Summary Paper V

In **Paper V**, the first ever protein structure from an XFEL with a novel space group was presented. The structure of the photosynthetic reaction center from *Blastochloris viridis* was solved to 8.2 Å resolution from only 265 images collected from lipidic-sponge phase batch-grown crystals. Since a novel space group was found in this type of experiment, it is not unlikely that this crystallization proceeds v*ia* a different route than that of the corresponding vapor diffusion experiment. Furthermore, we confirmed that a number of different lipidic sponge phases based on both Jeffamine M600 and PEGs could be successfully injected using a liquid microjet. This may enable more challenging protein targets to be solved using X-ray free electron lasers such as ion channels and GPCRs, which are known to crystallize in PEG-based lipidic cubic phases (Table 1).

Data were collected at the LCLS in June 2010, when the wavelength of the AMO beamline station was limited to 6.17 Å [147] and the experimental setup was limited to 7.4 Å resolution. The reaction center structure was processed to 8.2 Å and structural refinement yielded crystallographic R and R_{free} values of 35 % and 38 %, respectively. Both the $2F_{obs}$-F_{calc} electron density map and composite omit map clearly indicated transmembrane α helices despite the low resolution of 8.2 Å. Moreover, upon removal of all four heme groups of the RC_{vir} cytochrome *c* subunit from the structural model, positive F_{obs}-F_{calc} electron density associated with each of these co-factors were observed in the resulting omit map confirming that little model bias is present.

5.3 High-resolution XFEL experiment on RC_{vir}: Paper VI

In 2011, a new beamline was commissioned at the LCLS, the Coherent X-ray Imaging beamline (CXI) [151]. This enabled crystallographic data collection at 120 Hz using energies up to 11 keV and a 1.3 x 1.3 μm^2 (FWHM) beam spot size [14, 151]. This allows for high-resolution RC_{vir} data to be collected and one such experiment was conducted in 2011.

5.3.1 Data collection

Microcrystals were directly injected into the LCLS beam (9 keV, focal spot of 10 μm^2, 0.6 mJ/pulse) at the CXI beamline [151] in 2011 using a microjet. These data were recorded on a Cornell-SLAC Pixel Array Detector (CSPAD) [19] consisting of an array of 64 independently controlled panels of 192 x 185 pixels each, forming a 1516 x 1516 pixel array (arranged in 1702 x 1702 pixels with small gaps allowing for the beam to go through). The sample-to-detector distance was 142 mm in the experiment, corresponding to 2.62 Å resolution at the edge of the detector. Crystals occasionally diffracted to a maximum of 2.8 Å resolution (Figure 29) and in total 2,744,614 images were recorded during approximately five hours of data collection.

5.3.2 Data processing

Peak detection and local background correction were performed using the Cheetah software package, where water scattering and coherent scattering from the microjet were removed from the images. Images containing more than ten Bragg peaks were classified as hits and were passed to the CrystFEL [106] software suite for processing. MOSFLM [108] and DirAx [107] were used for processing by the Indexamajig program of the CrystFEL suite. Furthermore, high tolerances were used to account for the c -axis variability which was also seen in the low-resolution data.

Scaling and merging was performed using process_hkl (part of the CrystFEL software suite [106]), where the data were merged according to the Monte Carlo method [152]. Data collection statistics and quality measures such as R_{split} were calculated by splitting the dataset in half and comparing the two halves relative to each other using the check_hkl and compare_hkl scripts of CrystFEL. The data collection statistics are summarized in Table 6.

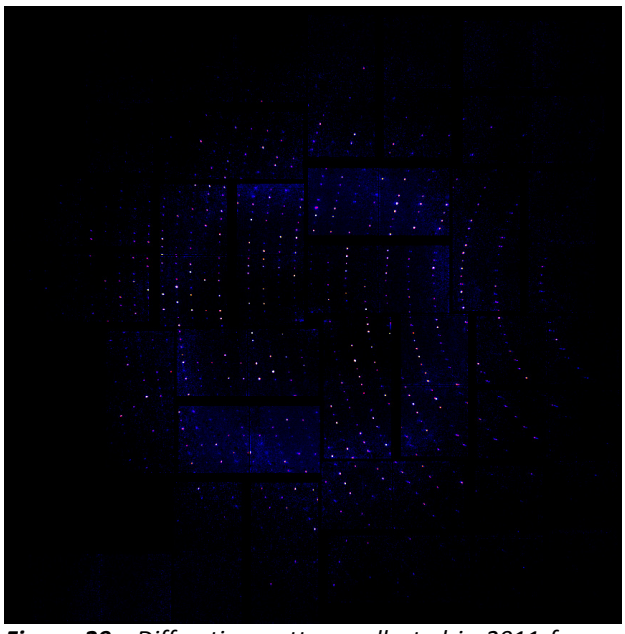

Figure 29. *Diffraction pattern collected in 2011 from a single microcrystal of reaction center showing diffraction to about 2.8 Å. Detector distance 142 mm.*

5.3.3 Refinement strategies

Molecular replacement was used to obtain the phases using PhaserMR 2.5.2. [149] with coordinates from the high-resolution cryo-temperature structure as a search model (PDB entry 2WJN, **Paper III**). A log likelihood gain (LLG) = 2,879, Rotation function score (RFZ) = 28.6 and Translation Function Score (TFZ) = 32.8 were recovered. The structure was refined using rigid body refinement and jelly body refinement in REFMAC5 [99] in combination with manual rebuilding in COOT [98]. TLS [114] was also successfully used in conjunction with the jelly body refinement during refinement improving the R_{free} by about 1 %. The R and R_{free} values converged to 29.4 % and 32.7 % respectively, with an overall figure of merit of 0.78. The structure was validated using MOLPROBITY [153] and PROCHECK [154]. Refinement statistics are summarized in Table 6.

Data collection	**Native RCvir (2011)**
Energy (keV)	9.34
Total number of images (hits)	88,924
Indexed images	1,175
Data processing resolution limits (Å)	58.00-1.49
Total number of reflections	335,664
Number of used reflections (Free)	17,024 (1,175)
Completeness (%)	99.0 (93.42)
Multiplicity	27.02 (27.6)
Overall R_{split}[§] on I	36.53 (52.73)
Mean I/σ(I)	3.50 (2.0)
Space group	$P2_12_12_1$
Unit cell parameters	a=58.0 Å; b= 84.8 Å; c=382.7 Å α=β=λ=90°
Refinement resolution limits	30- 3.50 Å
R_{work} (%)	29.4
R_{free} (5% omitted reflections), (%)	32.7
Overall figure of merit (%)	78
Number of atoms in model	10,048
Protein residues	1,191
rms (bonds, Å)	0.0096
rms (angles, °)	1.97
Ramachandran favoured (%)	97.0
Ramachandran allowed (%)	3.00
Ramachandran outliers (%)	0
Clash score (all atoms)	6.48
Average B factor[§]	22.4

[§] *R_{split} defined as $R_{split} = 2^{-1/2}\Sigma_{hkl} |I_{even}-I_{odd}|/(½2\Sigma_{hkl} (I_{even}+I_{odd}))$. Values in parenthesis indicate statistics for the highest resolution shell.*

Table 6. *Summary of data collection and refinement statistics for the 2011 and 2012 data.*

5.3.4 Control map calculations

Control maps were calculated where all metal atoms were omitted (iron and magnesium) from the model. This resulted in positive F_{obs} - F_{calc} omit electron density at a contour level of 3σ associated with each of the heme co-factors (the omit map obtained for heme 4 is shown in Figure 30B) as well as for the magnesium atoms associated with the special pair (Figure 30A).

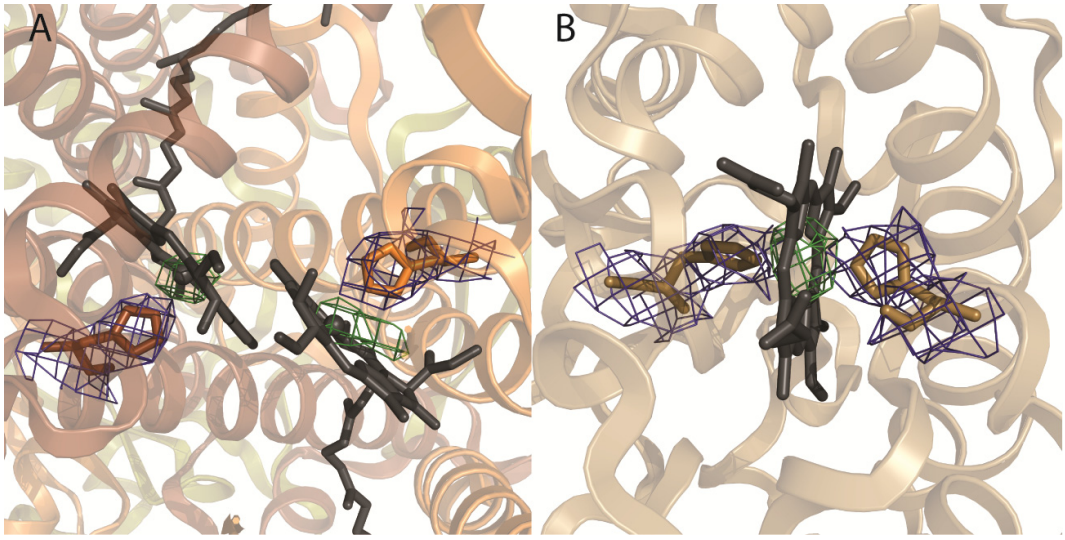

***Figure 30**. Electron density map for metal-containing co-factors. A) F_{obs}-F_{calc} electron density contoured at 1.5σ calculated with the two Mg atoms removed from the special pair; B) F_{obs}-F_{calc} electron density contoured at 3σ calculated with the Fe atom removed from heme 4. The $2F_{obs}$-F_{calc} electron density around the protein ligands is also shown (contoured at 1σ).*

5.4 The structure of RC_{vir} to 3.5 Å resolution

The data collected in 2011 was cut at 3.5 Å where the I/σ was 2.0 and the completeness 93.4 % when using 1,175 indexed images. The quality of the resulting electron density map is excellent as even the bacteriochlorophyll tail of the special pair is clearly visible in the density (Figure 31). Density is also visible for all lipids found in the structures presented in **Paper III**. Upon investigation of the Q_B binding pocket a Monoolein molecule was again found to be bound instead of the native ubiquinone-9 (not shown).

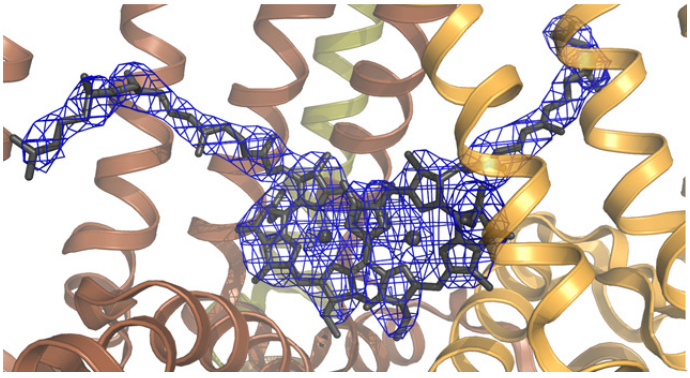

***Figure 31.** A $2F_{obs}$-F_{calc} electron density map of the special pair of RC_{vir} at 3.5 Å resolution obtained from 1,175 diffraction images. The electron density map was contoured at 1σ.*

5.4.1 Comparison with the Laue room temperature ground state structure

Calculation of internal distance matrix changes [155] provides a method of comparing different structures without the need for superposition. This approach was used to compare this SFX structure to all other RC_{vir} structures deposited in the PDB. This revealed that the LSP-grown microcrystal RC_{vir} structure is closest to the room-temperature Laue diffraction structure (PDB entry 2X5U, **Paper IV**). The average internal distance matrix change in this case on the Cα atoms is 0.27 Å, which is similar to the value of the difference between the Laue structure compared to all

other cryo-cooled RC_{vir} structures. The internal distance matrix reveals that there is a large change in the C-subunit, while the changes in the transmembrane regions are relatively minor. When overlaying the 2X5U structure with the one from this SFX experiment, a slight twist of the C-subunit is observed and movements of up to 1.9 Å occur at the edges of the C-subunits. The Cα atom differences within the membrane region are less than 0.5 Å. Since the C-subunit is involved in crystal contacts, it must be concluded that these differences arise from the packing and not from any systematic differences between SFX and Laue data collection.

5.4.2 SFX and radiation damage

The use of SFX to overcome radiation damage in crystals was briefly discussed in section 2.5.3. A single microcrystal in this experiment was exposed to an X-ray fluence of about 4×10^{11} 9 keV photons (in a 10 μm^2 spot focus), which corresponds to a dose of 33 MGy at the sample position. This dose is similar to what cryogenically cooled crystals are exposed to and about two orders of magnitude above that useful for room temperature data collection [156]. This dose of 33 MGy causes about four primary photo-ionization events per RC_{vir} molecule in the microcrystal, which in turn lead to about 200 secondary ionization events [157]. This amounts to approximately 800 ionization events per RC_{vir} molecule and ultimately causes the destruction of the microcrystal within a few hundred femtoseconds. However, upon inspection of the F_{obs}-F_{calc} electron density for the co-factors calculated with all iron and magnesium atoms omitted from the model, the electron density surrounding the metal centers is surprisingly well-ordered and there is no indication of radiation damage (Figure 30).

5.4.3 Summary Paper VI

In **Paper VI** we demonstrated that the concept of the lipidic sponge phase (LSP) batch microcrystallization can be used to obtain crystals diffracting to high resolution. We found that the LSP-grown RC_{vir} crystals occasionally diffracted to about 2.8 Å and a complete dataset could be processed to 3.5 Å resolution using 1,175 images obtained from five hours of data collection at the CXI beamline commissioned at the LCLS in 2011. This structure is currently the highest resolution membrane structure obtained to date using the SFX method

An internal distance matrix was calculated between the RC_{vir} SFX structure at 3.5 Å resolution and the Laue diffraction ground state structure (2.95 Å resolution) which revealed a shift in the C- subunit relative to the other subunits in the SFX data. Movements of up to 1.9 Å of the Cα atoms could be seen at the edges of the C- subunit and are proposed to be a result of the crystal contacts of the SFX crystal form rather than differences between the Laue and SFX data collection approaches.

The impact of damage on the RC_{vir} microcrystals was also investigated. A number of electron density maps were calculated with the metal centers omitted from the model. The resulting F_{obs}-F_{calc} electron density maps showed surprisingly well-ordered positive electron density without any visible radiation damage around the metal atoms of the co-factors.

6 Future perspectives

This thesis contributes to structural and functional understanding of the membrane protein reaction center from the purple bacterium *Blastochloris viridis* (RC_{vir}). The structure was studied using both conventional synchrotron radiation, as well as a newly commissioned free-electron laser source and its electron transport was studied using time-resolved Laue diffraction. Furthermore, a lipid sponge phase membrane protein crystallization screen was developed in an effort to facilitate crystallization of difficult membrane protein targets.

Lipidic sponge phases

Since **Papers I** and **II** were published, several interesting structures have been crystallized in lipidic phases (mainly the lipidic cubic phase, LCP), including pharmaceutically relevant GPCRs, ion channels and transporters (summarized in Table 1). The crystallization conditions are strikingly similar to many of those included in the screen; particularly PEG400 which has been successfully used for the majority of structures obtained from the LCP. Many eukaryotic proteins, including human, require addition of cholesterol in the LCP for additional stabilization during crystallization. This is a feature which could easily be incorporated into the existing screen, extending it to a 96 well format. Additionally, miniaturization of the screen would allow for high-throughput using a robot, which would make the screen more user friendly and could potentially increase the rate of successful crystallization events.

Time-resolved Laue crystallography

The time-resolved Laue method has successfully been used in conjunction with the LSP-grown crystals and movement of a highly conserved Tyrosine residue (TyrL162) in response to photoactivation could be detected. However, data were only collected at one time-point (3 ms) and the movement of TyrL62 should be further investigated at other time-points to determine its role in electron transfer in the bacterial reaction center.

Moreover, another goal of the experiment presented in **Paper IV** was to study the movement of ubiquinone in the Q_B binding pocket in response to light-activation. This was not possible due to the low ubiquinone occupancy of the Q_B site, where a Monoolein molecule was bound instead. The high lipid content of the crystallization matrix is a major limiting factor and thus increases the difficulty of ubiquinone incorporation. One possibility would be to deplete the protein of ubiquinone and instead use a synthetic ubiquinone with a shorter tail which more readily would fit into the binding pocket and which is added throughout the whole purification process.

Serial Femtosecond Crystallography

An X-ray free electron laser (XFEL) such as the Linac Coherent Light Source (LCLS) allows time-resolved data to be collected with previously unachievable temporal resolution and atomic resolution structures to be determined from nanosized protein crystals. The method of Serial Femtosecond Crystallography (SFX) for solving

novel protein structures has already shown enormous potential. Structures have been solved for a number of soluble proteins, of which one is a novel complex structure of an enzyme with its native inhibitor bound [20] and several membrane protein structures, including those presented in this thesis (**Papers V** and **VI**). Moreover, several beamlines at the LCLS are equipped with femtosecond lasers, allowing for time-resolved data collection on both reversible, but also irreversible systems, made possible by the continuous replenishment of sample by using a microjet.

Despite these recent successes, many challenges remain. In particular, the sample volumes necessary for high-resolution data collection amount to several grams per beamtimes and this is usually not feasible for most membrane proteins. Therefore the injection systems need to be further developed to decrease the sample consumption, decrease clogging and minimize settling events. Improvements in data processing will detect more “hits” and new methods of determining experimental errors in the data will emerge. The LSP-batch microcrystallization can be extended to other systems, including targets crystallized in the closely-related lipidic cubic phase (LCP), providing a more liquid environment which facilitates the delivery of crystals. Other microcrystal evaluation tools such as SONICC need to be further developed and extended to the highly successful LSP and LCP crystallization methods. Moreover, improvements in data processing will likely contribute to an increase in the indexing rates and improved handling of noise.

In conclusion, the potential of an XFEL in conjunction with membrane protein crystallography will be further exploited with the commissioning of new XFELs around the world such as SACLA in Japan, SwissFEL in Switzerland and the European XFEL in Germany. These advances in membrane structural biology will undoubtedly revolutionize our understanding of the interplay between the structure and function of proteins.

7 Acknowledgements

Time flies when you're having fun (or being busy rather…). I've learnt more things than I could ever imagine throughout these past five years. It's been great to get to know all of you, both current and former members on this floor and I want to say a special thank you to the following people:

Richard, my supervisor a.k.a. "the boss". You can be very demanding at times (I know your phone numbers by heart, all of them ☺); but you are also a truly inspiring person and I really appreciate the scientific freedom you give us here in the lab. And thank you for all the opportunities of travelling around the world, it's been a true privilege and I'm very grateful for the opportunity!

Gergely, my co-supervisor. You are a true genius! Thanks for always replying to my endless questions about crystallography (and about programming and about other random things). And good luck with the THz!

Martin, thank you for being my examiner and for answering all my questions about the defence! And thank you **Örjan** for chairing the defence.

Annemarie, thank you for having me as your diploma worker! Not only did you teach me how to prep RC, you also introduced me to beer club (and to the art of "working late")!

Sven Engström, "the LSP guru": thanks for introducing me to the world of lipids and teaching me the art of SAXS measurements, especially the day before xmas☺.

Jan Davidsson, thank you for all laser-related synchrotron trips! Your knowledge has been essential more time than I can recall! **Moreno, Alexande**r: good luck with your future research!

The old "Neutze" group: **Magnus**- I'm sorry I stole your position as the beer king! **Pontus, Maria, Fredrik, Gerhard and Urszula,** while we've never really worked together, it's been a pleasure having you around and thanks for countless BC nights! And thanks Gerhard for the trip to Canada and for that bottle of Pernod…

Cecilia, Jennie, Rob. Cecilia: you're a real asset to this group. Keep up the good work! Jennie, I'm sure you will have a great time with UbOx. At least eventually ☺ Rob, it's been fun getting to know you and thanks for all late nights! I'm sure there will be more of those soon…

Erik, thanks for being a great drummer in The Hidden. I'm still laughing when I think about it! And thanks for all beam times and all late nights in the lab!

David, I wasn't very convinced about the new ginger male at first, but you have become a true friend! Thanks for sharing coffee breaks, harddrive space and pretty

much everything with me. You're welcome to come and hang out with the goats anytime, I promise ☺

Mikael, it was fun getting to know you "back in the day" in the "exjobb" room. I'm still looking forward to seeing you in those shoes (you know what I mean…!)

Weixiao, it's been great to have some to discuss with about lipids! **Ida, Annette, Sebastian, Mike, Peter, Etienne, Kristina, Rhawnie, Elin, Rosie, Susanna:** you make up the core of this corridor. Keep up the good work!

Alex: I will miss your labels ☺ **Petra:** lycka till både i och utanför "rinken"! Jag lovar att komma förbi och titta på er snart!

Madde, tack för alla tips om disputation och avhandling och tack för en grym fest! **Karin "kakan"**: snart blir det frukost på sängen igen, jag lovar!

Linnea och Johan tack för alla roliga AW:s och BC:ar!

Maria och Anna: det var kul att undervisa Biokemi 2 med er (även om jag är glad att vi slipper det i fortsättningen). **Joakim och Anders**: lycka till i "källaren"!

My "exjobb" students: **Anna, Petra** and **Ruth**. Thank you for your endless patience with COX/UbOx! You have really done a lot and I'm very impressed with all of you!

All new people in the lab: **Amit, Gisela, Rajiv, Kiran, Maria**, **Susmita, Stephan, Sebastian, Gupta, Oskar**: welcome to floor 2! I'm sure you will enjoy your time here as much as I have!

Lars & Bruno, tack för att ni fixar med datorer och allt annat som är trasigt! Vad skulle vi egentligen göra utan er?

Till alla mina **vänner**, jag lovar att jag snart ska komma och hälsa på er igen! Tack för att ni alltid finns där för mig! Puss!

Min familj: alltid växande (i antal, inte på bredden), tack för att ni inte klagar alltför mycket när jag inte kan fira olika högtider med er. Snart ses vi igen!

Farmor och farfar: hade jag inte ofrivilligt startat den där bananflugefarmen vet man aldrig vad det hade blivit av mig… Och tack för att ni alltid finns där för mig!

Mattias, tack för all din uppmuntran och allt ditt stöd. Men framförallt tack för att du har stått ut med mig under dessa fem år. Snart är det min tur att återgälda allt! Jag älskar dig!

8 Appendix:

8.1 Conditions of the lipidic sponge phase screen (Paper II)

Vial No.	Solvent 1	Solvent 2	Lipid	Buffer	pH	Salt 1	Salt 2
1	PEG 400	-	MO	MES	5.5	-	-
2	PEG 400	-	MO	MES	5.5	NaCl	$MgCl_2$
3	PEG 1500	-	MO	MES	5.5	-	-
4	PEG 1500	-	MO	MES	5.5	NaCl	Li_2SO_4
5	PEG 4000	-	MO	MES	5.5	NaCl	Li_2SO_4
6	PEG 400	-	MO	MES	6.0	-	-
7	PEG 400	-	MO	MES	6.0	NaCl	Li_2SO_4
8	PEG 1500	-	MO	MES	6.0	-	-
9	PEG 1500	-	MO	MES	6.0	NaCl	$MgCl_2$
10	PEG 4000	-	MO	MES	6.0	NaCl	$MgCl_2$
11	PEG 4000	-	MO	MES	6.0	NaCl	Li_2SO_4
12	PEG 400	-	MO	MES	6.5	NaCl	$MgCl_2$
13	PEG 400	-	MO	MES	6.5	NaCl	Li_2SO_4
14	PEG 1500	-	MO	MES	6.5	-	-
15	PEG 1500	-	MO	MES	6.5	NaCl	$MgCl_2$
16	PEG 4000	-	MO	MES	6.5	-	-
17	PEG 4000	-	MO	MES	6.5	NaCl	Li_2SO_4
18	PEG 400	-	MO	HEPES	7.0	-	-
19	PEG 400	-	MO	Tris	7.0	-	-
20	PEG 1500	-	MO	Tris	7.0	-	-
21	PEG 4000	-	MO	HEPES	7.0	-	-
22	Jeffamine M600	1,2,3-heptanetriol	MO	HEPES	7.0	NH_4SO_4	-
23	Jeffamine M600	1,2,3-heptanetriol	MO	HEPES	7.0	NH_4SO_4	-
24	Jeffamine M600	1,2,3-heptanetriol	MO	HEPES	7.0	NH_4SO_4	-
25	PEG 400	-	MO	HEPES	7.5	-	-
26	PEG 400	-	MO	HEPES	7.5	NaCl	$MgCl_2$
27	PEG 1500	-	MO	HEPES	7.5	-	-
28	PEG 1500	-	MO	HEPES	7.5	NaCl	Li_2SO_4
29	PEG 4000	-	MO	Tris	7.5	-	-
30	PEG 4000	-	MO	Tris	7.5	NaCl	$MgCl_2$
31	Jeffamine M600	1,2,3-heptanetriol	MO	HEPES	7.5	NH_4SO_4	-
32	PEG 400	-	MO	HEPES	8.0	-	-
33	PEG 400	-	MO	HEPES	8.0	NaCl	Li_2SO_4
34	PEG 4000	-	MO	Tris	8.0	NaCl	$MgCl_2$
35	Jeffamine M600	1,2,3-heptanetriol	MO	HEPES	8.0	NH_4SO_4	-
36	Jeffamine M600	1,2,3-heptanetriol	MO	HEPES	8.0	NH_4SO_4	-
37	Jeffamine M600	1,2,3-heptanetriol	MO	HEPES	8.0	NH_4SO_4	-
38	PEG 400	-	MO	HEPES	8.5	-	-
39	PEG 400	-	MO	Tris	8.5	NaCl	$MgCl_2$
40	PEG 1500	-	MO	Tris	8.5	NaCl	$MgCl_2$
41	PEG 4000	-	MO	Tris	8.5	-	-
42	Jeffamine M600	1,2,3-heptanetriol	MO	HEPES	8.5	NH_4SO_4	-
43	Jeffamine M600	1,2,3-heptanetriol	MO	HEPES	8.5	NH_4SO_4	-
44	PEG 400	-	MO	Tris	9.0	-	-
45	PEG 400	-	MO	Tris	9.0	NaCl	$MgCl_2$
46	PEG 1500	-	MO	Tris	9.0	-	-
47	PEG 1500	-	MO	Tris	9.0	NaCl	$MgCl_2$
48	PEG 4000	-	MO	Tris	9.0	NaCl	Li_2SO_4

8.2 Table of reproducible peaks (Paper IV)

Table of the reproducible peaks recovered from the top 100 strongest positive and negative peaks in the three difference Fourier F_{obs}-F_{obs} maps (using 3.5 Å search radius).

	Difference map	Peak rank*	Rank product†	Peak height (σ)	Average (σ)
Positive cluster 1	1	1		5.43	
(TyrL162)	2	23	46	3.69	4.52
	3	2		4.43	
Positive cluster 2	1	14		4.12	
(ArgL135, ProL136)	2	70	81340	3.45	3.69
	3	83		3.49	
Negative cluster 1	1	1		-4.70	
(TyrL162)	2	32	512	-3.92	-4.29
	3	16		-4.25	
Negative cluster 2	1	35		-3.89	
Accessory chlorophyll	2	37	22015	-3.87	-4.00
L-branch	3	17		-4.24	
Negative cluster 3	1	54		-3.80	
ValM166	2	66	167508	-3.66	-3.79
	3	47		-3.90	

*The position this peak is observed at when sorted according to maximum σ value

†The product of the three Peak rank values.

8.3 Free energy calculations of the proton transfer from TyrL162 to GluC254 (Paper IV)

Free energy of proton transfer from TyrL162 to GluC254 in four different states of the reaction center and in water.

	ΔG (kJ/mol) run 1	ΔG (kJ/mol) run 2	ΔG (kJ/mol) run 3	$\langle \Delta G \rangle$
C_{559}(II),P_{960}^{0}	21.1 ± 2.9	23.1 ± 2.2	27.0 ± 2.0	24 ± 3
C_{559}(II),P_{960}^{+}	-20.0 ± 2.2	-24.9 ± 2.3	-24.8 ± 3.5	-23 ± 5
C_{559}(III),P_{960}^{0}	-4.9 ± 3.5	-1.8 ± 2.3	-9.8 ± 3.2	-6 ± 2
C_{559}(III),P_{960}^{+}	-48.1 ± 2.0	-52.3 ± 2.2	-54.2 ± 2.1	-52 ± 2
Water	-50.4 ± 0.5	-48.8 ± 1.0	-52.3 ± 1.5	-51 ± 1

The roman numerals between parentheses indicate the oxidation state of the hemes in the cytochrome c subunit.

9 References

1. von Heijne, G., *The membrane protein universe: what's out there and why bother?* Journal of Internal Medicine, 2007. **261**(6): p. 543-557.
2. Krogh, A., et al., *Predicting transmembrane protein topology with a hidden Markov model: Application to complete genomes.* Journal of Molecular Biology, 2001. **305**(3): p. 567-580.
3. Drews, J., *Drug discovery: A historical perspective.* Science, 2000. **287**(5460): p. 1960-1964.
4. Muller, D.J., N. Wu, and K. Palczewski, *Vertebrate membrane proteins: Structure, function, and insights from biophysical approaches.* Pharmacological Reviews, 2008. **60**(1): p. 43-78.
5. Deisenhofer, J., et al., *X-ray structure analysis of a membrane protein complex. Electron density map at 3 A resolution and a model of the chromophores of the photosynthetic reaction center from Rhodopseudomonas viridis.* J Mol Biol, 1984. **180**(2): p. 385-98.
6. Raman, P., V. Cherezov, and M. Caffrey, *The Membrane Protein Data Bank.* Cell Mol Life Sci, 2006. **63**(1): p. 36-51.
7. Garman, E.F. and T.R. Schneider, *Macromolecular cryocrystallography.* Journal of Applied Crystallography, 1997. **30**: p. 211-237.
8. Aishima, J., et al., *High-speed crystal detection and characterization using a fast-readout detector.* Acta Crystallogr D Biol Crystallogr, 2010. **66**(Pt 9): p. 1032-5.
9. Hendrickson, W.A., *Determination of Macromolecular Structures from Anomalous Diffraction of Synchrotron Radiation.* Science, 1991. **254**(5028): p. 51-58.
10. Baxter, R.H.G., et al., *Time-resolved crystallographic studies of light-induced structural changes in the photosynthetic reaction center.* Proceedings of the National Academy of Sciences of the United States of America, 2004. **101**(16): p. 5982-5987.
11. Owen, R.L., E. Rudino-Pinera, and E.F. Garman, *Experimental determination of the radiation dose limit for cryocooled protein crystals.* Proceedings of the National Academy of Sciences of the United States of America, 2006. **103**(13): p. 4912-4917.
12. Solem, J.C., *Imaging Biological Specimens with High-Intensity Soft X-Rays.* Journal of the Optical Society of America B-Optical Physics, 1986. **3**(11): p. 1551-1565.
13. Neutze, R., et al., *Potential for biomolecular imaging with femtosecond X-ray pulses.* Nature, 2000. **406**(6797): p. 752-757.
14. Emma, P., et al., *First lasing and operation of an angstrom-wavelength free-electron laser.* Nature Photonics, 2010. **4**(9): p. 641-647.
15. McNeil, B.W.J. and N.R. Thompson, *X-ray free-electron lasers.* Nature Photonics, 2010. **4**(12): p. 814-821.
16. Barty, A., et al., *Self-terminating diffraction gates femtosecond X-ray nanocrystallography measurements.* Nature Photonics, 2012. **6**(1): p. 35-40.
17. Boutet, S., et al., *High-Resolution Protein Structure Determination by Serial Femtosecond Crystallography.* Science, 2012. **337**(6092): p. 362-364.
18. Chapman, H.N., et al., *Femtosecond X-ray protein nanocrystallography.* Nature, 2011. **470**(7332): p. 73-U81.
19. Hart, P., et al., *The CSPAD megapixel x-ray camera at LCLS.* X-Ray Free-Electron Lasers: Beam Diagnostics, Beamline Instrumentation, and Applications, 2012. **8504**.
20. Redecke, L., et al., *Natively Inhibited Trypanosoma brucei Cathepsin B Structure Determined by Using an X-ray Laser.* Science, 2013. **339**(6116): p. 227-230.
21. Kern, J., et al., *Room temperature femtosecond X-ray diffraction of photosystem II microcrystals.* Proc Natl Acad Sci U S A, 2012. **109**(25): p. 9721-6.
22. Kern, J., et al., *Simultaneous Femtosecond X-ray Spectroscopy and Diffraction of Photosystem II at Room Temperature.* Science, 2013.
23. Krauss, N., *Mechanisms for photosystems I and II.* Curr Opin Chem Biol, 2003. **7**(5): p. 540-50.
24. Xiong, J., et al., *Molecular evidence for the early evolution of photosynthesis.* Science, 2000. **289**(5485): p. 1724-1730.
25. Xiong, J. and C.E. Bauer, *Complex evolution of photosynthesis.* Annual Review of Plant Biology, 2002. **53**: p. 503-521.
26. Xiong, J. and C.E. Bauer, *A cytochrome b origin of photosynthetic reaction centers: an evolutionary link between respiration and photosynthesis.* Journal of Molecular Biology, 2002. **322**(5): p. 1025-1037.
27. Price, D.C., et al., *Cyanophora paradoxa Genome Elucidates Origin of Photosynthesis in Algae and Plants.* Science, 2012. **335**(6070): p. 843-847.
28. Nelson, N. and A. Ben-Shem, *The complex architecture of oxygenic photosynthesis.* Nature Reviews Molecular Cell Biology, 2004. **5**(12): p. 971-982.
29. Drews, G. and R.A. Niederman, *Membrane biogenesis in anoxygenic photosynthetic prokaryotes.* Photosynthesis Research, 2002. **73**(1-3): p. 87-94.
30. Deisenhofer, J. and H. Michel, *The Photosynthetic Reaction Center from the Purple Bacterium Rhodopseudomonas-Viridis.* Embo Journal, 1989. **8**(8): p. 2149-2170.
31. Yano, J., et al., *Where water is oxidized to dioxygen: Structure of the photosynthetic Mn4Ca cluster.* Science, 2006. **314**(5800): p. 821-825.
32. Hillier, W. and G.T. Babcock, *Photosynthetic reaction centers.* Plant Physiology, 2001. **125**(1): p. 33-37.
33. Chitnis, P.R., *Photosystem I: Function and physiology.* Annual Review of Plant Physiology and Plant Molecular Biology, 2001. **52**: p. 593-626.
34. Jordan, P., et al., *Three-dimensional structure of cyanobacterial photosystem I at 2.5 A resolution.* Nature, 2001. **411**(6840): p. 909-17.
35. Buttner, M., et al., *Photosynthetic Reaction Center Genes in Green Sulfur Bacteria and in Photosystem-1 Are Related.* Proceedings of the National Academy of Sciences of the United States of America, 1992. **89**(17): p. 8135-8139.

36. Deisenhofer, J., et al., *Structure of the protein subunits in the photosynthetic reaction centre of Rhodopseudomonas viridis at 3A resolution.* Nature, 1985. **318**(6047): p. 618-24.
37. Feniouk, B.A., et al., *Coupling of proton flow to ATP synthesis in Rhodobacter capsulatus: F0F1-ATP synthase is absent from about half of chromatophores.* Biochimica Et Biophysica Acta-Bioenergetics, 2001. **1506**(3): p. 189-203.
38. Drews, G. and P. Giesbrecht, *[Rhodopseudomonas viridis, n. sp., a newly isolated, obligate phototrophic bacterium].* Arch Mikrobiol, 1966. **53**(3): p. 255-62.
39. Miller, K.R. and J.S. Jacob, *The Rhodopseudomonas-Viridis Photosynthetic Membrane - Arrangement Insitu.* Archives of Microbiology, 1985. **142**(4): p. 333-339.
40. Lang, F.S. and D. Oesterhelt, *Microaerophilic growth and induction of the photosynthetic reaction center in Rhodopseudomonas viridis.* J Bacteriol, 1989. **171**(5): p. 2827-34.
41. Edebo, L., *A New Press for the Disruption of Micro-Organisms and Other Cells.* Journal of Biochemical and Microbiological Technology and Engineering, 1960. **2**(4): p. 453-479.
42. Alderton, G., W.H. Ward, and H.L. Fevold, *Isolation of Lysozyme from Egg White.* Journal of Biological Chemistry, 1945. **157**(1): p. 43-58.
43. Alderton, G., J.C. Lewis, and H.L. Fevold, *The Relationship of Lysozyme, Biotin and Avidin.* Science, 1945. **101**(2615): p. 151-152.
44. Berman, H.M., et al., *The Protein Data Bank.* Nucleic Acids Res, 2000. **28**(1): p. 235-42.
45. Ganem-Quintanar, A., D. Quintanar-Guerrero, and P. Buri, *Monoolein: A review of the pharmaceutical applications.* Drug Development and Industrial Pharmacy, 2000. **26**(8): p. 809-820.
46. Caffrey, M., *A lipid's eye view of membrane protein crystallization in mesophases.* Current Opinion in Structural Biology, 2000. **10**(4): p. 486-497.
47. Landau, E.M. and J.P. Rosenbusch, *Lipidic cubic phases: a novel concept for the crystallization of membrane proteins.* Proc Natl Acad Sci U S A, 1996. **93**(25): p. 14532-5.
48. Katona, G., et al., *Lipidic cubic phase crystal structure of the photosynthetic reaction centre from Rhodobacter sphaeroides at 2.35 angstrom resolution.* Journal of Molecular Biology, 2003. **331**(3): p. 681-692.
49. Pebay-Peyroula, E., et al., *X-ray structure of bacteriorhodopsin at 2.5 angstroms from microcrystals grown in lipidic cubic phases.* Science, 1997. **277**(5332): p. 1676-81.
50. Vogeley, L., et al., *Anabaena sensory rhodopsin: a photochromic color sensor at 2.0 A.* Science, 2004. **306**(5700): p. 1390-3.
51. Royant, A., et al., *X-ray structure of sensory rhodopsin II at 2.1-angstrom resolution.* Proceedings of the National Academy of Sciences of the United States of America, 2001. **98**(18): p. 10131-10136.
52. Gordeliy, V.I., et al., *Molecular basis of transmembrane signalling by sensory rhodopsin II-transducer complex.* Nature, 2002. **419**(6906): p. 484-487.
53. Kolbe, M., et al., *Structure of the light-driven chloride pump halorhodopsin at 1.8 A resolution.* Science, 2000. **288**(5470): p. 1390-6.
54. Kato, H.E., et al., *Crystal structure of the channelrhodopsin light-gated cation channel.* Nature, 2012. **482**(7385): p. 369-U115.
55. Tiefenbrunn, T., et al., *High Resolution Structure of the ba3 Cytochrome c Oxidase from Thermus thermophilus in a Lipidic Environment.* Plos One, 2011. **6**(7).
56. Lyons, J.A., et al., *Structural insights into electron transfer in caa(3)-type cytochrome oxidase.* Nature, 2012. **487**(7408): p. 514-U137.
57. Cherezov, V., et al., *High-resolution crystal structure of an engineered human beta(2)-adrenergic G protein-coupled receptor.* Science, 2007. **318**(5854): p. 1258-1265.
58. Chien, E.Y.T., et al., *Structure of the Human Dopamine D3 Receptor in Complex with a D2/D3 Selective Antagonist.* Science, 2010. **330**(6007): p. 1091-1095.
59. Jaakola, V.P., et al., *The 2.6 Angstrom Crystal Structure of a Human A(2A) Adenosine Receptor Bound to an Antagonist.* Science, 2008. **322**(5905): p. 1211-1217.
60. Shimamura, T., et al., *Structure of the human histamine H-1 receptor complex with doxepin.* Nature, 2011. **475**(7354): p. 65-U82.
61. Wu, B.L., et al., *Structures of the CXCR4 Chemokine GPCR with Small-Molecule and Cyclic Peptide Antagonists.* Science, 2010. **330**(6007): p. 1066-1071.
62. Haga, K., et al., *Structure of the human M2 muscarinic acetylcholine receptor bound to an antagonist.* Nature, 2012. **482**(7386): p. 547-U147.
63. Kruse, A.C., et al., *Structure and dynamics of the M3 muscarinic acetylcholine receptor.* Nature, 2012. **482**(7386): p. 552-556.
64. Manglik, A., et al., *Crystal structure of the mu-opioid receptor bound to a morphinan antagonist.* Nature, 2012. **485**(7398): p. 321-U170.
65. Wu, H.X., et al., *Structure of the human kappa-opioid receptor in complex with JDTic.* Nature, 2012. **485**(7398): p. 327-U69.
66. Thompson, A.A., et al., *Structure of the nociceptin/orphanin FQ receptor in complex with a peptide mimetic.* Nature, 2012. **485**(7398): p. 395-U150.
67. White, J.F., et al., *Structure of the agonist-bound neurotensin receptor.* Nature, 2012. **490**(7421): p. 508-+.
68. Granier, S., et al., *Structure of the delta-opioid receptor bound to naltrindole.* Nature, 2012. **485**(7398): p. 400-U171.
69. Zhang, C., et al., *High-resolution crystal structure of human protease-activated receptor 1.* Nature, 2012. **492**(7429): p. 387-+.
70. Hanson, M.A., et al., *Crystal Structure of a Lipid G Protein-Coupled Receptor.* Science, 2012. **335**(6070): p. 851-855.
71. Cherezov, V., et al., *In meso crystal structure and docking simulations suggest an alternative proteoglycan binding site in the OpcA outer membrane adhesin.* Proteins, 2008. **71**(1): p. 24-34.
72. Fairman, J.W., et al., *Crystal Structures of the Outer Membrane Domain of Intimin and Invasin from Enterohemorrhagic E. coil and Enteropathogenic Y. pseudotuberculosis.* Structure, 2012. **20**(7): p. 1233-1243.

73. Efremov, R.G. and L.A. Sazanov, *Structure of Escherichia coli OmpF porin from lipidic mesophase.* Journal of Structural Biology, 2012. **178**(3): p. 311-318.
74. Liao, J., et al., *Structural Insight into the Ion-Exchange Mechanism of the Sodium/Calcium Exchanger.* Science, 2012. **335**(6069): p. 686-690.
75. Cherezov, V., H. Fersi, and M. Caffrey, *Crystallization screens: Compatibility with the lipidic cubic phase for in meso crystallization of membrane proteins.* Biophysical Journal, 2001. **81**(1): p. 225-242.
76. Cherezov, V., et al., *Room to move: crystallizing membrane proteins in swollen lipidic mesophases.* J Mol Biol, 2006. **357**(5): p. 1605-18.
77. Caffrey, M., *On the Mechanism of Membrane Protein Crystallization in Lipidic Mesophases.* Crystal Growth & Design, 2008. **8**(12): p. 4244-4254.
78. Cherezov, V., et al., *A robotic system for crystallizing membrane and soluble proteins in lipidic mesophases.* Acta Crystallographica Section D-Biological Crystallography, 2004. **60**: p. 1795-1807.
79. Cherezov, V. and M. Caffrey, *Picolitre-scale crystallization of membrane proteins.* Journal of Applied Crystallography, 2006. **39**: p. 604-606.
80. Cherezov, V. and M. Caffrey, *Membrane protein crystallization in lipidic mesophases. A mechanism study using X-ray microdiffraction.* Faraday Discussions, 2007. **136**: p. 195-212.
81. Engstrom, S., et al., *Solvent-induced sponge (L-3) phases in the solvent-monoolein-water system.* Colloid Science of Lipids, 1998. **108**: p. 93-98.
82. Qiu, H. and M. Caffrey, *The phase diagram of the monoolein/water system: metastability and equilibrium aspects.* Biomaterials, 2000. **21**(3): p. 223-234.
83. Engstrom, S., P. Wadsten-Hindrichsen, and B. Hernius, *Cubic, sponge, and lamellar phases in the glyceryl monooleyl ether-propylene glycol-water system.* Langmuir, 2007. **23**(20): p. 10020-10025.
84. Nollert, P. and E.M. Landau, *Enzymic release of crystals from lipidic cubic phases.* Biochemical Society Transactions, 1998. **26**(4): p. 709-713.
85. Wadsten, P., et al., *Lipidic sponge phase crystallization of membrane proteins.* Journal of Molecular Biology, 2006. **364**(1): p. 44-53.
86. Cherezov, V., et al., *In meso structure of the cobalamin transporter, BtuB, at 1.95 A resolution.* J Mol Biol, 2006. **364**(4): p. 716-34.
87. Wohri, A.B., et al., *Lipidic Sponge Phase Crystal Structure of a Photosynthetic Reaction Center Reveals Lipids on the Protein Surface.* Biochemistry, 2009. **48**(41): p. 9831-9838.
88. Faham, S. and J.U. Bowie, *Bicelle crystallization A new method for crystallizing membrane proteins yields a monomeric bacteriorhodopsin structure.* Journal of Molecular Biology, 2002. **316**(1): p. 1-6.
89. Luecke, H., et al., *Crystallographic structure of xanthorhodopsin, the light-driven proton pump with a dual chromophore.* Proceedings of the National Academy of Sciences of the United States of America, 2008. **105**(43): p. 16561-16565.
90. Ujwal, R. and J.U. Bowie, *Crystallizing membrane proteins using lipidic bicelles.* Methods, 2011. **55**(4): p. 337-41.
91. Ujwal, R., et al., *The crystal structure of mouse VDAC1 at 2.3 A resolution reveals mechanistic insights into metabolite gating.* Proc Natl Acad Sci U S A, 2008. **105**(46): p. 17742-7.
92. Luecke, H., et al., *Crystallographic structure of xanthorhodopsin, the light-driven proton pump with a dual chromophore.* Proc Natl Acad Sci U S A, 2008. **105**(43): p. 16561-5.
93. Wang, H., J. Elferich, and E. Gouaux, *Structures of LeuT in bicelles define conformation and substrate binding in a membrane-like context.* Nat Struct Mol Biol, 2012. **19**(2): p. 212-9.
94. Vinothkumar, K.R., *Structure of rhomboid protease in a lipid environment.* J Mol Biol, 2011. **407**(2): p. 232-47.
95. Rasmussen, S.G., et al., *Crystal structure of the human beta2 adrenergic G-protein-coupled receptor.* Nature, 2007. **450**(7168): p. 383-7.
96. Giacovazzo, C., M. Ladisa, and D. Siliqi, *The approach of the joint probability distribution functions: the SIR-MIR, SAD-MAD and SIRAS-MIRAS, cases.* Zeitschrift Fur Kristallographie, 2002. **217**(12): p. 703-709.
97. Deacon, A.M., et al., *The Shake-and-Bake structure determination of triclinic lysozyme.* Proceedings of the National Academy of Sciences of the United States of America, 1998. **95**(16): p. 9284-9289.
98. Emsley, P., et al., *Features and development of Coot.* Acta Crystallographica Section D-Biological Crystallography, 2010. **66**: p. 486-501.
99. Vagin, A.A., et al., *REFMAC5 dictionary: organization of prior chemical knowledge and guidelines for its use.* Acta Crystallogr D Biol Crystallogr, 2004. **60**(Pt 12 Pt 1): p. 2184-95.
100. Adams, P.D., et al., *PHENIX: a comprehensive Python-based system for macromolecular structure solution.* Acta Crystallogr D Biol Crystallogr, 2010. **66**(Pt 2): p. 213-21.
101. Brunger, A.T., *Free R value: a novel statistical quantity for assessing the accuracy of crystal structures.* Nature, 1992. **355**(6359): p. 472-5.
102. Brunger, A.T., et al., *Crystallography & NMR system: A new software suite for macromolecular structure determination.* Acta Crystallographica Section D-Biological Crystallography, 1998. **54**: p. 905-921.
103. Henderso.R and J.K. Moffat, *Difference Fourier Technique in Protein Crystallography - Errors and Their Treatment.* Acta Crystallographica Section B-Structural Crystallography and Crystal Chemistry, 1971. **B 27**(Jul15): p. 1414-&.
104. Terwilliger, T.C. and J. Berendzen, *Correlated phasing of multiple isomorphous replacement data.* Acta Crystallographica Section D-Biological Crystallography, 1996. **52**: p. 749-757.
105. Terwilliger, T.C. and J. Berendzen, *Difference Refinement - Obtaining Differences between 2 Related Structures.* Acta Crystallographica Section D-Biological Crystallography, 1995. **51**: p. 609-618.
106. White, T.A., et al., *CrystFEL: a software suite for snapshot serial crystallography.* Journal of Applied Crystallography, 2012. **45**: p. 335-341.
107. Duisenberg, A.J.M., *Indexing in Single-Crystal Diffractometry with an Obstinate List of Reflections.* Journal of Applied Crystallography, 1992. **25**: p. 92-96.

108. Leslie, A.G.W. and H.R. Powell, *Processing diffraction data with MOSFLM.* Evolving Methods for Macromolecular Crystallography, 2007. **245**: p. 41-51.
109. Kirian, R.A., et al., *Femtosecond protein nanocrystallography-data analysis methods.* Opt Express, 2010. **18**(6): p. 5713-23.
110. Garman, E., *'Cool' crystals: macromolecular cryocrystallography and radiation damage.* Current Opinion in Structural Biology, 2003. **13**(5): p. 545-551.
111. Murphy, M.L., et al., *The Effect of Coronary-Artery Bypass-Surgery on the Incidence of Myocardial-Infarction and Hospitalization.* Progress in Cardiovascular Diseases, 1986. **28**(4): p. 309-317.
112. Cammarata, M., et al., *Chopper system for time resolved experiments with synchrotron radiation.* Review of Scientific Instruments, 2009. **80**(1).
113. DePonte, D.P., et al., *Gas dynamic virtual nozzle for generation of microscopic droplet streams.* Journal of Physics D-Applied Physics, 2008. **41**(19).
114. Winn, M.D., M.N. Isupov, and G.N. Murshudov, *Use of TLS parameters to model anisotropic displacements in macromolecular refinement.* Acta Crystallographica Section D-Biological Crystallography, 2001. **57**: p. 122-133.
115. Lancaster, C.R.D. and H. Michel, *The coupling of light-induced electron transfer and proton uptake as derived from crystal structures of reaction centres from Rhodopseudomonas viridis modified at the binding site of the secondary quinone, Q(B).* Structure, 1997. **5**(10): p. 1339-1359.
116. Barclay, E., M. O'Reilly, and G. Milligan, *Activation of an alpha(2A)-adrenoceptor-G alpha(o1), fusion protein dynamically regulates the palmitoylation status of the G protein but not of the receptor.* Biochemical Journal, 2005. **385**: p. 197-206.
117. Katona, G., et al., *Lipidic cubic phase crystal structure of the photosynthetic reaction centre from Rhodobacter sphaeroides at 2.35A resolution.* J Mol Biol, 2003. **331**(3): p. 681-92.
118. Koepke, J., et al., *pH modulates the quinone position in the photosynthetic reaction center from Rhodobacter sphaeroides in the neutral and charge separated states.* Journal of Molecular Biology, 2007. **371**(2): p. 396-409.
119. Camara-Artigas, A., D. Brune, and J.P. Allen, *Interactions between lipids and bacterial reaction centers determined by protein crystallography.* Proceedings of the National Academy of Sciences of the United States of America, 2002. **99**(17): p. 11055-11060.
120. McAuley, K.E., et al., *Structural details of an interaction between cardiolipin and an integral membrane protein.* Proceedings of the National Academy of Sciences of the United States of America, 1999. **96**(26): p. 14706-14711.
121. Fyfe, P.K., et al., *Disruption of a specific molecular interaction with a bound lipid affects the thermal stability of the purple bacterial reaction centre.* Biochimica Et Biophysica Acta-Bioenergetics, 2004. **1608**(1): p. 11-22.
122. Deisenhofer, J., et al., *Crystallographic Refinement at 2.3-Angstrom Resolution and Refined Model of the Photosynthetic Reaction-Center from Rhodopseudomonas-Viridis.* Journal of Molecular Biology, 1995. **246**(3): p. 429-457.
123. Baxter, R.H.G., et al., *Cryogenic structure of the photosynthetic reaction center of Blastochloris viridis in the light and dark.* Acta Crystallographica Section D-Biological Crystallography, 2005. **61**: p. 605-612.
124. Schotte, F., et al., *Watching a protein as it functions with 150-ps time-resolved X-ray crystallography.* Science, 2003. **300**(5627): p. 1944-1947.
125. Srajer, V., et al., *Photolysis of the carbon monoxide complex of myoglobin: Nanosecond time-resolved crystallography.* Science, 1996. **274**(5293): p. 1726-1729.
126. Srajer, V., et al., *Protein conformational relaxation and ligand migration in myoglobin: A nanosecond to millisecond molecular movie from time-resolved Laue X-ray diffraction.* Biochemistry, 2001. **40**(46): p. 13802-13815.
127. Knapp, J.E., et al., *Allosteric action in real time: Time-resolved crystallographic studies of a cooperative dimeric hemoglobin.* Proceedings of the National Academy of Sciences of the United States of America, 2006. **103**(20): p. 7649-7654.
128. Perman, B., et al., *Energy transduction on the nanosecond time scale: Early structural events in a xanthopsin photocycle.* Science, 1998. **279**(5358): p. 1946-1950.
129. Ren, Z., et al., *A molecular movie at 1.8 angstrom resolution displays the photocycle of photoactive yellow protein, a eubacterial blue-light receptor, from nanoseconds to seconds.* Biochemistry, 2001. **40**(46): p. 13788-13801.
130. Stowell, M.H.B., et al., *Light-induced structural changes in photosynthetic reaction center: Implications for mechanism of electron-proton transfer.* Science, 1997. **276**(5313): p. 812-816.
131. Pokkuluri, P.R., et al., *Temperature and cryoprotectant influence secondary quinone binding position in bacterial reaction centers.* Febs Letters, 2004. **570**(1-3): p. 171-174.
132. Breton, J., et al., *Vibrational spectroscopy favors a unique Q(B) binding site at the proximal position in wild-type reaction centers and in the Pro-l209 -> Tyr mutant from Rhodobacter sphaeroides.* Biochemistry, 2002. **41**(43): p. 12921-12927.
133. Breton, J., et al., *Characterization of the bonding interactions of Q(B) upon photoreduction via A-branch or B-branch electron transfer in mutant reaction centers from Rhodobacter sphaeroides.* Biochimica Et Biophysica Acta-Bioenergetics, 2004. **1656**(2-3): p. 127-138.
134. Breton, J., *Absence of large-scale displacement of quinone Q(B) in bacterial photosynthetic reaction centers.* Biochemistry, 2004. **43**(12): p. 3318-3326.
135. Read, R., J. Sutherland, and P. Ghosh, *The Matrix Components of the Epiphyseal Growth Plate and Articular Cartilages from Dogs Treated with Ammonium Tetrathiomolybdate, a Copper Antagonist.* Australian Journal of Experimental Biology and Medical Science, 1986. **64**: p. 545-562.
136. Begley, P., et al., *Detection of Trace Levels of Trichothecenes in Human-Blood Using Capillary Gas-Chromatography Electron-Capture Negative-Ion Chemical Ionization Mass-Spectrometry.* Journal of Chromatography, 1986. **367**(1): p. 87-101.
137. Black, R.M., R.J. Clarke, and R.W. Read, *Detection of Trace Levels of Trichothecene Mycotoxins in Human-Urine by Gas-Chromatography Mass-Spectrometry.* Journal of Chromatography, 1986. **367**(1): p. 103-115.

138. Dohse, B., et al., *Electron-Transfer from the Tetraheme Cytochrome to the Special Pair in the Rhodopseudomonas-Viridis Reaction-Center - Effect of Mutations of Tyrosine L162.* Biochemistry, 1995. **34**(36): p. 11335-11343.
139. Ortega, J.M., et al., *Low-temperature electron transfer from cytochrome to the special pair in Rhodopseudomonas viridis: Role of the L162 residue.* Biophysical Journal, 1998. **74**(3): p. 1135-1148.
140. Ishikita, H., *Tyrosine Deprotonation and Associated Hydrogen Bond Rearrangements in a Photosynthetic Reaction Center.* Plos One, 2011. **6**(10).
141. Barry, B.A. and G.T. Babcock, *Tyrosine Radicals Are Involved in the Photosynthetic Oxygen-Evolving System.* Proceedings of the National Academy of Sciences of the United States of America, 1987. **84**(20): p. 7099-7103.
142. Debus, R.J., et al., *Directed Mutagenesis Indicates That the Donor to P-680+ in Photosystem-Ii Is Tyrosine-161 of the D1 Polypeptide.* Biochemistry, 1988. **27**(26): p. 9071-9074.
143. Ferreira, K.N., et al., *Architecture of the photosynthetic oxygen-evolving center.* Science, 2004. **303**(5665): p. 1831-1838.
144. Allen, J.F. and W. Martin, *Evolutionary biology - Out of thin air.* Nature, 2007. **445**(7128): p. 610-612.
145. Narvaez, A.J., et al., *Trapped tyrosyl radical populations in modified reaction centers from Rhodobacter sphaeroides.* Biochemistry, 2004. **43**(45): p. 14379-84.
146. Wampler, R.D., et al., *Selective Detection of Protein Crystals by Second Harmonic Microscopy.* Journal of the American Chemical Society, 2008. **130**(43): p. 14076-+.
147. Bozek, J.D., *AMO instrumentation for the LCLS X-ray FEL.* European Physical Journal-Special Topics, 2009. **169**: p. 129-132.
148. Struder, L., et al., *Large-format, high-speed, X-ray pnCCDs combined with electron and ion imaging spectrometers in a multipurpose chamber for experiments at 4th generation light sources.* Nuclear Instruments & Methods in Physics Research Section a-Accelerators Spectrometers Detectors and Associated Equipment, 2010. **614**(3): p. 483-496.
149. Mccoy, A.J., et al., *Phaser crystallographic software.* Journal of Applied Crystallography, 2007. **40**: p. 658-674.
150. Brunger, A.T., *Version 1.2 of the Crystallography and NMR system.* Nature Protocols, 2007. **2**(11): p. 2728-2733.
151. Boutet, S. and G.J. Williams, *The Coherent X-ray Imaging (CXI) instrument at the Linac Coherent Light Source (LCLS).* New Journal of Physics, 2010. **12**.
152. Kirian, R.A., et al., *Femtosecond protein nanocrystallography-data analysis methods.* Optics Express, 2010. **18**(6): p. 5713-5723.
153. Lovell, S.C., et al., *Structure validation by C alpha geometry: phi,psi and C beta deviation.* Proteins-Structure Function and Genetics, 2003. **50**(3): p. 437-450.
154. Laskowski, R.A., et al., *AQUA and PROCHECK-NMR: programs for checking the quality of protein structures solved by NMR.* J Biomol NMR, 1996. **8**(4): p. 477-86.
155. Schneider, T.R., *Objective comparison of protein structures: error-scaled difference distance matrices.* Acta Crystallographica Section D-Biological Crystallography, 2000. **56**: p. 714-721.
156. Henderson, R., *The Potential and Limitations of Neutrons, Electrons and X-Rays for Atomic-Resolution Microscopy of Unstained Biological Molecules.* Quarterly Reviews of Biophysics, 1995. **28**(2): p. 171-193.
157. Caleman, C., et al., *On the Feasibility of Nanocrystal Imaging Using Intense and Ultrashort X-ray Pulses.* Acs Nano, 2011. **5**(1): p. 139-146.